Relativistic One-Nucleon Removal Reactions

Thesis submitted in accordance with the requirements of
the University of Liverpool for the degree of Doctor in Philosophy
by

Stefanos Paschalis

Department of Physics

May 2008

Abstract

A well-established technique to probe the single-particle structure over a wide range of nuclei is the one-nucleon removal reactions in inverse kinematics using radioactive ion beams. This thesis presents inclusive measurements of one-nucleon removal from ^{57}Ni by a carbon (C) target. The interest in studying ^{57}Ni, a nuclide with only one nucleon (neutron) above the N = Z = 28 double shell closure, arises from the conflicting results regarding its single-particle nature that were extracted in several experiments. Moreover, this thesis discusses the first results of a new experimental technique used to identify the quasi-free (p,2p) and (p,pn) scattering processes in inverse kinematics, when the ^{57}Ni ions react with the protons of a polyolefin (CH_2) target, by the coincident detection of the two recoiling fast nucleons and the heavy outgoing fragment. In both reactions the measurement of the transverse momentum distribution of the projectile-like fragments, after the removal of one nucleon, provides information on the orbital angular momentum of the removed particle. The one-nucleon removal reactions with the C target induce mainly peripheral collisions, providing information only on the asymptotic part of the single-particle wave function, while the quasi-free scattering reactions can also probe more deeply bound nucleons providing an insight into the interior of the nucleus. The experiment was performed in May 2005 at GSI, Darmstadt, Germany using the LAND/ALADIN setup (future R^{3}B setup). The cocktail beam of the radioactive species under study was produced by the in-flight fragmentation of a $\sim$ 600 MeV/nucleon ^{58}Ni primary beam on a thick beryllium (Be) target and was selected and unambiguously identified on an event-by-event basis by the FRS separator. The ^{57}Ni fragments present in the cocktail beam reacted with the secondary target located at the LAND/ALADIN setup with an energy of $\sim$ 510 MeV/nucleon. A large part of this thesis is also devoted to presenting new calibration and reconstruction techniques integrated in the (under development) common analysis framework *land02*, which is used for on-line monitoring and off-line analysis of past and future experiments performed at the LAND/ALADIN setup.

To Marina,

for transforming grey into colours and colours into flowers ...

στο Βαγγέλλη,

που ήταν στεριά στις φουρτούνες μου κι εγώ αέρας στις δικές του.

Contents

List of Figures

List of Tables

Acknowledgements

In the next few paragraphs I would like to acknowledge the people that have supported me while writing this thesis and especially while carrying out the work that this thesis presents.

I would first like to thank my supervisor Marielle Chartier for providing the great opportunity to work in this field and get involved in her exciting research projects, for the funding, the guidance and the interesting discussions during our meetings, the useful suggestions on this thesis and for supporting my job applications. I would also like to thank Roy Lemmon for his guidance and his help to interpret the results and Robert Page for taking on advisory responsibilities for a few months the year before.

I would like to thank Tom Aumann for all his help, for making me feel as a member of the LAND group, for giving me the unique opportunity to participate and analyse experiments performed with the LAND/ALADIN setup, for always finding time to help me, for his enthusiasm and the stimulating discussions on physics and analysis, his guidance and his priceless comments on the results presented in this thesis. I feel also gratitude for his great support regarding my job applications throughout this stressful year.

The work presented in this thesis would not have been possible without the help, support and contributions from my colleagues at GSI. In particular, I would like to thank Håkan Johansson for initiating and leading the development of the analysis software, for his generous help with the analysis and the programming and for giving me the worst software "headaches". A great thanks to Kripa Mahata for helping me with the analysis and interpretation of the results, the close collaboration and his excellent work. Many thanks to Audrey Chatillon for her aid with the analysis. Thanks to Haik Simon for always being around ready to help and solve problems. A special thanks to Adam Klimkiewicz for his help during my first visit at GSI and all the good times and fun we had thereafter. Thanks to Dominic Rossi for his contributions in the analysis and to Yuliya Aksyutina for our discussions on the analysis. Thanks to Tudi Le Bleis for the fun in and out of the lab and the quiz-nights. A big thanks to the rest of the LAND group and the broader LAND collaboration for their friendliness, help and hospitality from my very first day at GSI and throughout these years. Konstanze Boretzky, Hans Emling, Michael Heil, Oleg Kiselev, Christine Wimmer, Wamers Felix,

Kristian Larsson, Thomas Nilsson, Ralf Plag, Rene Reifarth, Klaus Sümmerer... thanks a lot!

I would like to express my gratitude to Christos Touramanis for his generous help from the very beginning of my PhD, for keeping me sane throughout stressful periods and for supporting my job applications. The absorbing discussions on various exciting physics topics and his optimism have kept alive my enthusiasm for research.

Thanks to all the students, postdocs and staff of the nuclear physics group in Liverpool for their friendliness and help and for providing a pleasant working environment. I am particularly thankful to Beatriz Fernández-Domínguez for helping me with programming and GEANT4 simulations during my first year of my PhD, for her useful comments on the analysis, for proofreading this thesis and most of all for the great time and fun we had together. I would also like to thank the people providing the computing support, John Cresswell, Mark Norman and Janet Sampson. Thanks to Janet Sampson also for proofreading parts of this thesis.

Thanks a lot to the SPEG group at GANIL for their friendliness and help throughout the few months that I spent there participating in a campaign of experiments. A special thanks to Nigel Orr for his support regarding my job applications.

I would like to thank my mentor in nuclear physics Gerasimos Anagnostatos for his enthusiasm and the interesting and enlightening discussions on nuclear physics and for supporting and guiding me to start this PhD.

My closest friends, Aggelos, Vaggelis and Stathis for their support even while being so far away. My family in Greece, Evgenia and Dionisia, for all their love and support, for always believing in me.

The biggest thanks to my partner Marina, for her infinite love, enormous support and understanding.

Chapter 1

Introduction

The writing of the present thesis has coincided with two major events that significantly affect, if not define, the future of the UK and the European nuclear physics field: the form in the UK of the Science and Technology Facilities Council (STFC[1]) [1] and the "kick-off" of the Facility for Antiproton and Ion Research (FAIR) [2] in Germany, respectively. Both facts have introduced nuclear physicists to a much more competitive environment, which has forced them to bring to the surface the very fundamental questions that nuclear physics research is aiming to answer. Questions such as why and how neutrons and protons are grouped together to form nuclear matter and how nuclear research affects our knowledge and understanding of nature. Big pieces of the nuclear physics puzzle are revealed through studies of nuclear matter under extreme conditions, which is the main aim of the new nuclear facilities such as the NuSTAR (Nuclear STructure, Astrophysics and Reactions) project [3] at FAIR. In particular, the R^3B (Reactions with Relativistic Radioactive Beams) [4] international collaboration, which is part of the NuSTAR project, aims to investigate nuclear matter at the extremes of isospin for a wide range of nuclides by performing kinematically complete measurements of reactions with high-energy radioactive beams.

The material of this thesis concentrates on discussing some interesting physics results and presenting some new developments in the analysis of an experiment (S287) that was performed in May 2005 at GSI (Gesellschaft für SchwerIonenforschung) [5], Darmstadt, Germany using the LAND/ALADIN setup, which constitutes the precursor setup of the future R^3B project. The use of different targets, the large number of different nuclides present in the secondary beam and the kinematically complete measurement of all the incoming and outgoing species performed with the LAND/ALADIN setup enable the study of a wide range of nuclear physics aspects within the same experiment. This experiment probes collective modes of excitation as well as single-particle

[1] "STFC was formed through a merger of the Council for the Central Laboratory of the Research Councils (CCLRC) and the Particle Physics and Astronomy Research Council (PPARC) and the transfer of responsibility for nuclear physics from the Engineering and Physical Sciences Research Council (EPSRC)" [1].

properties in the neutron-rich Ni isotopic chain and neighbouring nuclei, as illustrated in Fig. 1.1, while at the same time tests and demonstrates new reaction techniques that will be employed in R^3B. The probing of such different degrees of freedom is achieved through electromagnetic and nuclear reactions occurring when the highly energetic (e.g. 510 MeV/nucleon for the ^{57}Ni secondary fragments) radioactive species of interest, which constitute the secondary beam under study, react with three different targets of C(187 mg/cm^2), CH_2(213 mg/cm^2) and Pb(519 mg/cm^2). The secondary beam used in this experiment is produced by the fragmentation of ^{58}Ni and ^{86}Kr primary beams on a thick Be target. In particular, the present experiment aims at

- extracting the dipole strength distribution in the continuum of the neutron-rich ^{68,70,72}Ni and of ^{56}Ni, covering thus a wide range of isospin from $N - Z = 0$ to $N - Z = 16$,
- measuring the partial cross sections and the transverse momentum distributions of the residual nucleus in one-nucleon removal reactions for the $N \sim 28$ and $N \sim 40$ region, giving an estimation of the spectroscopic factors and thus the single-particle occupancies of the removed nucleon, and
- testing the feasibility of the quasi-free scattering (p,2p) and (p,pn) reactions in inverse kinematics by measuring all three particles involved in the reaction, i.e. the residue and the two fast recoiling nucleons.

The dipole strength distribution has been systematically studied in a wide range of stable nuclei available as target material and has shown that nearly the complete dipole strength is absorbed into the giant dipole resonance (GDR), the most collective excitation in nuclei. The nature of the GDR is qualitatively understood as neutrons and protons oscillating against each other. With the advent of radioactive beams the question of how the multipole strength functions evolve for neutron-proton asymmetric nuclei can be investigated. This is of particular interest since the theoretical predictions for the dipole strength of neutron-rich nuclei suggest a redistribution of this strength towards lower excitation energies (stronger fragmentation of the strength) [6]. The nature of this low-lying dipole strength, which is commonly referred to as the "pygmy" dipole resonance, is still under investigation; however, the most preferable concept is that of a neutron skin oscillating against the core of the nucleus. The nuclei in the present experiment are probed through relativistic Coulomb excitation in inverse kinematics, as a result of high energy ions impinging on a thick Pb target. The measurement of the dipole strength in the Ni isotopic chain is a continuation of an experimental program to study the "pygmy" resonance in neutron-rich nuclei, i.e. the oxygen isotopic chain [7] and recently the heavier nuclei around ^{132}Sn [8].

Recent experimental studies on light neutron-rich atomic nuclei have indicated neutron sub-shell closures different than those known for stable nuclei [9, 10, 11] ("neutron

magic numbers" N = 8, N = 20, N = 28). For heavier neutron-rich nuclei, a shell gap at N = 40 is suggested rather than at N = 50 [12]. This experiment aims to shed light on the N = 40 region, where contradictory results have been found by recent experiments [13, 14], through a systematic study of the single-particle occupancies of the neutron-rich Ni isotopes (^{68,70,72}Ni, Z = 28, N = 40 − 44) via one-nucleon removal reactions. In order to perform such measurements a carbon (C) target is used and the orbital angular momentum l of the removed particle is determined from the precise measurement of the transverse momentum distribution of the residual nucleus with a coincident γ-ray measurement to identify the final state. Such measurements, known as one-nucleon removal reactions, were widely used in the last decade with either a carbon or a beryllium target in order to extract spectroscopic factors and thus single-particle occupancies for exotic nuclei in inverse kinematics.

Finally, this experiment also serves as a pilot experiment for quasi-free hadronic scattering (QFS) measurements in inverse kinematics. Hadronic quasi-free scattering (p,pN) reactions, i.e. (p,2p) and (p,pn), have been an excellent tool for probing single-particle properties in stable nuclei. Quasi-free scattering measurements in inverse kinematics require high beam energies of the order of few hundred MeV/nucleon, which are feasible in the present GSI facility. In contrast to one-nucleon removal reactions using a carbon or beryllium target, quasi-free scattering reactions are expected to probe the nucleon's wave function not only at the surface but also in the interior of the nucleus. To employ these reactions in inverse kinematics a target rich in hydrogen atoms (i.e. "free" from nuclear binding protons) is required. In the present experiment, in order to obtain single-particle information via the quasi-free (p,2p) and (p,pn) reactions, a CH_2 target is used where the "background" contribution from the carbon of the target can be estimated from the measurements with the pure carbon target.

This thesis is dedicated to the study of the single-particle properties of ^{57}Ni via one-nucleon removal reactions and quasi-free scattering (p,2p) and (p,pn) reactions, delivering the first results to be extracted from the present experiment. The interest in studying ^{57}Ni arises from the conflicting results regarding its single-particle nature that were extracted in several experiments. The single-particle character of the ground state and the low-lying excited states of ^{57}Ni has been questioned. A neutron-pickup experiment [15] suggested that excited states from ^{56}Ni may contribute to the lowest excited states of ^{57}Ni. Moreover, the large B(E2) value that is measured for ^{56}Ni [16], the core of ^{57}Ni, induces a high degree of collectivity and questions the single-particle character of ^{57}Ni. In contrast to these experimental findings, the pure single-particle character of the ground and the first two excited states in ^{57}Ni has been manifested in a transfer (d,p) reaction experiment [17]. The single-particle structure of ^{57}Ni via one-nucleon removal reactions has also been the study of a recent experiment [18] performed at MSU using, however, a lower beam energy than the one used in the

present experiment. In Ref. [18] reduced spectroscopic factors have been reported for the removal of a neutron leading to the ground or excited states of ^{56}Ni.

In this thesis the transverse momentum distribution of the outgoing projectile-like fragment, after the removal of one nucleon via the C(^{57}Ni,^{56}Ni)X and C(^{57}Ni,^{56}Co)X reactions, is deduced giving thus an insight into the single-particle nature of the removed nucleon. Moreover, the feasibility of the quasi-free scattering (p,2p) and (p,pn) reactions in inverse kinematics is discussed presenting results from p(^{57}Ni,^{56}Ni)pn and p(^{57}Ni,^{56}Co)2p reactions using a CH_2 target after subtracting the carbon contribution as background. The transverse momentum distribution of the outgoing projectile-like fragment was measured in coincidence with the two outgoing nucleons and some first kinematical observations are discussed. The theoretical framework, however, for such reactions in inverse kinematics is still under development.

With the forthcoming R^{3}B setup great effort and time has been invested within the LAND/ALADIN collaboration to develop a common analysis framework in C++ (*land02*), which will serve for off-line and on-line analysis of past, present and future experiments performed with this setup. The experimental results presented in this thesis are analysed within this framework, while a large part of the author's work has been invested on the development of calibration and reconstruction routines for this framework. Thus, this thesis is also dedicated to presenting some of the new analysis procedures in more detail.

In order to accommodate the aforementioned investigations, this thesis comprises of 6 chapters. In Chapter 2 the structure of exotic nuclei is briefly described together with the motivations and the highlights of the recent investigations in this field. In addition, an introduction on the theoretical techniques behind the nuclear reactions discussed in this thesis is presented. Chapter 3 provides a brief description of the main experimental parts used in the present experiment. In Chapter 4 the main calibration and reconstruction procedures are described together with examples from the present experiment. The analysis and the results obtained for ^{57}Ni for both (C and CH_2) targets are presented in Chapter 5 including the first kinematical observations of the quasi-free scattering (p,2p) and (p,pn) reactions in inverse kinematics. This chapter concludes with the discussion that arises from these results. In Chapter 6 the work presented in this thesis is summarised and its implication for future work is stated.

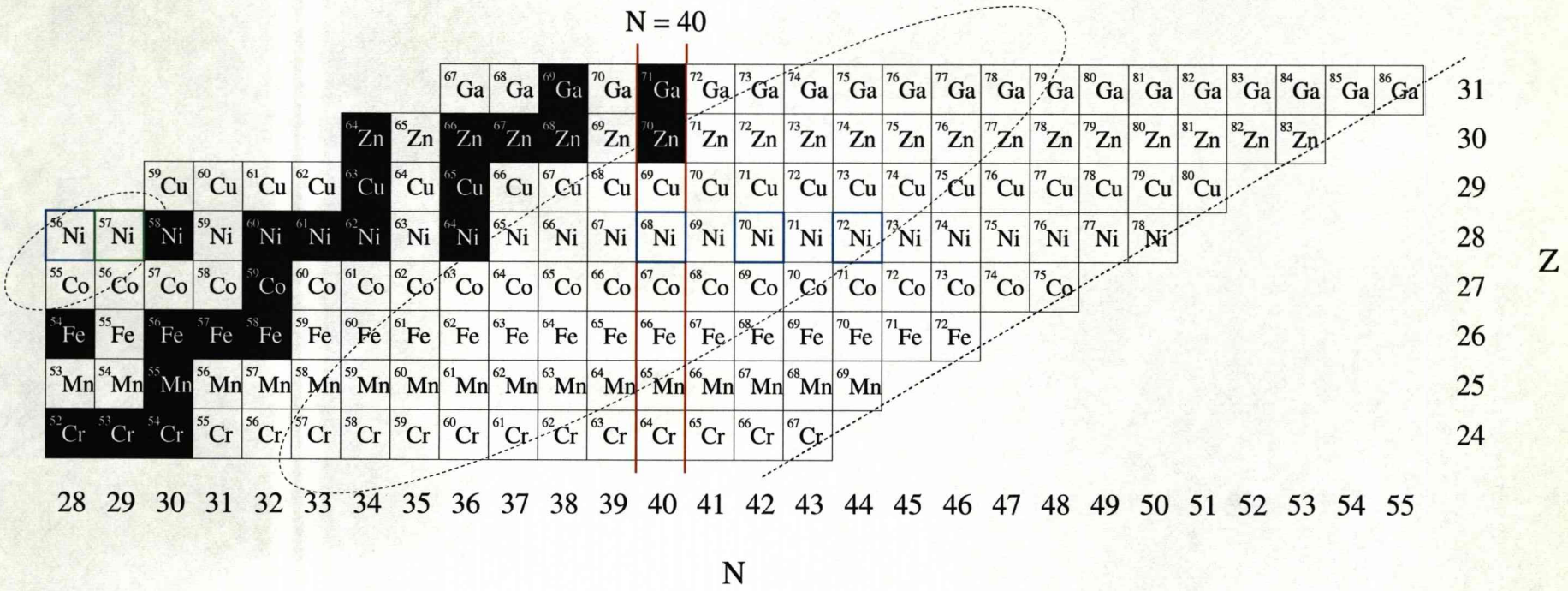

Figure 1.1: The region of interest lies around the Z = 28 shell closure and towards the neutron-rich side of the nuclear chart. The stable isotopes are shown in black-filled squares, while the N = 40 region is highlighted in red. The even-even Ni isotopes of which the electromagnetic excitation is of primary interest in this experiment are highlighted with a blue box. The Ni isotope under study in this thesis (^{57}Ni) via one-nucleon removal and quasi-free scattering reactions is highlighted with a green box. The dashed line represents the experimentally suggested neutron drip line; the data are taken from Ref. [19]. The dashed ellipses show roughly the nuclides available in the secondary beam delivered in the present experiment.

Chapter 2

Exotic nuclei

2.1 Introduction

Early experiments have clearly indicated that an atom has a small, central, dense, positively charged core, the atomic nucleus. The nucleus is a collection of nucleons (protons and neutrons), which interact with each other mainly through the strong interaction. With classical considerations particles interacting with strong attractive forces should be packed in the closest possible geometrical configuration to maximise the binding energy of the system. Motions in this system should be rather complicated and the collisions very frequent. The nucleus, however, is a quantum-mechanical system where Pauli's and uncertainty principles do not allow this very dense configuration and they give rise to structure effects. Coulomb and weak interactions also affect the structure of the nucleus.

In contrast to atomic physics, in nuclear physics there is not a unified theory that can describe nuclear structure and explain nuclear properties. Several models have been proposed throughout the years which are usually successful only in a small part of the nuclear chart. This fact reveals the difficulty of the nuclear physics problem, which is mainly due to the unclear nature of the strong interaction and the number of particles involved.

One of the first attempts of nuclear theory was to describe the nucleus as a liquid drop [20], which explains qualitatively the almost constant density of the nucleus, its binding energy and its well-defined surface. There had been, however, observations that nuclei with certain numbers of protons or neutrons were more "favoured", in the sense that they were much more stable than the rest, which was not consistent with the liquid drop approach. The specific numbers of protons or neutrons for which nuclei are more bound are known as magic numbers (Z or N = 2, 8, 20, 28, 50, 82 and N = 126). These observations were very similar to atomic physics observations of particularly stable electron configurations (noble gases) and were a clear indication of a shell structure in the nucleus.

In order to use the well-established formalism of atomic physics and the analogy of

the atom with the nucleus, there was a need for a central potential (like the nucleus in the atom) under which all nucleons would move independently. Such a potential in the case of the nucleus can be thought of as being built up by the individual two-body nucleon interactions and is known as mean-field potential. A reasonable choice for the shape of this potential could be, for example, the mathematically convenient harmonic oscillator (for which the eigenfunctions can be given in closed form) or the more realistic Woods-Saxon potential. However, when filling any of these potentials with nucleons following Pauli's principle, most of the magic numbers derived were different from those observed experimentally.

In atomic physics the fine splitting observed in the spectral lines of the hydrogen atom is caused by the spin-orbit interaction. Inspired once more from atomic physics, a spin-orbit term was introduced for the nucleons, only that in the nuclear case it had to be strong enough to recover the observed magic numbers [21, 22]. The successful reproduction of the observed magic numbers through these simple considerations was a great success for mean-field theories such as the independent-particle shell model (see Fig. 2.1). Explanation of the angular momentum of the ground state and some low excited states of many nuclei were also supporting the validity of mean-field and independent-particle motion assumptions.

Although this simplified approach was very successful, especially for a range of nuclei not far away from simply/doubly magic nuclei, it is clear that residual interactions, such as nucleon-nucleon correlations, exist and play an important role in nuclear structure and nuclear properties. The shell model has evolved to account for some of these residual interactions, extending its predictive power in a wider range of nuclei and enabling a much more detailed understanding of nuclear structure. The inputs in a modern shell-model calculation, such as the mean-field potential and corrections for the residual interactions, are deduced from studies with stable nuclei, resulting in a sufficiently good reproduction of experimental observables for nuclei around the valley of β stability. It appears, however, that nuclear structure changes dramatically under extreme conditions, such as high temperature, high mass, high spin and high isospin [24]. Theoretical models usually not only fail to reproduce experimental observations under such conditions, but also their predictions diverge significantly from each other. This fact is evidence that yet a lot needs to be understood about nuclear structure and the nucleon-nucleon interaction and that extreme conditions provide a definitive test of nuclear theory.

Reaching these extreme conditions constitutes an experimental challenge. In particular, investigations of nuclei at the extremes of isospin, also known as exotic or rare isotopes, have been enabled by the recent development of radioactive ion beams. These beams are currently constituting one of the frontiers of experimental nuclear physics and their future is even brighter through the construction of new radioactive beam fa-

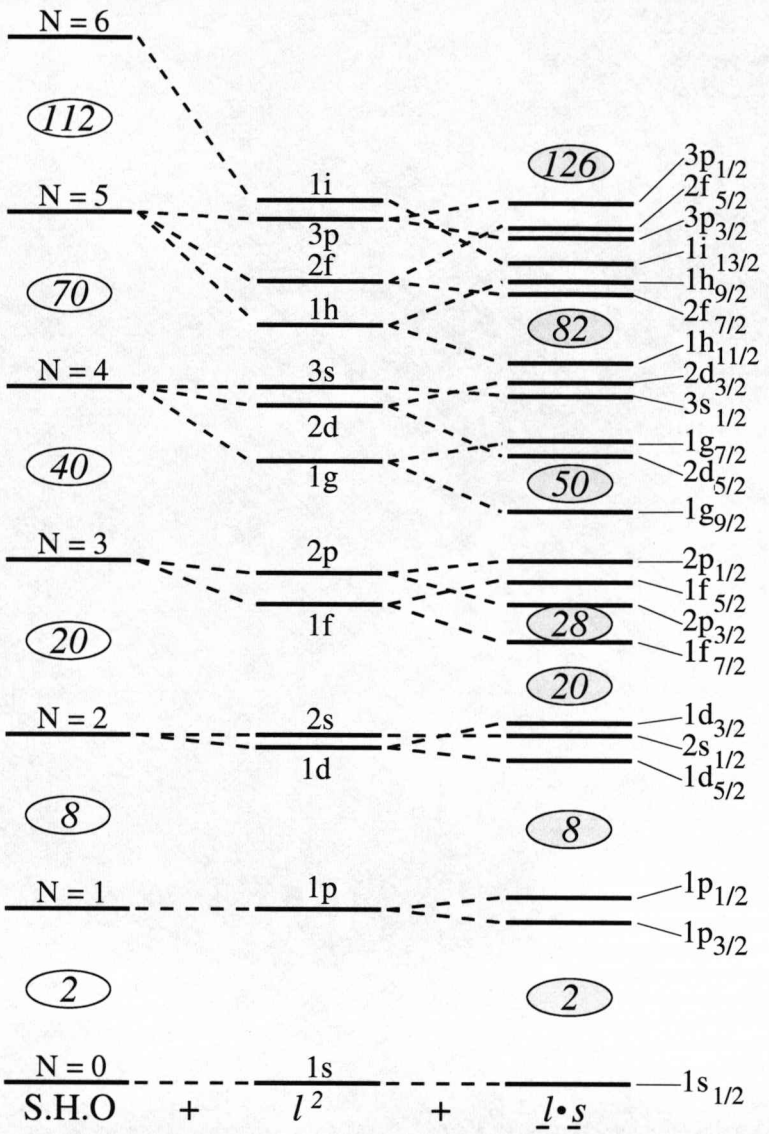

Figure 2.1: Schematic energy levels for a spherical harmonic oscillator (left) and after introducing a strong spin-orbit interaction (right). Large shell gaps give rise to the so-called magic numbers which are shown inside ellipses. In the right level scheme the shell gaps and thus the corresponding magic numbers are the same as those observed experimentally for nuclei close to the valley of β stability, which supports the assumption for a strong spin-orbit interaction. The picture is modified from Ref. [23].

cilities around the globe. They are particularly useful for reaching neutron-rich nuclei, where new phenomena and interesting features of nuclear structure have been revealed. A lot of theoretical and experimental attention has been drawn lately in studying how the average mean field and the nuclear wave function are affected in neutron-proton asymmetric nuclei and understanding new phenomena appearing in neutron-rich matter such as neutron halos and neutron skins. These issues are further discussed in the following sections.

2.2 Nuclear structure of exotic nuclei

2.2.1 Neutron halos and neutron skins

In principle, adding more neutrons in a nucleus results in systems with their outer neutrons loosely bound. This fact has some very interesting consequences, as the wave function of the weakly bound neutrons extends far beyond the core of the nucleus in the classically-forbidden region, due to tunnelling effects. The neutrons' extended density distribution can be considered to form a halo structure when surrounding a well-defined inert core. Halos in light neutron-rich nuclei have first been observed experimentally more than two decades ago [25] and since then a great deal of experimental effort has been devoted to study them. The two-neutron halo ^{11}Li in particular appears to be experimentalists' and theorists' favoured halo nucleus. The theoretical approach to halo nuclei is that of two- or three-body systems referring to the core and the one or two halo particles, respectively. Such systems provide a unique tool for studying the nucleon's wave function within a low density environment, where it is expected to behave in a significantly different way than inside the quite dense nuclear core.

In heavier nuclei, it is expected that adding more and more neutrons can lead to the development of a neutron skin at the surface of the nucleus, due to the very different neutron-proton Fermi levels. Such skins are a completely new form of nuclear matter consisting only of neutrons. This matter is found only in neutron stars and could not be probed in the laboratory until recently. Great experimental and theoretical interest has been drawn in determining the thickness of this skin for different isotopes. Probing the thickness of the neutron skin provides information on the symmetry-energy term in the nuclear equation of state [26]. There has been experimental evidence that this skin can oscillate against the inert core, giving rise to a new type of low-lying resonance collective excitation. Measuring this low-lying resonance excitation is a promising way for extracting information on the thickness of the neutron skin [8, 27].

2.2.2 Evolution of shell gaps

Nuclei with a large neutron excess are of great interest not only for studying these new phenomena and new forms of nuclear matter described above, but also for challenging the established shell structure in nuclei. As mentioned before, the introduction of a strong spin-orbit interaction to the mean-field theory and the consequent shell structure, shown in Fig. 2.1, provides an explanation for the magic numbers in stable nuclei, as a result of the large shell gaps in the energy level spectrum. However, there is more and more evidence showing that the shell structure is very fragile when moving away from stability. For nuclei with large neutron-proton asymmetry the nuclear potential and residual interactions are altered leading to significant shifts and even re-ordering of the energy levels. In particular, the empirical strong spin-orbit interaction appears

to weaken with neutron excess. In other words, shell gaps created by this interaction collapse and thus established magic numbers are no longer true (see Fig. 2.2).

Modern modifications of the mean field and the residual interactions suggest that new magic numbers emerge for neutron-rich nuclei and there has even been some experimental evidence in light nuclei supporting this prediction. A well-known example is the so-called island of inversion observed for the N = 20 isotones with Z $\leq$ 12; such a phenomenon was first observed in ^{31}Na mass measurement studies [28], where the disappearance of the N = 20 magic number was suggested. Many studies using completely different experimental techniques have been performed in this region reporting a dramatic change in nuclear structure (see Ref. [10] and references therein). In particular, strong deformations have been found in this region, which cause the intruder configuration with opposite parity from higher state becoming the ground state.

Moving even further towards the neutron drip line, it is possible that energy levels become almost equally spaced for single-particle excitations and magic numbers disappear completely (see left level scheme of Fig. 2.2). This leads to large diffuseness of the nuclear surface and to the new phenomenon of neutron skins discussed in the previous section.

2.2.3 Single-particle structure

In a simplified mean-field approach nucleons are filling up the average potential such that each of them occupies a single-particle quantum state in this potential and the particles are not interacting with each other. Non-interacting nucleons in a nucleus can be considered as a Fermi gas (collection of non-interacting fermions). In a Fermi gas the highest state occupied (at zero temperature) is called the Fermi energy or Fermi surface. Every state below the Fermi energy is fully occupied by a nucleon and the states above are completely empty. In such a simplified model the occupation of each quantum state is 100%. This approach reflects the single-particle (or microscopic) structure of the nucleus. Nuclear properties and nuclear structure, however, are affected by both single-particle and collective degrees of freedom. In a modern shell model approach although the deeply-bound states are still considered to be fully occupied, the states close to the Fermi surface (valence orbitals) can have occupancies which are just a percentage of the full strength. To account for such reduced occupancies it is needed to include in the calculations effects beyond the mean field such as configuration mixing and correlations.

The occupancies of the nuclear states offer a way of identifying the single-particle component in the nuclear wave function, but the occupancies themselves are not a direct observable. What can be probed experimentally are the absolute spectroscopic factors (see Sections 2.3.1 and 2.3.2), which reflect these occupancies. The spectroscopic factors are usually probed experimentally with direct reactions such as transfer reactions, the

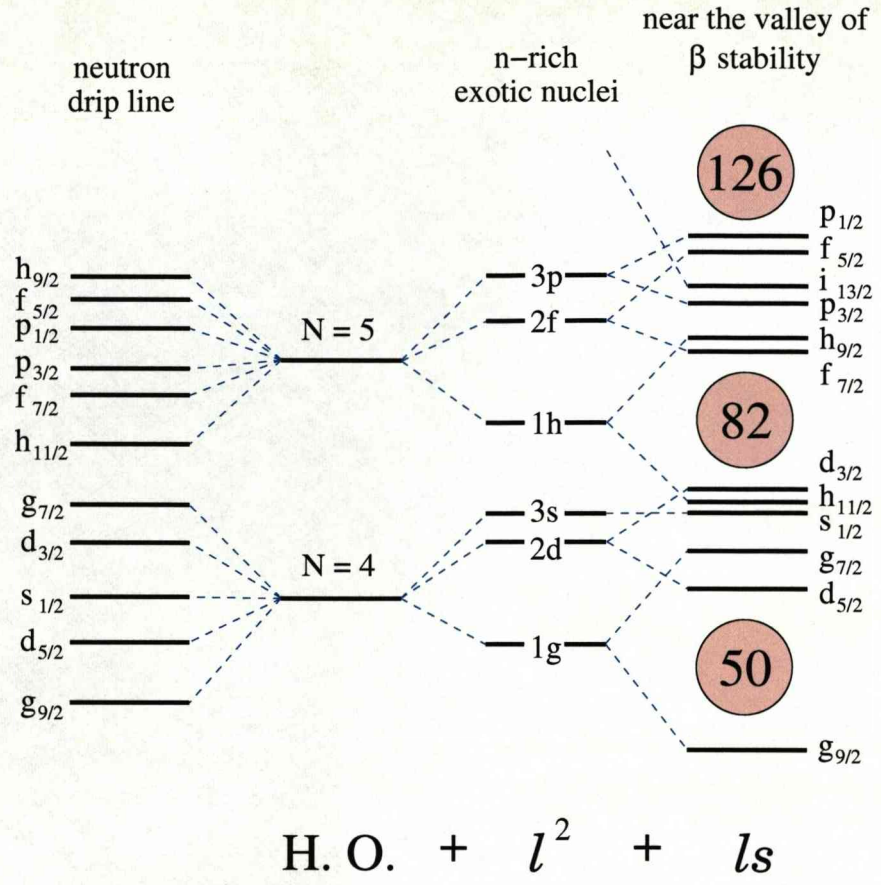

Figure 2.2: The level scheme of spherical harmonic oscillator with strong spin-orbit interaction (right level scheme) reproduces exactly the magic numbers observed for nuclei around the valley of β stability. For neutron-rich nuclei, where it is predicted that spin-orbit interaction is much weaker, energy levels shift and form new shell gaps and thus new magic numbers (centre-right level scheme). In the neutron drip line energy levels could become almost equally spaced (left level scheme) causing magic numbers to disappear. The picture is modified from Ref. [29].

more accurate (e,e'p) knockout reactions and lately the nucleon-removal reactions in inverse kinematics, discussed in the following section.

It is convenient to present results from such studies as the ratio between the experimentally measured spectroscopic factors and those deduced from shell-model calculations. This ratio is known as the quenching (or reduction) factor R_s [30, 31]. This factor reflects the reduced occupancy compared to a single-particle picture. Experiments strongly support significantly reduced occupancies (60%-70%), compared to the single-particle values, for the valence states in stable nuclei [18, 32, 33]. In Fig. 2.3 quenching factors obtained with different experimental techniques are shown as a function of the difference of neutron and proton separation energies. It is clear that there is a strong correlation between R_s and the difference in separation energies which is linked to the nuclear symmetry energy [34]. Understanding these trends of spec-

troscopic factors tests the validity of nuclear shell model and constitutes one of the major motivations for probing neutron-proton asymmetric nuclei, where the difference of neutron-proton separation energies varies significantly.

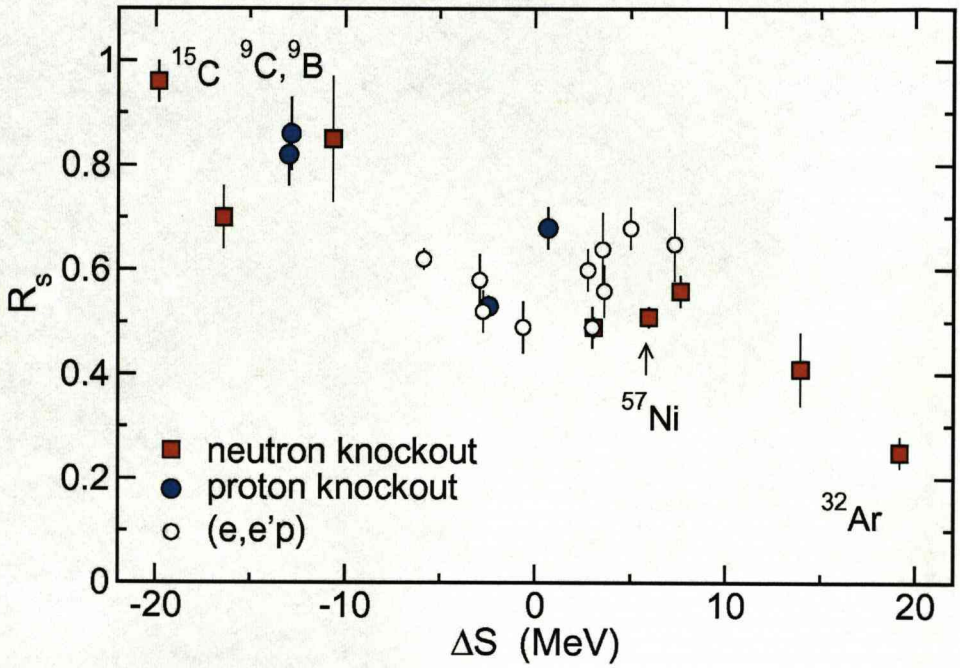

Figure 2.3: Quenching factors as a function of the difference of neutron (S_n) and proton (S_p) separation energies obtained with (e,e'p) reactions (open circles), one-proton removal reactions (blue circles) and one-neutron removal reactions (red squares). $\Delta S = S_n - S_p$ for neutron spectroscopic factors and $\Delta S = S_p - S_n$ for proton spectroscopic factors. A strong dependence of the quenching factor upon ΔS is evident [35].

2.3 Direct nuclear reactions as spectroscopic tools

In direct nuclear reactions the mechanism can be simplified enough to allow the study of nuclear structure and nuclear properties. Thus, they have been a widely used spectroscopic tool to probe the single-particle structure and the properties of nuclei for many decades. With the recent development of fast radioactive beams this tool is now used for the study of exotic nuclei far from stability. In reactions with radioactive beams the nucleus to be studied is no longer the target nucleus but the projectile and thus inverse kinematics should be used. In this text only direct reactions are further discussed and specifically reactions in inverse kinematics which are used in conjunction with relativistic radioactive beams.

Among the many types of direct reactions, those which are used with radioactive beams in inverse kinematics are the transfer reactions [36, 37] (stripping, pickup) and

one-nucleon removal reactions [10, 38, 39]. Lately, a lot of interest is drawn on studying exotic nuclei via the (p,2p) and (p,pn) quasi-free scattering reactions, which together with the (e,e′p) quasi-free scattering reactions have been a very successful spectroscopic tool for stable nuclei.

Using the aforementioned direct reactions, it is possible to obtain valuable information on nuclear structure through comparison of the measured partial cross sections and momentum distributions with calculated ones. This comparison allows the extraction of the spectroscopic factors of the shell-model states involved in the reaction, as well as the angular momentums of these states.

In order to obtain the spectroscopic factors experimentally, it is always necessary to use estimated single-particle cross sections from theoretical calculations. Thus, they are always model dependent. This fact has led to some contradictory results and has invoked a lot of discussion on whether they can provide a safe observable. It is believed that (e,e′p) reactions provide much more reliable information on spectroscopic factors. This is due to the better understanding of the interaction involved (electromagnetic) and the low probability of the electrons to interact with the nuclear matter while leaving the nucleus area after the knockout reaction (i.e. low re-scattering), minimising the distortion of their momentum change measurement. However, it appears that the (e,e′p) quasi-free scattering reactions are more difficult to adjust in radioactive beam experiments compared to the hadronic ones from a technical point of view. Furthermore, the hadronic quasi-free scattering can also probe the neutrons' wave function.

In the following sections the one-nucleon removal reactions and the hadronic quasi-free scattering reactions (mentioned also as knockout reactions) are presented in more detail together with some example cases. Moreover, the complementarity and differences of these two types of reactions are further discussed in Section 2.3.3.

2.3.1 One-nucleon removal reaction

In this reaction one nucleon is knocked out or removed from a (mass-A) projectile during peripheral collisions with a light target, as illustrated in Fig. 2.4. The (A−1) residue is then detected in coincidence with its in-flight decay γ rays, so an identification of its final state can be performed. Although most often all fragments of the reaction cannot be detected, within the appropriate theoretical framework (Glauber method, see later) an indirect measurement of the momentum $\vec{k}$ of the knocked-out nucleon in the projectile is possible by measuring the momentum $\vec{k}_{\mathrm{A}}$ of the projectile and $\vec{k}_{\mathrm{A}-1}$ of the residue according to the following expression

$$\vec{k} = \frac{\mathrm{A}-1}{\mathrm{A}}\vec{k}_{\mathrm{A}} - \vec{k}_{\mathrm{A}-1}, \tag{2.1}$$

providing a measurement of the wave function of the knocked-out nucleon [31, 40, 41]. Indeed, the momentum distribution of the residue reflects the orbital angular

momentum l of the state from which the nucleon is knocked out. The shape and width of the momentum distributions can give information about nuclear structure. For example narrow widths indicate waves often associated with a halo structure, satisfying Heisenberg's uncertainty principle where large spatial distribution (halo) corresponds to well-defined (narrow) momentum distributions.

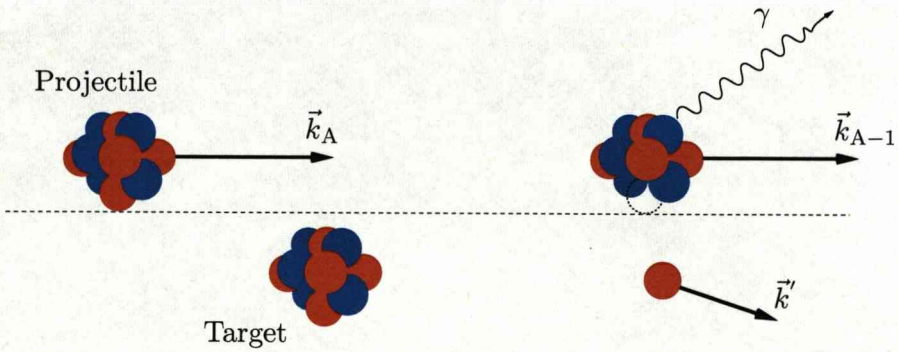

Figure 2.4: One-nucleon removal reaction in inverse kinematics, diffraction dissociation case.

The theoretical framework supporting one-nucleon removal reactions in inverse kinematics is based on the Glauber method [40, 42] which consists of the following two main approximations:

- the adiabatic (or sudden) approximation and
- the eikonal approximation.

The first one, which is common for all semi-classical approaches, requires that the time of the reaction to occur is short enough to allow the hypothesis that the nucleons inside the nucleus are frozen. In the second it is assumed, in the simplest form of the approximation, that the projectile travels along a definite straight-line trajectory through the field of the target nucleus, so that one can integrate along a straight-line path which simplifies the calculations considerably.

In other words, let κ be the incident wave number of a point particle scattered by potential with depth V_0 and range α. Then the above two approximations can be expressed as a requirement that the wavelength ($\lambda = 1/\kappa = \hbar/p$) of the incident particle is much shorter than the interaction region

$$\kappa\alpha \gg 1, \tag{2.2}$$

and that the energy E' of the scattered particle is much larger than the depth of the potential

$$E' \gg V_0. \tag{2.3}$$

This is equivalent with the requirement that the initial momentum is much higher than the momentum change in the reaction caused by the target potential, so that the projectile continues in the same trajectory before and after the reaction with the target, as shown in Fig. 2.5 [43, 44, 45].

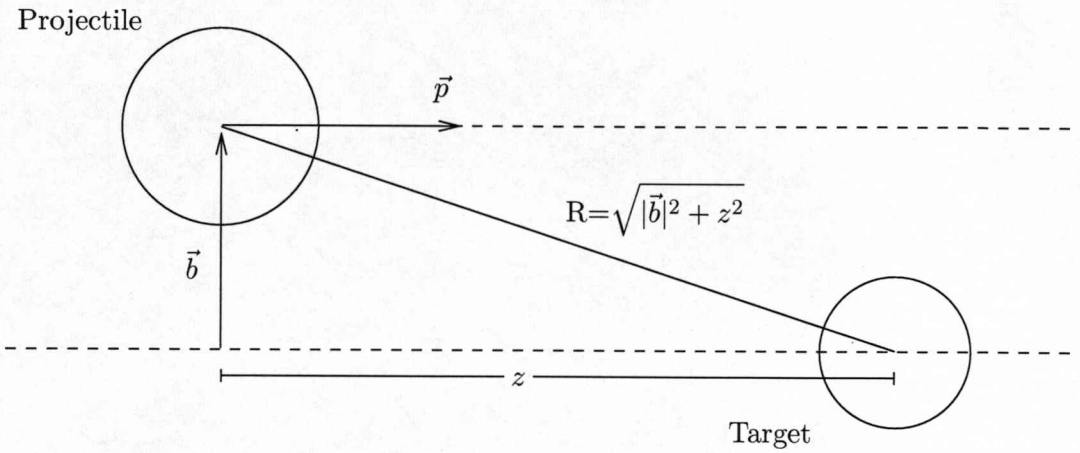

Figure 2.5: In the eikonal approximation, the projectile travels along a straight-line trajectory before and after the reaction. The trajectory is defined by the impact parameter ($\vec{b}$), which is a two-dimensional vector representing the minimum distance between the projectile and the target nucleus.

By performing the one-nucleon removal reactions using relatively high beam energies and light targets, the aforementioned approximations are valid. Within this theoretical framework the spectroscopic factors and thus the single-particle occupancies can be extracted through comparison of the measured partial cross sections with those deduced theoretically. Qualitatively speaking the spectroscopic factor describes in general the single-particle nature of a (quantum) state, i.e. the "real" occupancy of nucleons in the states obtained from the shell model. As discussed earlier, it is used to connect measurements with theories of nuclear structure, through comparison of the theoretical and experimental cross sections. In Refs. [31, 38, 46] this connection is successfully done with the assumption that the partial cross section $\sigma_{th}(I^\pi)$ for populating a given final state I^π of the residue (core) in a single-nucleon removal reaction is expressed as

$$\sigma_{th}(I^\pi) = \sum_j C^2S(I^\pi, nlj)\sigma_{sp}(S_n, nlj). \tag{2.4}$$

In Eq. 2.4 C^2S is the spectroscopic factor for the removal of a nucleon with given single-particle quantum numbers (nlj) and it expresses the parentage of this configuration in the initial state with respect to specific final state I^π of the remaining nucleons. The sum runs over all possible configurations (with a non-negligible parentage in the projectile ground state). The single-particle cross section σ_{sp} of Eq. 2.4 is the sum of

two main contributions [47],

$$\sigma_{sp} = \sigma_{str} + \sigma_{diff}, \tag{2.5}$$

the stripping (or inelastic) breakup (σ_{str}), in which the removed nucleon reacts with the target, and the diffraction dissociation (diffractive or elastic breakup) (σ_{diff}), in which the removed nucleon is at most elastically interacting with the target.

The Coulomb dissociation can also have an important role in the single-particle cross section, but it depends on the charge Z of the target and thus for light targets it can be neglected. The cross sections for the stripping and elastic breakup processes are written [47] as

$$\sigma_{sp}^{str} = \frac{1}{2J+1} \int d\vec{b} \sum_{M} \langle \phi_{JM} | (1 - |\mathcal{S}_n|^2) | \mathcal{S}_c |^2 | \phi_{JM} \rangle, \tag{2.6}$$

$$\sigma_{sp}^{diff} = \frac{1}{2J+1} \int d\vec{b} \left[\sum_{M} \langle \phi_{JM} | | (1 - \mathcal{S}_c \mathcal{S}_n) |^2 | \phi_{JM} \rangle - \sum_{M,M'} | \langle \phi_{J'M'} | (1 - \mathcal{S}_c \mathcal{S}_n) | \phi_{JM} \rangle |^2 \right], \tag{2.7}$$

where $|\phi_{JM}\rangle$ are the wave functions describing the relative motion of the removed nucleon (n) and the residue (c), J is the total angular momentum ($J = j+I$) of the nucleon (j) and the nucleus (I). $\mathcal{S}_c$ and $\mathcal{S}_n$ are the scattering matrices ($\mathcal{S}$-matrices), which relate the initial and the final states of the residue core-target and removed nucleon-target systems, respectively. It should be pointed out that there is a strong dependence of the single-particle cross section upon the separation energy S_n and angular momentum l of the removed nucleon [47].

Example cases

Two characteristic example cases of one-nucleon removal reactions with radioactive beams are discussed in this section. In the first one the momentum distributions of the residues and the cross-section measurements for this reaction are inclusive. In other words, the contribution from the different final states of the residue is not resolved, since no coincident γ-ray measurement is performed. In the second example, however, the final states of the residue are identified (exclusive measurement).

In Fig. 2.6 inclusive measurements of the transverse momentum distribution for the (A−1) residue after one-neutron removal reaction from the neutron-rich F, O, N, C and B isotopes by a C target [48] are illustrated. In this figure it is evident that the width of the momentum distributions varies significantly, even for neighbouring isotopes. For example it is noted the considerable reduction in the width of the distributions for ^{14}B and ^{15}C with respect to their lighter isotopes ^{13}B and ^{14}C. This reduction is associated with the crossing of the N = 8 shell closure. Furthermore, the narrow momentum distributions, the large one-nucleon removal cross sections and the weakly bound valence neutron in ^{14}B and ^{15}C are evidence of a halo structure.

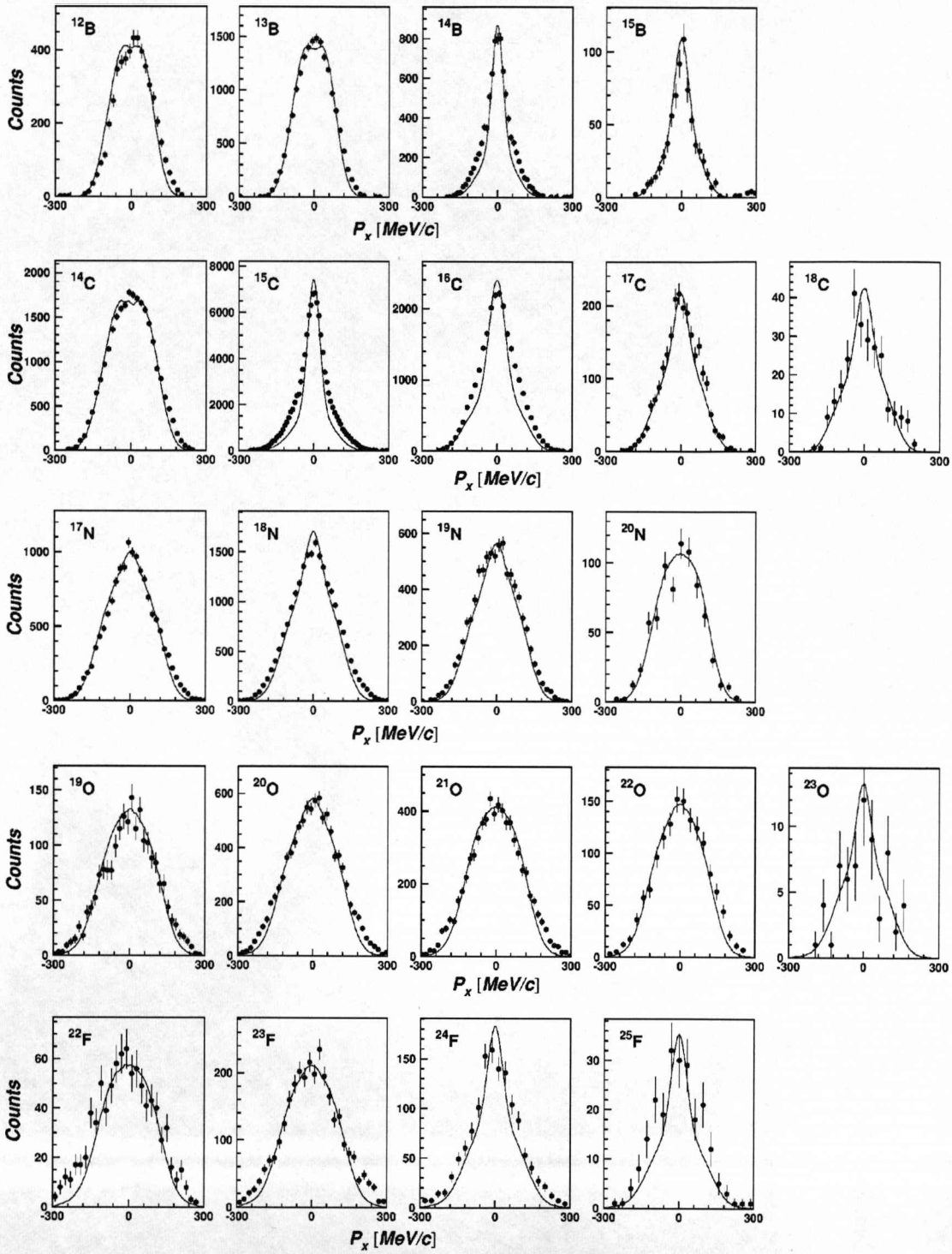

Figure 2.6: Transverse momentum distributions inclusive measurements for the (A−1) residue after one-neutron removal reaction from a cocktail of radioactive ion species produced by the fragmentation of ^{40}Ar at GANIL, Caen, France. Narrow distributions, as in ^{14}B and ^{15}C, and large one-nucleon removal cross sections are often associated with a halo structure. The picture is taken from Ref. [48].

Exclusive measurements of the partial cross section from each individual final state, which allows the extraction of spectroscopic factors, require γ-ray coincident measurements and comparison with theoretical estimations. Extensive exclusive studies of one-nucleon removal reactions by measuring the momentum distribution of the (A−1) residue fragments with a coincident measurement of the prompt γ rays have been performed in the last decade at NSCL/MSU, e.g. Refs. [9, 10, 38, 39]. An example case of such studies is shown in Fig. 2.7. A neutron is removed from ^{12}Be by a ^{9}Be target and the momentum distribution of the ^{11}Be residue is measured for its different final states, i.e. the ground state and the only bound excited state of ^{11}Be. Comparison of the measurements with the theoretical calculations suggest that the removed neutron from ^{12}Be, when the ^{11}Be is at the ground state (i.e. removal of a valence neutron), has an orbital angular momentum of $l = 0$ in the nucleus. This result shows that N = 8 is not a good closed shell for the neutron-rich ^{12}Be [9].

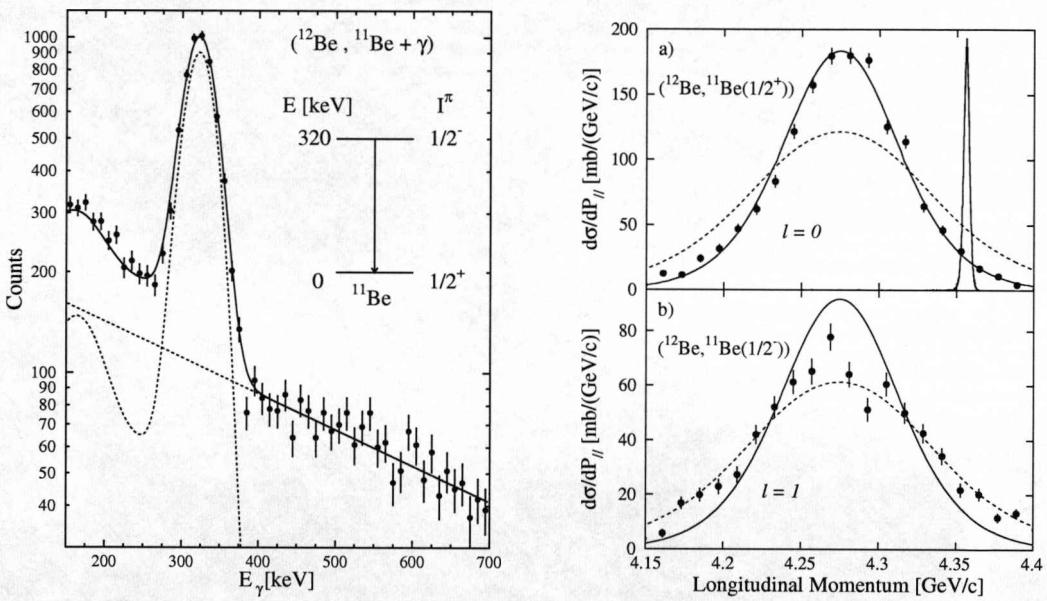

Figure 2.7: Longitudinal momentum distributions (right) for the ^{11}Be residue after one-neutron removal reaction from ^{12}Be, by selecting the ground state (a) or the excited states (b) of ^{11}Be through γ-ray tagging (left). Calculations for $l = 0$ (solid line) and $l = 1$ (dashed line) are also shown for comparison. The picture is taken from Ref. [9].

A wide range of light exotic nuclei has been explored via the one-nucleon removal reactions in the last decade. The exciting results from these studies are challenging nuclear structure theories and have established the one-nucleon removal reactions as a powerful spectroscopic tool for studies with radioactive beams. Moreover, the one-nucleon removal reaction measurements are feasible even with beam rates as low as few ions/s, allowing very exotic species to be probed with this technique.

2.3.2 Quasi-free scattering reaction

Quasi-free scattering, as described in Ref. [49], is a process in which a high energy (100 − 1000 MeV) particle knocks a nucleon out of a nucleus and no further violent interaction occurs between the nucleus and the incident or the two outgoing particles, a sort of free elastic scattering. In fact, although violent interaction occurs only between the knocked-out nucleon and the incident particle, the wave functions of both the incoming and outgoing nucleons are distorted while passing through the nucleus. Quasi-free scattering (x,xN) reactions, and particularly the (p,2p) and (e,e′p), have been used extensively in normal kinematics and provide one of the best ways to explore single-particle properties of stable nuclei [49, 50, 51].

The basic concepts of the (p,2p) process in normal kinematics, as discussed in Ref. [49], are presented below (see also Fig. 2.8). The symbols E, T and $\vec{k}$ stand for the total energy, the kinetic energy and the momentum of the incoming proton (0), the two outgoing protons (1, 2) and the residual nucleus (A−1). The separation energy (S) of the knocked-out proton for a certain final state of the nucleus is

$$S = T_0 - (T_1 + T_2 + T_{\mathrm{A}-1}). \tag{2.8}$$

Conservation of energy and momentum give

$$E_0 + M_{\mathrm{A}}c^2 = E_1 + E_2 + E_{\mathrm{A}-1}, \tag{2.9}$$

$$\vec{k}_{\mathrm{A}-1} = \vec{k}_0 - \vec{k}_1 - \vec{k}_2 = -\vec{k}_3, \tag{2.10}$$

where $\vec{k}_3$ is the momentum the knocked-out nucleon had in the nucleus.

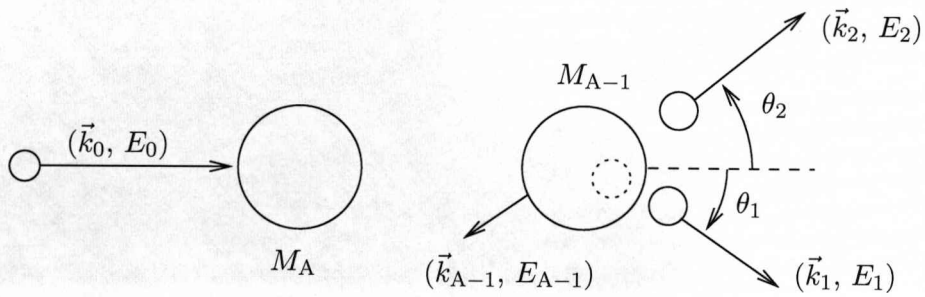

Figure 2.8: Quasi-free scattering in normal kinematics. For non-relativistic free nucleon-nucleon scattering $\theta_1 + \theta_2 = 90\,^\circ$.

The theoretical framework to study the quasi-free scattering reactions is based on the impulse approximation. Assuming an incident proton reacting with a nucleus, the main assumptions underlying this approximation can be expressed [52] as follows:

- the incident proton interacts strongly with at most one nucleon at the same time,

- each strong interaction of the incident proton with a nucleon is not affected by the presence of the other nucleons and
- during the fast, strong interaction of the incident proton with a nucleon, the binding forces in the nucleus are negligible.

The differential cross section of such reaction is usually estimated within the Distorted Wave Impulse Approximation (DWIA) and can be written [53] as

$$\frac{d^3\sigma}{d\Omega_1 d\Omega_2 dE_1} = S_b F_k \frac{d\sigma}{d\Omega_{p-p}} G(\vec{k}_3), \tag{2.11}$$

where S_b is the spectroscopic factor of the knocked-out proton, F_k is a kinematic factor and $d\sigma/d\Omega_{p-p}$ is the cross section for a free proton-proton scattering. Finally, G is the distorted momentum distribution of the removed proton. This distorted distribution accounts for the angular momentum of the proton in the nucleus and the unavoidable re-scattering that the outgoing proton feels while escaping the nucleus. This term is estimated using complex (real + imaginary parts) optical potentials, which makes the calculation of the differential cross section model dependent.

Example cases

An example case of quasi-free (p,2p) scattering in normal kinematics is the ^{16}O(p,2p)^{15}N reaction [49] (see Fig. 2.9). The energy spectrum shows the separation energy for knocking out a proton from the $1s$ (broad peak) or the $1p$ (sharp peaks) shells. The two sharp peaks, which correspond to protons from the $1p$ shell, show the spin-orbit splitting in this shell. Knocking out a proton from the $1p_{\frac{1}{2}}$ shell of ^{16}O leaves ^{15}N to the ground state (peak at 0 MeV excitation energy). The angular correlation spectra of protons originating from the ground state and the 6.4 MeV excited state are also shown in Fig. 2.9 together with calculations. The angular correlation of the two outgoing protons is related to the angular momentum of the state where the knocked-out proton originated from.

Quasi-free scattering with fast radioactive beams can be realised by bombarding a proton target (ideally liquid hydrogen) with high energy ions (mass A) and measuring the (A−1) residue and the two outgoing nucleons in coincidence. To apply the formulae described above in inverse and relativistic kinematics some modifications are required since the projectile is no longer the proton but the ion of interest which now moves with high velocity and hits the proton target. Both experimental and theoretical techniques for studying quasi-free scattering reactions in inverse kinematics are currently being developed.

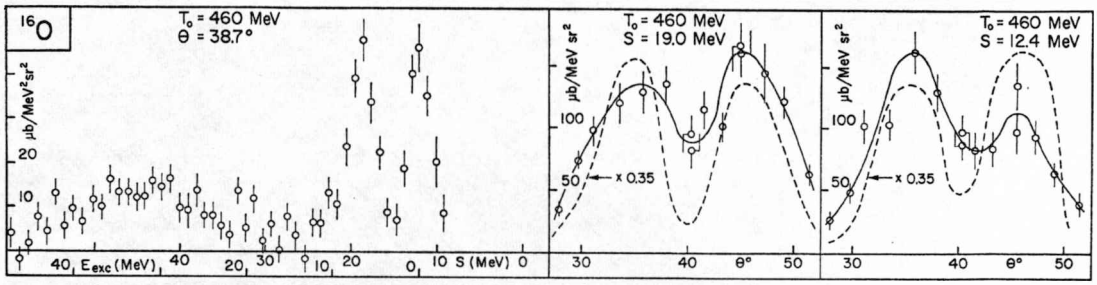

Figure 2.9: Separation- and excitation-energy spectrum (left) and angular correlations of the two outgoing protons for the ^{16}O(p,2p)^{15}N quasi-free scattering reaction. Calculations for the angular correlations are also shown with dashed lines.

2.3.3 Complementarity of one-nucleon removal and quasi-free scattering reactions

At first sight it might appear that there is a big overlap in the physics case that one can study with nucleon-removal reactions and quasi-free scattering (e.g. extraction of single-particle occupancies), but there are some essential differences which make each of them more or less appropriate for certain cases. Most importantly, the use of a light target (one-nucleon removal reaction) instead of protons (quasi-free scattering reactions) limits the reaction to the surface of the nucleus due to strong absorption. With the proton target the absorption is much less and nucleons from inner shells can be knocked out as well. In the case of halo nuclei the one-nucleon removal reactions have been a particularly successful tool since the halo nucleon spends most of the time away from the core. It is expected though that for deep single-particle states in the nucleus the quasi-free process should be a better probe. This advantage of the quasi-free scattering is over the pick-up and stripping reactions as well.

The energy range of the incoming ion in which the two reactions take place is also quite different, with the quasi-free scattering requiring a much higher energy, i.e. few hundred MeV/nucleon for quasi-free and few tens of MeV/nucleon for nucleon removal reactions. In this higher energy region, the cross section for nucleon-nucleon reactions is minimal and this implies that the incoming and the two outgoing nucleons of the quasi-free process have low probability to interact with the other nucleons of the nucleus, i.e. low re-scattering and less distortion in the momentum measurement. Higher projectile energies have also the advantage of a simpler theoretical approach and a better understanding of the observables.

The detection of the heavy residue and the prompt γ rays is common for the two reactions. However, the coincidence measurement of the two outgoing nucleons, only in the case of the quasi-free (p,2p) and (p,pn) scattering, provides an additional measurement of the momentum and energy of the bound nucleon, which should allow for a much cleaner determination of the observables. It should be mentioned here that a

great advantage of using quasi-free scattering in inverse kinematics compared to normal kinematics is the ability of measuring also the remaining core and not just the two outgoing nucleons, providing a full kinematical measurement. In the case of normal kinematics the residual core remains in the target and thus it is difficult to measure it. This means that quasi-free scattering in inverse kinematics could become a valuable tool even for stable nuclei, which have been measured so far in the target position. Finally, it is worth mentioning that the quasi-free hadronic scattering in conjunction with polarised proton targets could provide a spin-orbit coupling measurement, due to its strong spin dependence [50, 54, 55].

It is therefore clear that nucleon removal and quasi-free reactions are complementary and each one is optimum for probing different parts of the nucleus. Nucleon removal in inverse kinematics has already been an established spectroscopic tool which has extended our knowledge of nuclear structure towards the drip lines. Quasi-free scattering in inverse kinematics has only been attempted recently and its full capabilities will be realised in the future R^3B setup at FAIR/NuSTAR, Germany.

The essential parts of the experimental setup in order to perform these type of reactions (one-nucleon removal and quasi-free scattering reactions) in inverse kinematics with fast radioactive beams produced in-flight by fragmentation are: a fragment separator so that one can select and unambiguously identify the incoming ion on an event-by-event basis, a high resolution spectrometer after the target to identify the heavy reaction residues and measure their momentum distributions, and a γ-ray detection system to detect the prompt γ rays and allow the tagging on the individual final states of the residue after the reaction. Full quasi-free scattering measurements require an additional detection element, the proton-recoil detector which should surround the target area in order to measure angular and energy correlation of the two outgoing protons [56].

Chapter 3

Experimental apparatus

This chapter unfolds following the trajectory of the beam, starting with the production and acceleration of the ions constituting the primary beam, continuing with the in-flight production, separation and identification of the secondary radioactive beam, and finally reaching Cave C, where the secondary ions react with the secondary reaction target and the subsequent reaction residues are detected. In this way the main parts of the experimental apparatus at GSI are presented.

3.1 The GSI accelerator system

First the ions constituting the primary beam are generated from ion sources located at the beginning of the beam path. The UNIversal Linear ACcelerator (UNILAC) is then responsible for pre-accelerating these ions up to energies of 18 MeV/nucleon and injecting them into the Heavy Ion Synchrotron (SIS[1]) for further acceleration (Fig. 3.1). The maximum energies that the SIS can deliver are defined by its maximum magnetic bending power of 18 Tm. With such magnetic bending power a maximum energy of 1 - 4.5 GeV/nucleon can be reached depending on the ion species. This accelerator complex, as briefly described above, can accelerate all stable ions from hydrogen to uranium, delivering high quality stable beams, which can be used for in-flight production of secondary radioactive beams by hitting a thick production target at the exit of the SIS.

The fragmentation of the primary beam on the production target results in a secondary beam consisting of a large number of different nuclides, which need to be selected and identified on an event-by-event basis. For this purpose these beams pass through the FRagment Separator (FRS), which is described in the following section.

[1]German acronym for SchwerIonenSynchrotron.

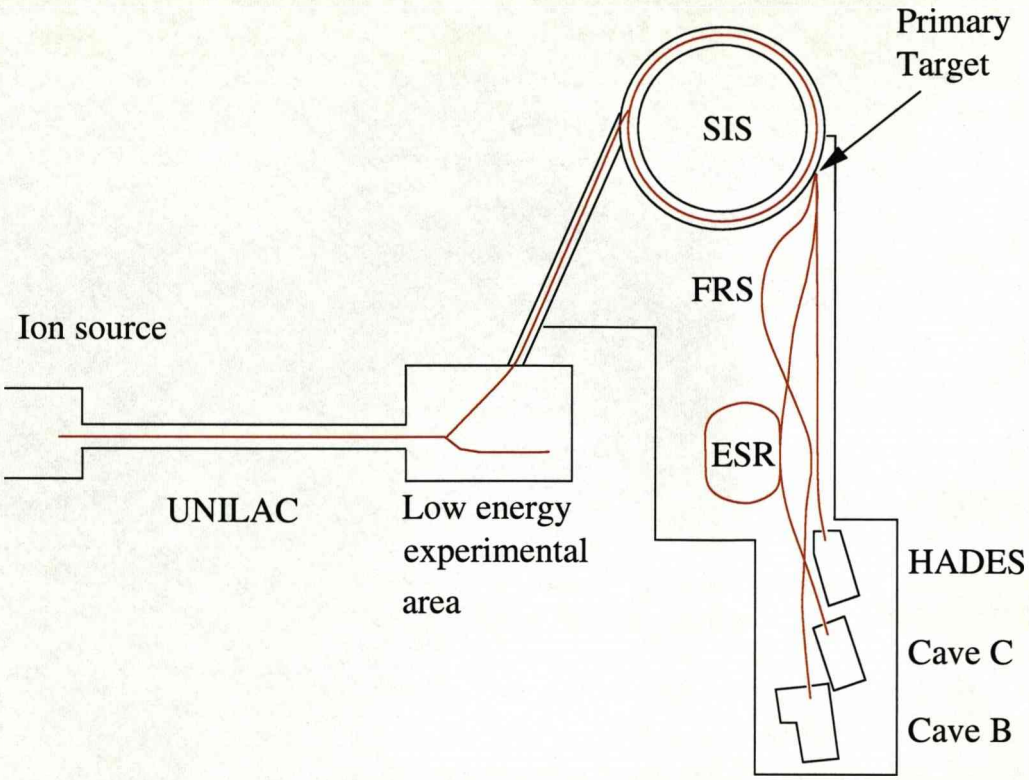

Figure 3.1: The GSI facility. Ion beams are produced at the ion source and accelerated by the UNILAC. They are used either for low energy experiments or post-accelerated by the SIS and used for higher energy experiments. Radioactive ion beams are produced via fragmentation of the post-accelerated beam on the primary target.

3.2 The Fragment Separator (FRS)

The FRS [57] is a high resolution zero-degree magnetic spectrometer consisting of four large dipole magnets and a set of quadrupoles and sextupoles (see Fig. 3.2). Passing through the first stage of the FRS (i.e. the two first dipole magnets of the separator) the ions are analysed according to their magnetic rigidity ($B\rho$), so that fragments of the same momentum-over-charge ratio will be focused on the same horizontal position (x) in the intermediate focal plane (F2), called the dispersive focal plane. Their time, energy loss and horizontal position are measured at F2 using scintillator detectors (S2, FGR). The second stage (consisting of the last two dipole magnets) is set to cancel the dispersion of the first one, so that the ion-optics of the whole system are achromatic at the exit of the FRS, called the achromatic focal plane (F8). At F8, time, energy loss and horizontal position are measured again using the scintillator detector S8.

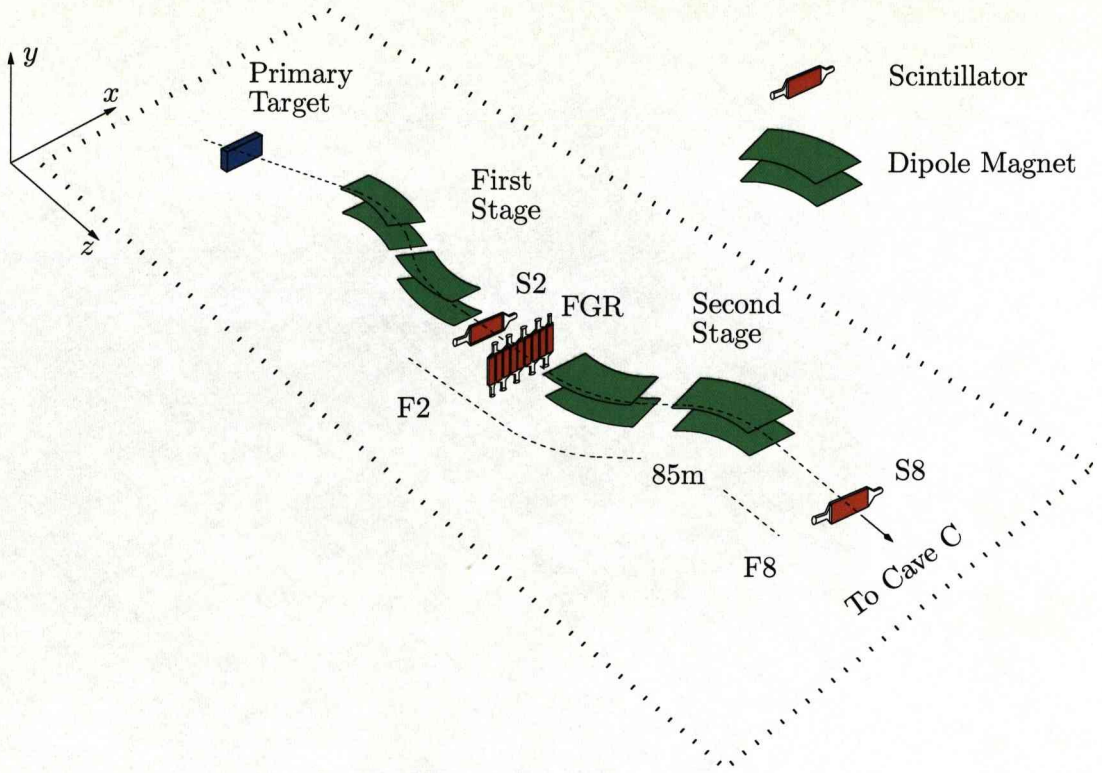

Figure 3.2: The FRS setup. The post-accelerated primary beam from SIS is fragmented on the primary target and the produced secondary ions are selected (first stage) and identified (second stage) by the FRS before being transferred to Cave C.

3.3 The LAND/ALADIN setup in Cave C

Selected and identified by the FRS, the secondary ions are transferred to Cave C where the secondary reaction target is located. As illustrated in Fig. 3.3, in front of the target there are detectors for time (POS detector), energy-loss and two-dimensional (2D) position measurements (PSP1, PSP2 detectors[2]). Around the target a CsI array (CS) is placed for the detection of prompt γ rays and protons. Emitted protons, before reaching the CsI detectors, are first registered in plastic scintillators (CV) that surround the target area. Another energy-loss and 2D position measurement is performed (PSP3) between the target and the ALADIN (A Large Acceptance DIpole magNet) magnet for the projectile-like fragments. Charged fragments are then bent by the magnetic field (ALADIN dipole magnet) according to their magnetic rigidity and their horizontal displacement is measured after the magnet with fibre detectors (GFI1, GFI2, GFI3 detectors[3]). The charged fragments finish their flight, delivering time, energy-loss and position measurements (TFW[4], NTF[5] detectors), while the neutrons continue their

[2]PSP stands for Position Sensitive silicon Pin diode.
[3]GFI is a German acronym for Große FIberdetektor.
[4]Acronym for Time-of-Flight Wall.
[5]Acronym for New Time-of-Flight wall.

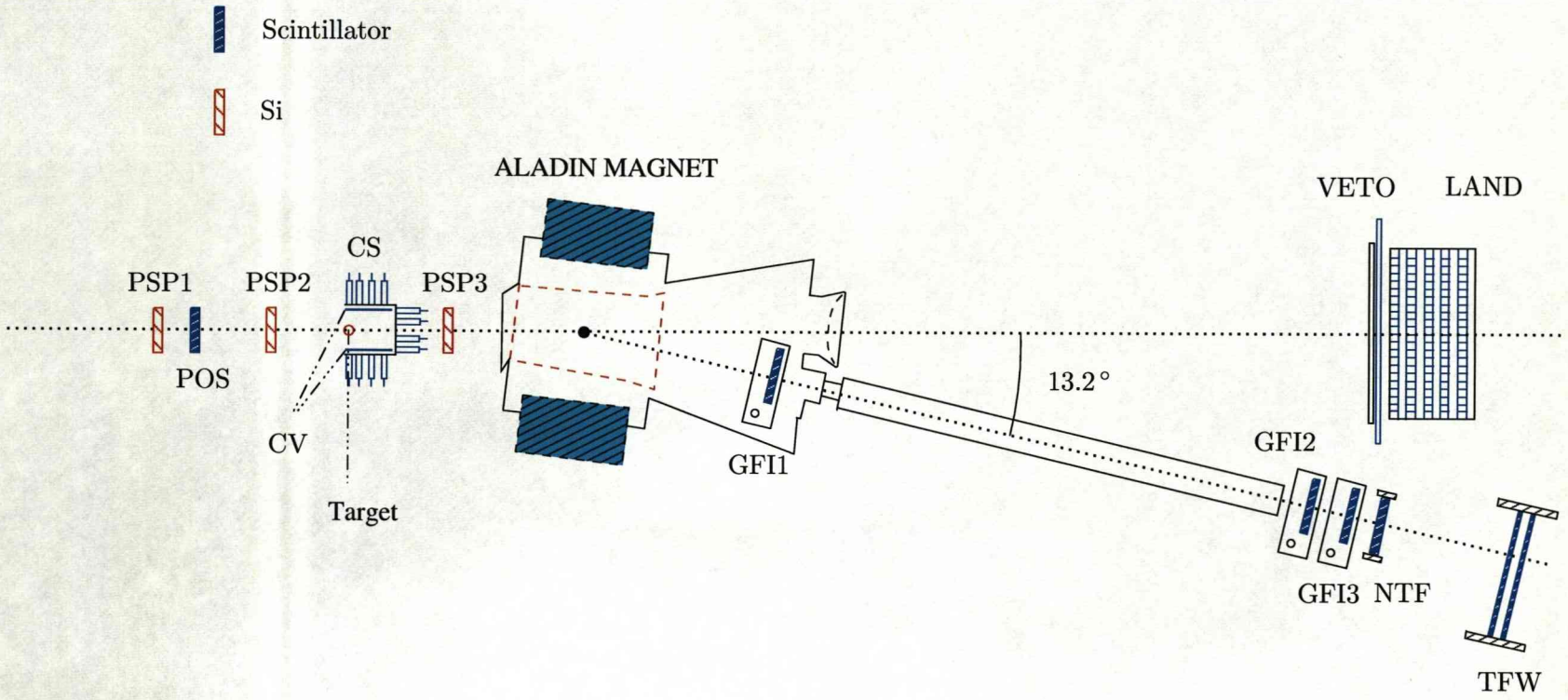

Figure 3.3: Main parts of the LAND/ALADIN setup in Cave C. This setup provides full kinematical measurements. The secondary ions are tracked on target with the use of Si detectors (PSP), heavy reaction fragments are deflected by the ALADIN magnet and measured by fibre detectors (GFI) and time-of-flight walls (NTF, TFW), neutrons are registered in the LAND detector, while γ rays are detected by the CsI array (CS) which, in conjunction with the plastic scintillator detector (CV), can also detect protons.

flight, unaffected by the magnetic field, and hit a Large Area Neutron Detector (LAND) located 15 m downstream of the target where their time, energy and position are measured.

The structure and the main characteristics of all the individual detectors used in the present experiment are briefly discussed in the following sections. These sections are organised such that the detectors involved in the same identification or tracking procedure are grouped together; however, this categorisation is not strict since most detectors are used for more than one purposes.

3.4 Detection system for the incoming secondary beam

The identification and tracking of the incoming beam is achieved with a series of position, energy-loss and time-of-flight measurements both at the FRS and at the entrance of Cave C. Position and time-of-flight measurements are needed for the determination of the mass-over-charge (A/Z) ratio, while energy-loss measurements give the charge (Z) of the nuclide[6]. Precise 2D position measurements close to the target are used to reconstruct the trajectory of the incoming ions, which allows the recovery of the momentum resolution.

3.4.1 Mass identification of the ions

The identification of the incoming secondary beam in terms of mass-over-charge ratio requires knowledge of the velocity (β) of the ion and its magnetic rigidity ($B\rho$). The velocity is calculated by measuring the time difference (time of flight) between plastic scintillator detectors S2, FGR and S8 placed along the FRS spectrometer (see Fig. 3.2) and POS at the entrance of Cave C (see Fig. 3.3). The $B\rho$ for each ion is determined by measuring the horizontal displacement of its trajectory at the dispersive focal plane (F2) of the FRS (FGR, S2 detectors) and at the achromatic focal plane (F8) at the exit of the FRS (S8 detector) with respect to a reference trajectory of an ion of $B\rho_0$.

The S2 and S8 detectors

The S2 and S8 detectors are of similar geometry (paddles), consisting of a rectangular plastic material with dimensions of $218.6\times80\times1$ mm^3 and $200\times80\times1$ mm^3, respectively, and placed in the beam line with their long side along the x axis and their short one along the z axis, as shown in Fig. 3.2. Two fast PhotoMultipliers (PMs) are mounted on each scintillator at the left and right ends of the long side of the paddle, delivering time and energy signals. These detectors, apart from time and energy-loss information, can

[6]For beam energies of a few hundred MeV/nucleon produced at GSI the ions are fully stripped of electrons after reacting with the primary target, thus the charge (Q) of the ion is equal to the atomic number of the nucleus.

provide also x-position information by subtracting the times and dividing the energies of the two PMs of the same detector, as explained in more detail in Section 4.2.1.

The FGR detector

The finger (FGR) detector is a multi-strip scintillator detector, consisting of 15 long plastic paddles with dimensions of 13×80×1 mm^3 each, placed in the beam line with its paddles' long side along the y axis. PM tubes are mounted at the end of the paddles in such a way that light from two neighbouring paddles is collected by a single PM at each end (Fig. 3.4). In this way a synchronisation of the time signals of the paddles is possible. Use of this detector allows for a "digital" position determination by simply checking which PMs have fired. Although position resolution from this detector is limited to the width of the paddle, it needs no calibration and can handle high rates of incoming particles, in contrast with the S2 scintillator.

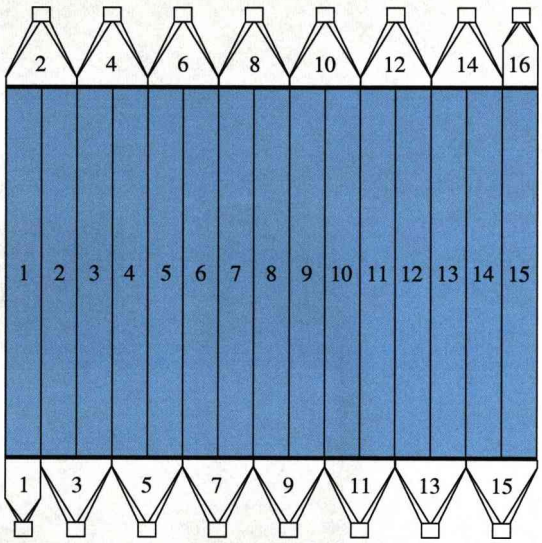

Figure 3.4: The finger detector, consisting of 15 paddles, placed at the dispersive focal plane (F2) of the FRS spectrometer for measuring the horizontal displacement of the fragments.

The POS detector

The POS detector is a square (5×5 cm^2) plastic scintillator 200 μm thick with four fast PMs mounted at each side (Fig. 3.5). It is used for timing purposes and it is placed in the beam line $\sim$ 200 cm upstream of the target, such that the PMs point at right, up, left and down with respect to the beam direction, as illustrated in Fig. 3.5.

3.4.2 Charge identification of the ions

When charged particles are moving through matter they lose energy mainly through electromagnetic interaction with the electrons of the atoms of the material, which are

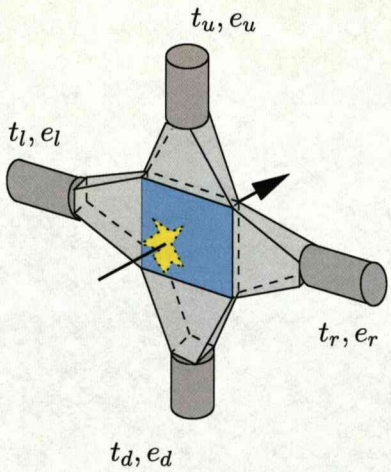

Figure 3.5: The POS detector, mainly used for timing purposes, placed before and close to the target [58].

then excited or ionised. The specific energy loss of a particle with charge eZ and velocity v when moving through matter is given by the Bethe-Bloch formula [59]

$$-\frac{dE}{dx} = \frac{4\pi e^4 Z^2}{m_0 v^2} Nz \left[\ln \frac{2m_0 v^2}{I} - \ln\left(1 - \frac{v^2}{c^2}\right) - \frac{v^2}{c^2} \right], \tag{3.1}$$

where N, I and z are the number density[7], ionisation potential and atomic number of the material, e and m_0 are the charge and rest mass of the electron, respectively. Thus, according to Eq. 3.1, the charge of the incoming ion can be determined through a combination of velocity and energy-loss measurements.

Detectors delivering energy-loss information before the target are the plastic scintillators S2, S8, FGR and POS detectors (described earlier) and most importantly the Si detectors PSP1 and PSP2, which are described in the following section.

3.4.3 Projectile tracking

The incoming ions collide with the target with a certain angle and it is important to measure this angle event by event in order to know precisely the momentum of the projectile in the reaction. It is also important to know with good precision the position of the incoming ion on target (x_0, y_0), which can later serve as a starting point for the determination of the trajectory of the outgoing heavy reaction fragments through the dipole magnet. Position on target is also used in order to reject events that are not hitting the target itself but the target frame. These 2D position measurements close to the target are performed using two Si detectors (PSP1 and PSP2).

[7]Number of certain objects per volume.

The PSP detector

PSP is a large Position Sensitive silicon Pin diode of a high resistivity n-type Si, with a 300 μm thick Si wafer. It has a square shape and an active area of 4.5×4.5 cm^2. Implementation of boron ions into one side of the n-type Si forms a p-n junction, which serves as an anode, while the other side serves as a cathode. The charge deposited in the detector is read out from all four corners of the anode side, Q_1, Q_2, Q_3, Q_4 (commonly referred to as position signals, Fig. 3.6), allowing the reconstruction of the position where the incident ion passed. The charge is also collected from a contact on the cathode side (Q), which is used to measure the total energy loss of the incident particle through the detector from which its charge (Z) can be obtained.

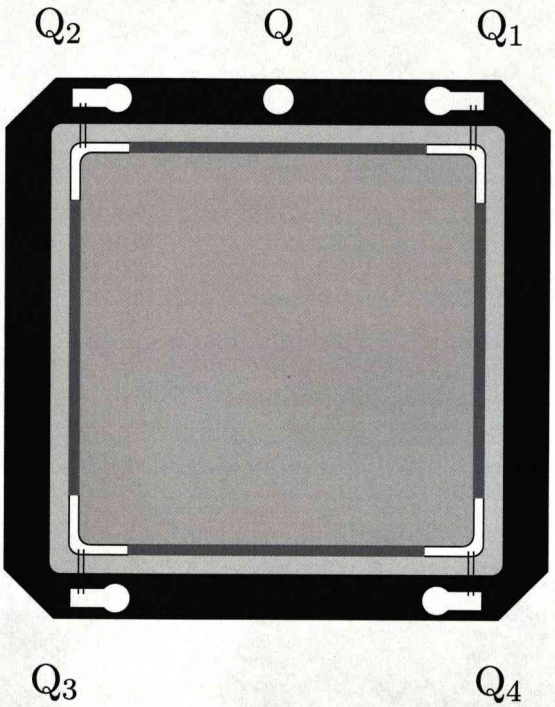

Figure 3.6: The anode side of the PSP detector. The charge generated in the detector is collected by the four anodes Q_1, Q_2, Q_3, Q_4 indicated on the figure and by a cathode Q at the back side of the detector.

The PIX detector

The pixel detector (PIX) is a mask consisting of 21×21 square scintillator pixels. The pitch between the pixels is 2 mm and the size of each side of a pixel is 0.5 mm, as shown in Fig. 3.7. The pixels consist of scintillating material and the light produced is guided to a PM, which is mounted at one side. The pixel detector is used in order to provide a reference to calibrate in position the PSP detectors. Three pixel masks are mechanically inserted in the beam line in front or behind each of the PSP detectors during specially performed runs, referred to as the pixel calibration runs.

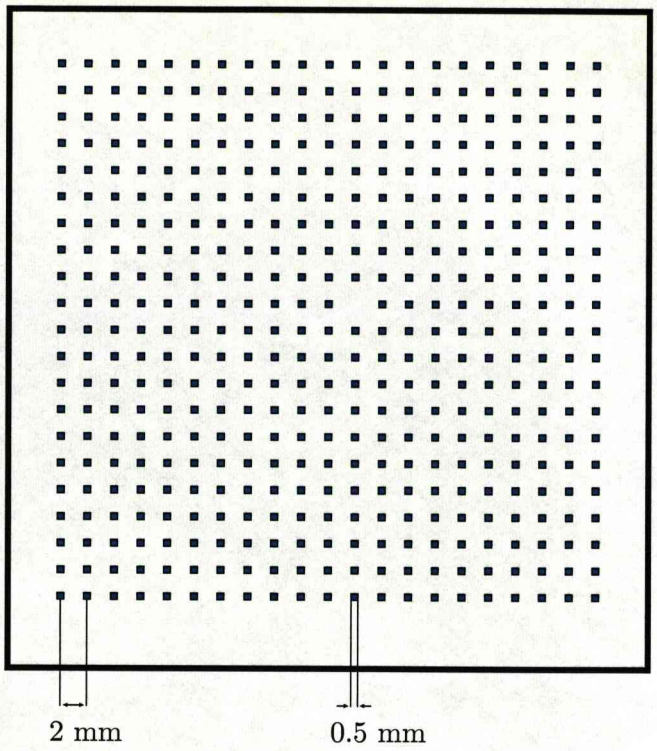

Figure 3.7: Schematic drawing of the pixels on the active pixel mask (PIX detector).

3.5 Detection system for the heavy reaction products

The reaction products that do not differ much in mass from the projectile mass are called heavy reaction products; other light reaction products could be for example neutrons, γ rays and protons, and their detection system is described in Section 3.6. The heavy reaction products need to be identified, in the sense of charge and mass, and also have their trajectory determined, as in the case of the incoming beam described in Section 3.4.

3.5.1 Charge identification

In order to determine the charge of the heavy reaction products, an energy-loss measurement is performed by a third Si detector (PSP3) close to the target and by the TFW and NTF detectors at the end of the track (see Fig. 3.3).

3.5.2 Mass identification and tracking

For the heavy reaction products, precise tracking of the particles through the dipole magnet (ALADIN) is essential for distinguishing the different masses. The determination of the trajectory of the charged particles through the dipole magnet requires a combination of position measurements before (target position (x_0, y_0) and PSP3) and after the magnet (GFI1, GFI2, GFI3). Time-of-flight measurements between the time

on target (t_0) and the time measured by NTF and TFW at the end of the track are also needed for resolving fragments from neighbouring masses.

The GFI detector

The GFI detector is a large area (50×50 cm^2) scintillator fibre detector consisting of almost 500 thin and long (0.1×50×0.1 cm^3) scintillator fibres placed parallel and close to each other, as illustrated in Fig. 3.8(top). Each fibre is coated with white paint to minimise cross talk between neighbouring fibres, which, however, causes a small reduction in the efficiency of the detector. Fibres are glued from one end to a mask in a sequential way, such that each fibre has a distinct (u, v) coordinate on the plane of the mask, as shown by the numbering in Fig. 3.8(bottom). This end is then coupled to the face of a Position-Sensitive PM (PSPM), which consists of a photocathode, mesh-type dynodes and a multi-wire anode with 18 wires in the u direction and 16 in the v direction, creating a rectangular grid. When a charged particle passes through a fibre it causes scintillation light which is guided on the mask where it appears as a light spot on the plane of the photocathode. The energy signal of each wire is read out and used to reconstruct the (u, v) coordinate of the light spot on the plane of the photocathode and from there to associate it with the fibre that was hit. The other end of the fibre is coupled to an ordinary PM for triggering purposes [60].

The TFW and NTF detectors

Time measurement of the heavy reaction products and also energy-loss information are obtained using the TFW (Time-of-Flight Wall) and NTF (New Time-of-Flight wall) detectors. The TFW detector consists of two planes placed perpendicular to the beam direction, one with 18 horizontal paddles and one with 14 vertical paddles, as illustrated in Fig. 3.9. The size of the horizontal paddles is 189×10×0.5 cm^3 and of the vertical ones is 147×10×0.5 cm^3. Each paddle is read out by two PMs mounted at each end of the long side of the paddle, delivering time and energy signals. By combining the two PM signals it is also possible to obtain position information. Position resolution is not sufficient (1 - 2 cm) to significantly contribute to the tracking of the particle; however, it plays an important role in the calibration procedures described in Section 4.2.1. The NTF detector is built using the same principles as the TFW detector; its paddles are eight horizontal and eight vertical and their dimensions are smaller (50×6.25×0.5 cm^3). Due to high-quality modern PMs which are mounted at each side of the paddle and due to the smaller paddle size, it is expected that the NTF detector should give a better time and energy resolution than the TFW detector. In the present experiment, however, only one plane of the NTF detector is used, which significantly affects the overall performance of the detector.

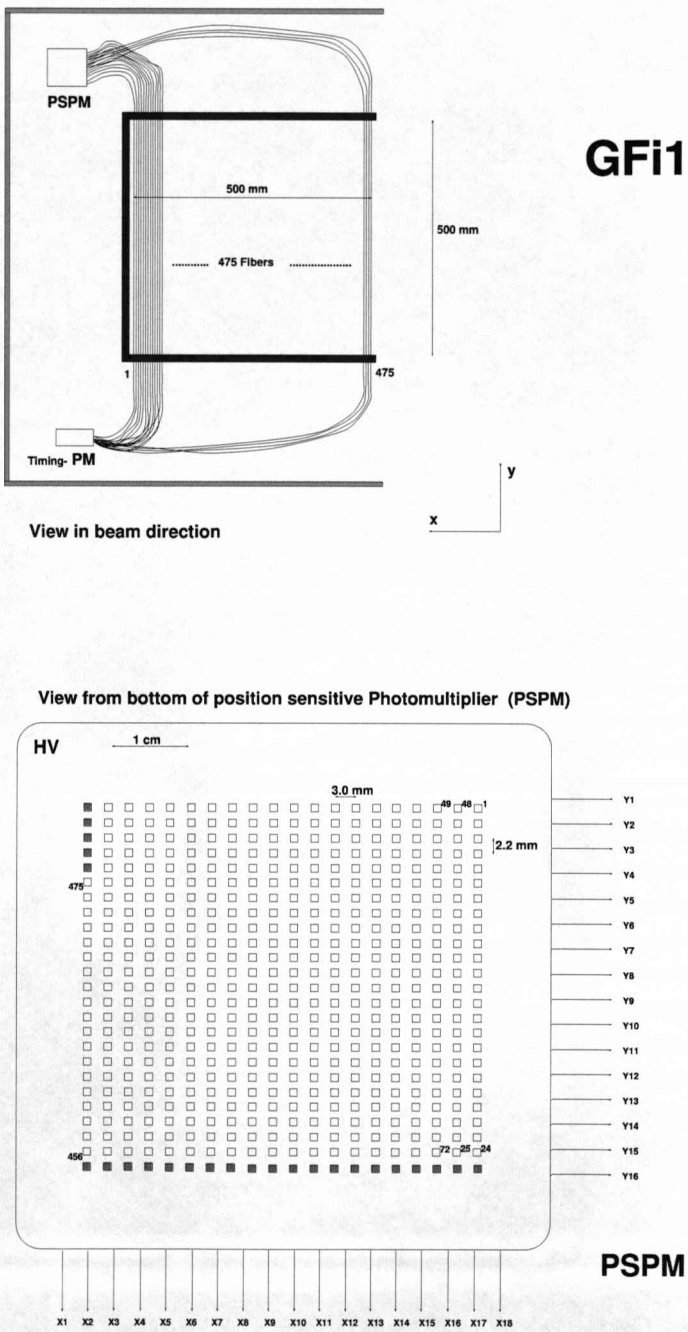

Figure 3.8: The GFI detector (top) and the mask used to guide the fibres on the PSPM cathode (bottom) [61].

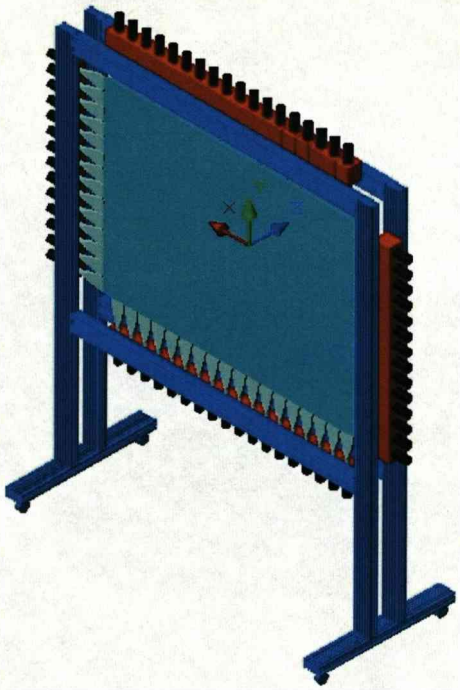

Figure 3.9: Schematic drawing of the TFW detector [62].

3.6 Detection system for the light reaction products

3.6.1 γ rays

The CS detector

For the detection of the prompt γ rays a CsI array is used. It consists of 144 CsI crystals, which are read out individually by PM tubes. The particular shape of the crystals and their arrangement is such that it compensates for the Lorentz boost of the γ rays emitted from the high energy particles (see Fig. 3.10). The γ rays emitted in-flight are also significantly Doppler broadened; however, the high granularity of the detector allows for recovering part of the energy resolution.

3.6.2 Protons

The CS and CV detectors

In order to detect protons from the reactions, twelve plastic paddles ($50\times5\times0.5$ cm^3) are placed around the target parallel to the beam axis (Fig. 3.11), such that they cover in ϕ a full 2π angle and in θ they cover angles between $10\,^\circ$ and $90\,^\circ$. Each paddle is read out by a single PM tube, so the position of the hit cannot be reconstructed and the energy loss of the particle cannot be measured. Thus, they can serve mainly for triggering and timing purposes. Although a signal from the CV detector cannot provide much information on its own, when used in conjunction with the signal of the

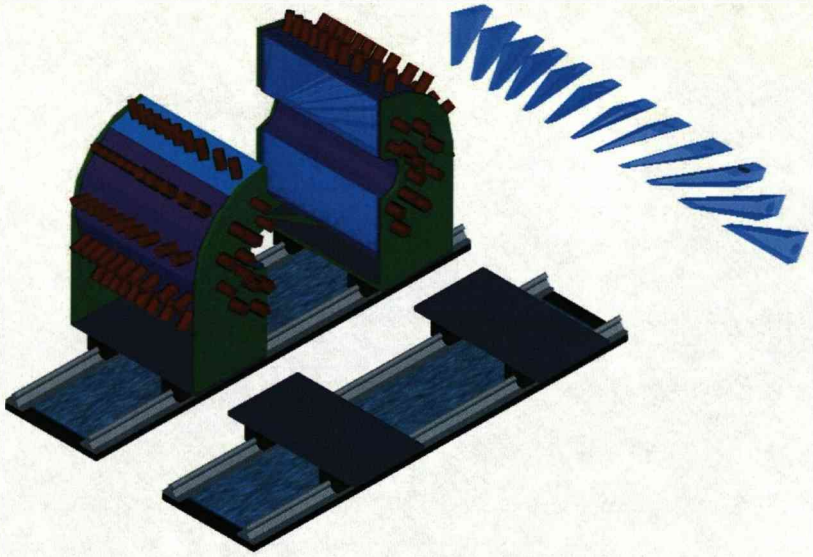

Figure 3.10: Schematic drawing of the CsI array [63].

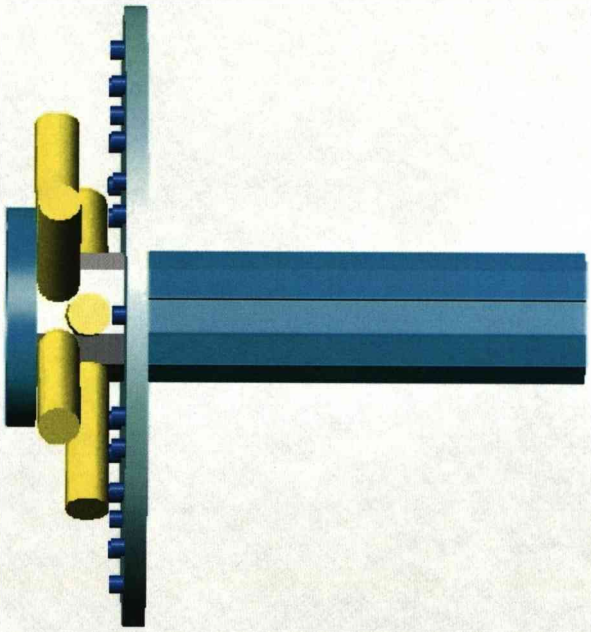

Figure 3.11: Schematic drawing of the CV detector.

CsI array, it helps to distinguish charged particles that continue their trajectory in the CsI detectors from γ rays and neutrons, since the latter particles will not be registered in the plastic CV detector. In this way the CsI crystals can provide rough angle and energy information for the outgoing protons.

3.6.3 Neutrons

The LAND detector

The Large Area (200×200×100 cm^3) Neutron Detector (LAND) [64] consists of 10 planes with 20 specially designed paddles (200×10×10 cm^3) each, as illustrated in Fig. 3.12. Read-out is realised with two PMs at each end of a paddle, providing time and energy signals. The paddles in the same plane are placed parallel and close to each other and the planes are packed together such that paddles of subsequent planes are always perpendicular to each other. This arrangement allows for a three-dimensional (3D) position reconstruction in vertical (y), horizontal (x) and parallel to the beam (z) directions. The total depth of the detector, considering all planes, becomes then 100 cm which allows detection of 100 - 1000 MeV neutrons with a 70 - 95% efficiency. The specially designed paddle is a multi-layer structure of iron and plastic scintillator layers. The iron layers significantly increase the efficiency of the detector and also improve re-absorption of secondary charged particles.

The Veto detector

The LAND detector is normally used in conjunction with a veto detector for charged particles, which is placed in front of LAND. It consists of 20 scintillator paddles (200×10×0.5 cm^3) arranged in a plane covering the full front face of the LAND detector. Its purpose is to veto the charged particles that enter the LAND detector, allowing for a cleaner neutron detection.

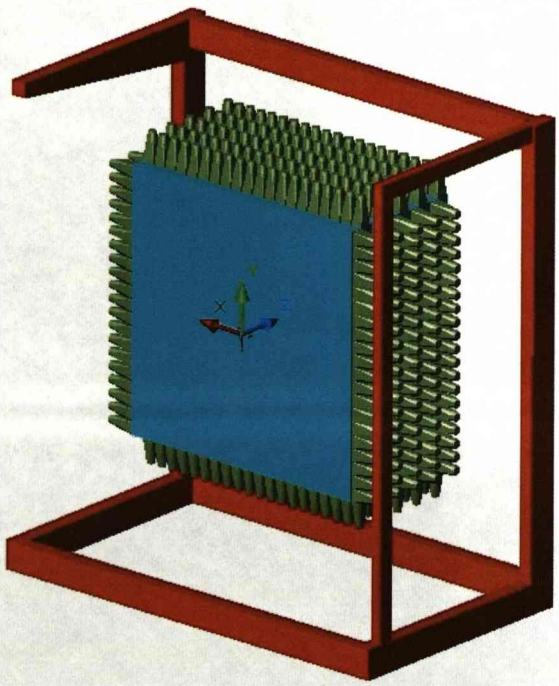

Figure 3.12: Schematic drawing of the LAND detector [65].

Det.	Description	Size(x,y,z)[cm]	Pos.[cm]	Measurement	σ
SCI1 (S2)	Org. scintil. paddle placed at FRS(F2) for β and $B\rho$ measur.	21.86×8.0×0.1	-14130.0	t de x	100 ps 4.0 % 1.0 cm
FGR	15 org. scintil. paddles placed at FRS(F2) for β and $B\rho$ measur.	19.5×8.0×0.1	-13948.0	t de x	200 ps 4.0 % 0.4 cm
SCI2 (S8)	Org. scintil. paddle placed at FRS(F8) for β and $B\rho$ measur.	20×8.0×0.1	-5590.0	t de x	100 ps 4.0 % 1.0 cm
PSP1	Square Si placed before the target for 2D position and Z measur.	4.5×4.5×0.03	-224.6	– de x, y	– 1.0 % 0.02 cm
POS	Square org. scintil. placed (close) before target for β measur.	5.0×5.0×0.02	-194.3	t de x, y	80 ps 4.0 % 1.0 cm
PSP2	see PSP1	4.5×4.5×0.03	-68.8	– de x, y	– 1.0 % 0.02 cm
ROLU	4 rectangulars of org. scintil. for veto-ing unfocused beam.				
CV	12 org. scintil. paddles placed around target "inside" CS detector	50×5.0×0.5	0.0	t de ϕ	100 ps – 30 °
CS	144 CsI crystals around the target for γ-ray and proton detection		0.0	t de ϕ, θ	1000 ps 10 % 30 °, 7 °
PSP3	see PSP1 but placed after target and before magnet	4.5×4.5×0.03	77.5	– de x, y	– 1.0 % 0.02 cm
GFI1	475 org. scintil. fibres placed after the magnet for x measur.	50×50×0.1	353.0	– – x	– – 0.03 cm
GFI2	see GFI1	50×50×0.1	1200.0	x	0.03 cm
GFI3	see GFI1	50×50×0.1	1259.0	x	0.03 cm
NTF	Wall of 8 org. scintil. placed after GFIs, for β and Z measur.	50×50×0.5	1287.1	t de x, y	100 ps – –
TFW	Wall of 18x16 org. scintil. paddles, placed after NTF for β and Z measur.	189×147×1.0	1459.0	t de x, y	100 ps 1.5 % 2.0 cm
LAND	10 planes of 20 paddles from org. scintil. and iron for neutron detection	200×200×100	1460.7	t de x, y, z	200 ps 5.0 % 4.0 cm

Table 3.1: Description of the detectors used in the present (S287) experiment. Their position is given relative to the target position or to the centre of the magnet for detectors placed before or after the magnet, respectively.

3.7 Triggers

The different triggers used in the present experiment were generated by combining the logical signals in the way shown in Fig. 3.13. The requirements for the logical signals are given in Table 3.2 while some remarks on the specific use of each trigger are given in Table 3.3. One can divide these triggers into two main categories: the on-spill and off-spill triggers, with the latter ones used only for calibration purposes.

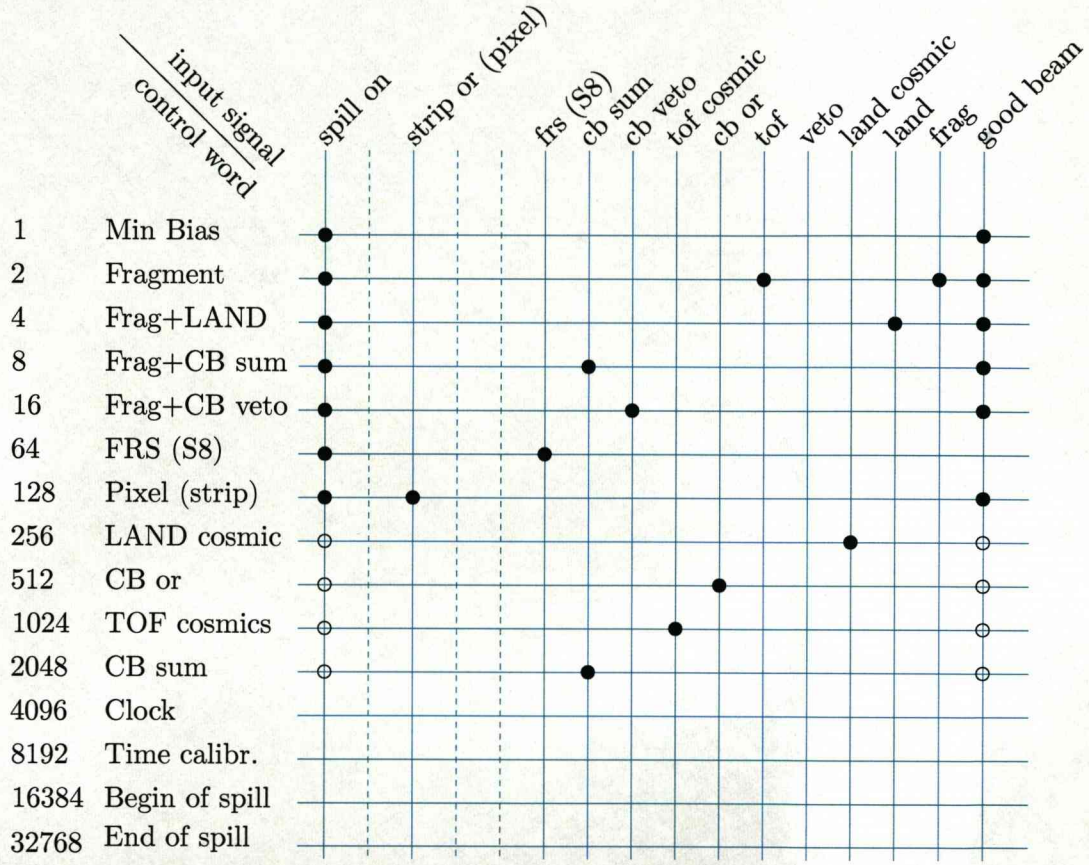

Figure 3.13: The triggers and the corresponding coincident logical signals are shown (filled circles). Some triggers require anti-coincidence of logical signals (empty circles). The first column on the left shows the corresponding number for each trigger (Tpat).

Signal name	Requiring signal from...
good beam	the POS detector with anti-coincidence of the active beam collimator (ROLU)
frag	the heavy fragment detector (GFI)
land	the neutron detector (LAND)
land cosmic	high multiplicity in LAND detector
veto	not used
tof	the heavy fragment TFW detector
cb or	any CsI crystal (used for calibration with a source)
tof cosm	cosmic ray in tof
cb veto	the proton detector (CV)
cb sum	the sum from all CsI crystals to be above a certain threshold
frs (s8)	the last FRS scintillator (S8)
strip or (pixel)	the active pixel mask (pixel calibration runs)
spill on	the accelerator for begin and end of spill

Table 3.2: The names and the requirements of the logical signals.

Trigger name	Notes
Min Bias	minimum requirements for accepting a physics event
Fragment	fragments can be reconstructed
Frag+LAND	good beam and a neutron candidate in LAND
Frag+CB sum	good beam and the sum of CsI above some threshold
Frag+CB veto	good beam and the plastic CV detector, proton candidate
FRS (S8)	for beam intensity and transmission monitoring
Pixel (strip)	for pixel calibration runs
LAND cosmic	for calibrating LAND with cosmic rays that penetrate it, spill off
CB or	for calibrating with a γ source, any CsI crystal, spill off
TOF cosmics	for calibrating the TFW detector with cosmics, spill off
CB sum	sum of the CsI array and spill off
Clock	for determining the pedestals in the QDCs, spill off
Time calibr.	for calibrating the bin of the TDCs, spill off
Begin of spill	from the accelerator
End of spill	from the accelerator

Table 3.3: The trigger names and some remarks on their main purposes.

Chapter 4

Calibrations

There has been a great deal of effort expended and initiated by H. T. Johansson [66], in the last few years to rewrite the analysis code (data handling, calibration, reconstruction routines, etc.) in a more general and hopefully transparent way (*land02* framework) that significantly enhances "re-usability" and automation of the code segments. In this spirit, the *land02* framework can be effectively used for analysis of past, present and future experiments performed at the LAND/ALADIN setup or the future R^3B setup at the FAIR facility.

In this type of experiments many complicated calibration procedures need to be applied first, before useful physical information can be extracted from the data[1]. Most calibration and reconstruction procedures have been built from "scratch" within the *land02* framework with completely new approaches. Hence, this chapter is exclusively dedicated to describing these procedures and often comparing them with their ancestors. The results presented in this thesis are amongst the first to be calibrated, reconstructed and partially analysed within the *land02* framework. Although the following sections are not aiming to present the calibration and reconstruction procedures in the instructive and detailed way of a user's manual, they can serve as a guide for the principles behind the calibration and reconstruction routines, the steps required and for pointing out the specific behaviour of the detectors that require additional care. Calibrations are performed in three main steps:

- Time calibration of all time signals using a clock, i.e. TDC (Time-to-Digital Converter) gain calibration (TCAL level, time in ns), and zero noise determination of QDC (Charge-to-Digital Converter) energy channels using a pulse generator are performed. At this level the data are treated as time (t) and energy (e) channels homogeneously, no matter which detector they come from.

- Internal/external calibration of the detectors is performed, such that they deliver for each event (or for each hit in the case of a multi-hit capable detector) energy,

[1] For simplicity in this thesis the terms run, file, etc. are used instead of data-run, data-file, etc.

time and position information. Position is first reconstructed in internal ((u, v) coordinates or paddle number (i, j)) (DHIT level) and then in external (x, y) (HIT level) coordinate systems.

- Synchronisation and alignment of the detectors with each other is performed, i.e. finding offsets from cables etc., flight paths and angles.

In this chapter the aforementioned calibration steps are presented in Sections 4.1, 4.2 and 4.3, respectively. Most of these calibration steps are performed within the *land02* framework. Although a detailed description of the data structures and the data flow within this framework is beyond the scope of this thesis, the detailed scheme of Fig. 4.1 [58] is shown here as a guide for the data reconstruction levels and the calibration steps mentioned in this chapter. Throughout the experiment the calibration parameters vary significantly and require additional monitoring and corrections; this time-dependent calibration is discussed in Section 4.4. In Sections 4.5 and 4.6 the track-level calibrations and reconstructions are described. Finally, in Section 4.7 the need for an advanced tracking algorithm is discussed.

4.1 TDC gain calibration

The purpose of this calibration is to measure precisely the size of each bin of the TDC, minimising the error while transforming the time from channels to ns. In this experiment TDCs with nominal values of 0.025, 0.05 and 0.2 ns/bin are used. In past LAND experiments this calibration procedure was performed using a time calibrator device, which produced a start and a stop signal with an adjustable step in between [67]. In this experiment this calibration is achieved using a very precise clock, which runs during the whole experiment and provides a continuous monitoring of this gain. Signals from the clock for one run are shown in Fig. 4.2. A typical graph of such calibration is illustrated in Fig. 4.3 for the four time channels of the POS detector by selecting the appropriate trigger for time calibrator (Tcalt) events. Typical deviations from the nominal value are of the order of few percent. In the *land02* framework, the *tcal* program is responsible for the determination of this gain for each channel and for providing the results in the input format needed by the analysis code.

In Fig. 4.4 the left plot shows a time-of-flight spectrum using times calibrated with the nominal values of the TDC gain, i.e. 0.05 ns/bin for the TDC used for the S2 and S8 detectors. The right plot shows the same time difference produced using the calibration parameters (gains and offsets) obtained from the time calibrator. After this calibration step is complete, the time of each individual signal is in ns, but the time differences between them do not yet represent a real time-of-flight measurement, due to time synchronisation offsets between the different parts of the same detector (i.e. paddles) or between the different detectors, see Sections 4.2 and 4.3, respectively.

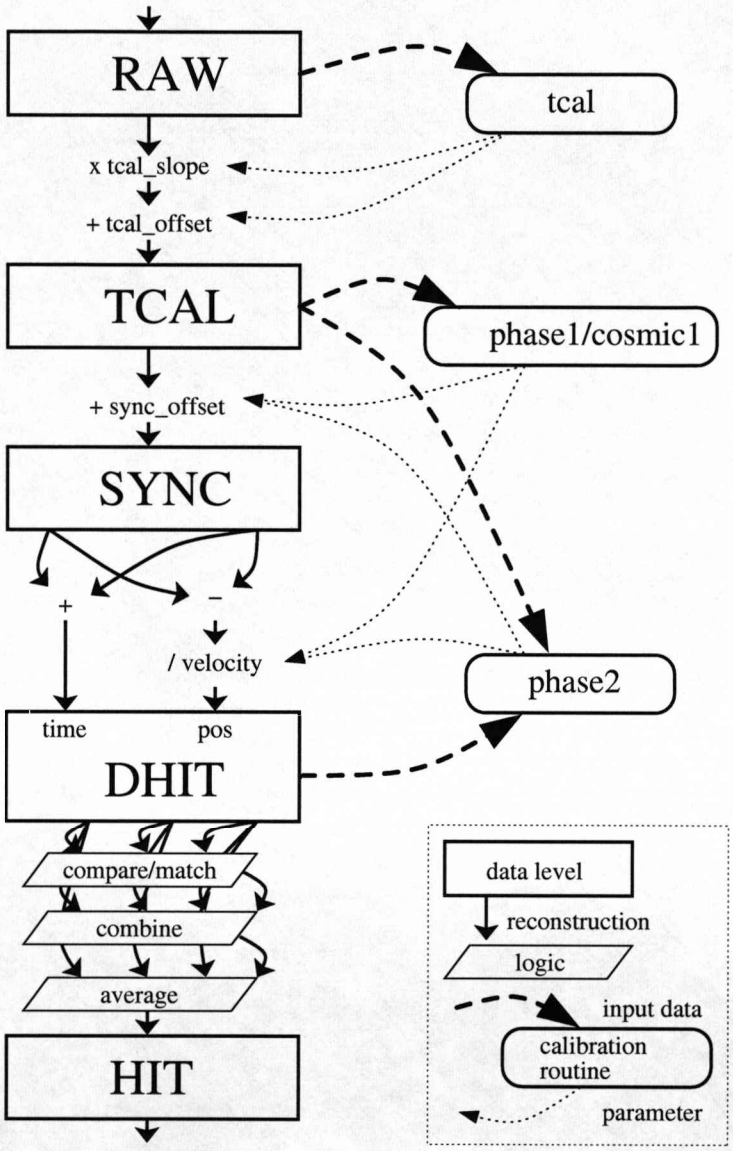

Figure 4.1: The ordering (from top to bottom) of the reconstruction levels (left), the calibration steps (right) and the relations between them (represented by arrows) within the *land02* framework for the case of the TFW detector. The figure is taken from Ref. [58].

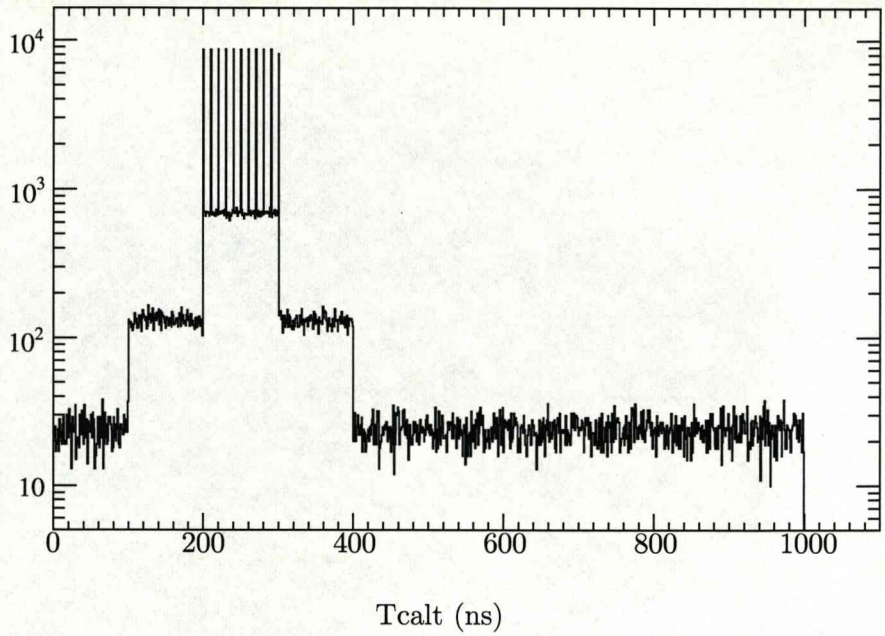

Figure 4.2: Typical time calibrator (*tcalt*) events. Between 200 and 300 ns the 11 pulses used in earlier experiments for time calibration are also evident.

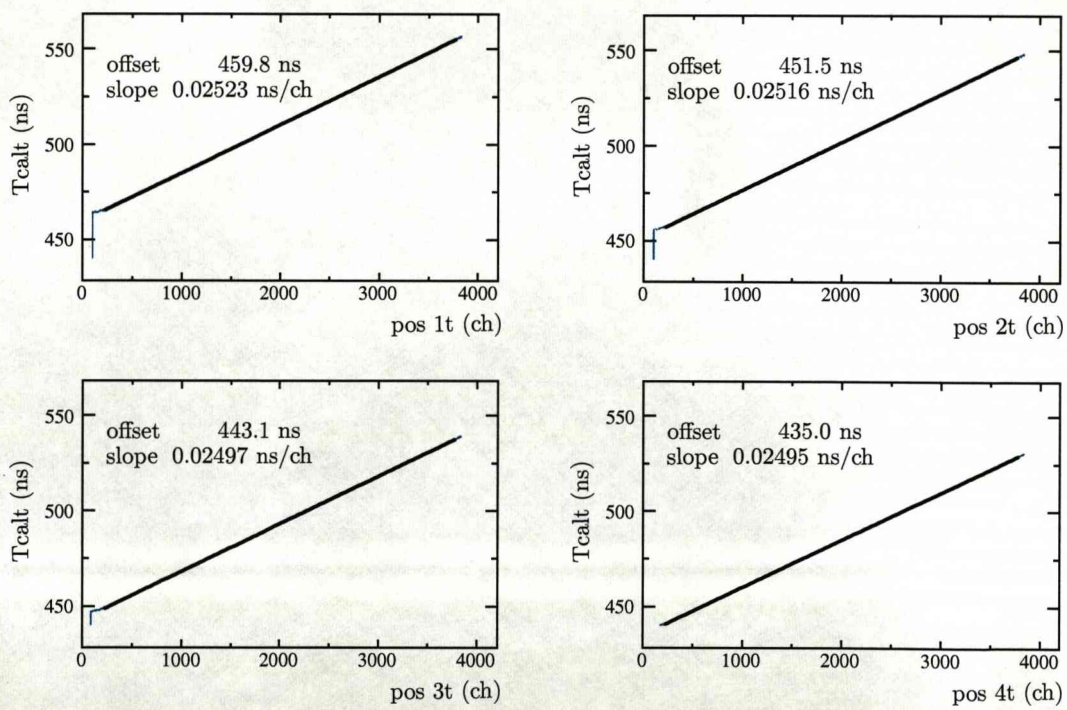

Figure 4.3: Calibration of the TDC channels. Time in ns from the time calibrator clock (Tcalt) is plotted versus channels in the TDC for the 4 POS time signals.

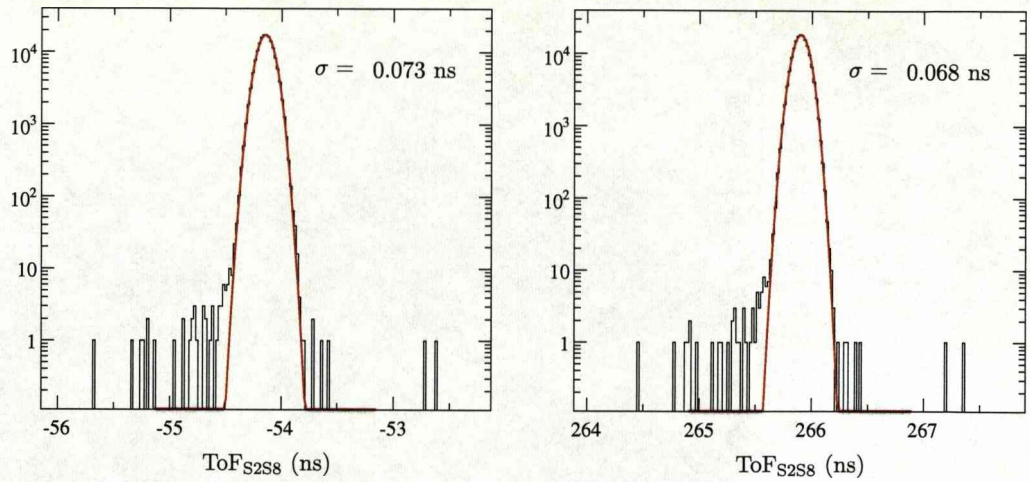

Figure 4.4: Time of flight (ToF) between S2 and S8 detectors using nominal values for the gain of the TDC (left) and parameters obtained from the time calibrator (right). For S2 and S8, where the parameters are found to differ by few percent from the nominal ones, the improvement in resolution (σ) is evident.

4.2 Internal/external calibration of the detectors

The term internal calibration of the detector means that after this stage the detector delivers one time and one energy for each hit (if not multi-hit capable it delivers one time and one energy per event) and also position information according to its internal structure. For example, if it consists of paddles it gives the position in paddle number units. After the external calibration is completed, the detector forgets its internal structure and the position information at this stage is delivered from the detectors in cm with respect to some origin on the detector (e.g. its centre), but still not in lab coordinates.

Although the structure of the detectors may differ quite a lot, they are built and can be treated using the same general principles. Thus, some more general calibration procedures are described first and then their application to the individual detectors is presented.

4.2.1 Calibration of plastic scintillator paddles

Paddles are normally much longer in one direction than they are in the other two (Fig. 4.5). A plastic scintillator paddle is usually read out by a pair of PMs, one at each end of the long side, delivering time and energy signals. In Fig. 4.5 t_0 is the time of the hit and E_0 is the total energy deposited in the detector. The quantities t_1, E_1 and t_2, E_2 are the times and energies that each PM measures with

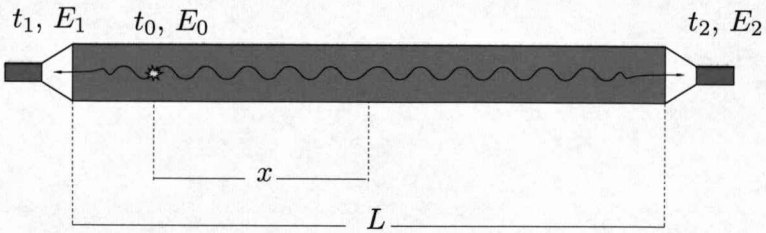

Figure 4.5: The time and energy signals that each PM measures depend not only on the energy and time of each hit but also on the distance of the hit from them. This fact can be used to calculate the position of the hit in the paddle, while when averaging signals from the two PMs this dependency cancels out.

$$t_1 = t_0 + \frac{L/2 - x}{c_{\text{eff}}} + C_1, \tag{4.1}$$

$$t_2 = t_0 + \frac{L/2 + x}{c_{\text{eff}}} + C_2, \tag{4.2}$$

where L is the length of the paddle, c_{eff} is the effective speed of light in the material of the paddle and C_1, C_2 are constant offsets due to cabling and time in the PM tube. The time t_0 of a particle that hits the paddle is obtained by averaging the two time signals (t_1, t_2) from PM_1 and PM_2,

$$t_0 = \frac{t_1 + t_2}{2} - \frac{L/2 - x + L/2 + x}{2c_{\text{eff}}} - \frac{C_1 + C_2}{2} = \frac{t_1 + t_2}{2} - T_{\text{offset}}, \tag{4.3}$$

which is independent of the position of the hit. T_{offset} contains the constants $L/(2c_{\text{eff}})$ and $(C_1 + C_2)/2$ and is obtained by synchronising the detectors, which constitutes the last time-calibration step (see Section 4.3). From Eqs. 4.1 and 4.2 it is evident that the time delivered by each PM depends on the x position of the hit. Thus, x can be written in the following equation as a linear function of the time difference of the two PMs

$$x = c_{\text{eff}} \left(\frac{t_2 - t_1}{2} - \frac{C_2 - C_1}{2} \right). \tag{4.4}$$

For this paddle geometry, it is expected that the energy measured by each PM, E_1 or E_2, has an exponential dependence with the position of the hit, which can be written as

$$E_1 = E_0 C_1^E e^{-\alpha(L/2 - x)}, \tag{4.5}$$

$$E_2 = E_0 C_2^E e^{-\alpha(L/2 + x)}, \tag{4.6}$$

where α, C_1^E, C_2^E are constants. The total energy E_0 deposited in the detector is

$$E_0 = \sqrt{E_1 E_2}\frac{e^{aL/2}}{\sqrt{C_1^E C_2^E}}, \tag{4.7}$$

which is also independent of the position of the hit, like t_0. Using Eqs. 4.5 and 4.6 it is possible to get the position x of the hit as a linear function of the natural logarithm of the ratio of the energy signals measured by the two PMs,

$$x = \frac{1}{2\alpha}\left(\ln\frac{E_1}{E_2} - \ln\frac{C_1^E}{C_2^E}\right). \tag{4.8}$$

In both time and energy signals there are some calibration parameters that need to be determined. For a single paddle these calibration parameters are difficult to obtain. In the case of crossed paddles (Fig. 4.6), however, it is much easier to determine these parameters, since the extra position information of where the two perpendicular paddles meet can be used. Thus, the detectors that have this crossed-paddle structure (TFW, NTF, LAND) can be "self-calibrated" in the sense that throughout the experiment they can provide sets of calibration parameters without the aid of an external device or a specially performed run. In Eq. 4.4 x is known from the crossing of the paddles and t_1, t_2 are measured so that the calibration parameters needed are simply obtained from the linear fit of x versus $(t_1 - t_2)/2$, which in Fig. 4.6 is $(t_L - t_R)/2$ or $(t_U - t_D)/2$. Similar arguments hold for obtaining also the energy calibration parameters.

The detectors with crossed paddles, apart from providing a straight-forward way of determining the calibration parameters, have the additional advantage of allowing for a check of their internal detection resolution, which is very useful for a continuous on-line monitoring of their status. In these detectors the intrinsic time resolution can be found through the difference of the mean time of a horizontal paddle (H) minus the mean time of a vertical paddle (V), as follows

$$t_H - t_V = \frac{t_L + t_R}{2} - \frac{t_U + t_D}{2}. \tag{4.9}$$

Assuming that the resolution (σ_t) of the time measurement from all four PMs is the same, the above difference should have a resolution of

$$\sigma_{t_H - t_V} = \sqrt{4\left(\frac{\sigma_t}{2}\right)^2} = \sigma_t. \tag{4.10}$$

However, the mean time t_0 of a hit in a detector with crossed paddles is

$$t_0 = \frac{t_L + t_R + t_U + t_D}{4}, \tag{4.11}$$

and thus the resolution σ_{t_0} of this measurement can be as good as half the resolution obtained from one PM,

$$\sigma_{t_0} = \sqrt{4\left(\frac{\sigma_t}{4}\right)^2} = \frac{\sigma_t}{2}. \tag{4.12}$$

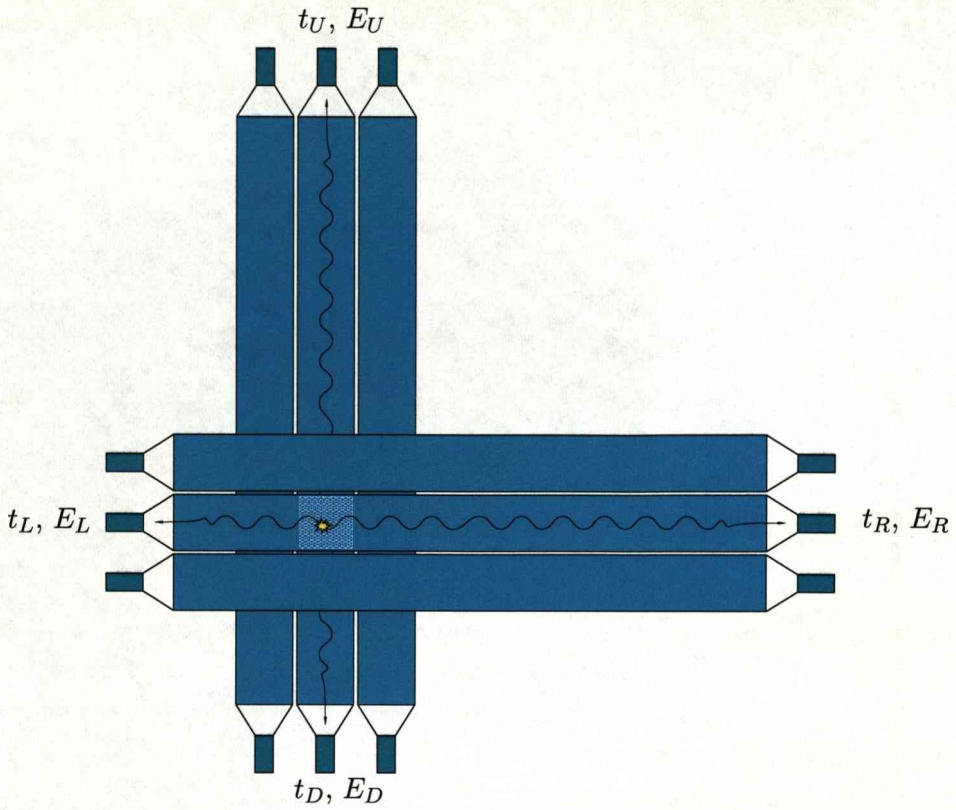

Figure 4.6: When paddles are crossed the rough position of the hit is simply obtained from the (four) PMs that have fired. This information can be used to get the calibration parameters (i.e. "self-calibration").

4.2.2 Find-neighbour algorithm

As mentioned earlier, in the DHIT level the detector has used time and energy information to deliver position information but not in length units yet. This means, for example, that it delivers position information in paddle number units (FGR, TFW, LAND, NTF cases) or a set of (u, v) internal coordinates (GFI, PSP cases). DHIT coordinates (u, v) need to be transformed in the HIT level into the real (x, y) ones for 2D position capable detectors (PSP) or just x if the detector gives information only in one dimension (GFI).

By plotting v versus u variables from GFI or PSP detectors one gets a point for each (u, v) pair as illustrated in Fig. 4.7. It is clear that these points in general form well-defined clusters, while there is a small number of points (noise) in regions between them. To proceed from here, one needs to find the exact (u, v) position of these clusters first and then associate them with the expected x or (x, y) position. An object-oriented algorithm has been developed by the author of this thesis to solve this problem and is briefly described below in two main steps[2].

[2]For position calibrating the GFI detector, a different code based on similar principles was written and used by K. Mahata [68].

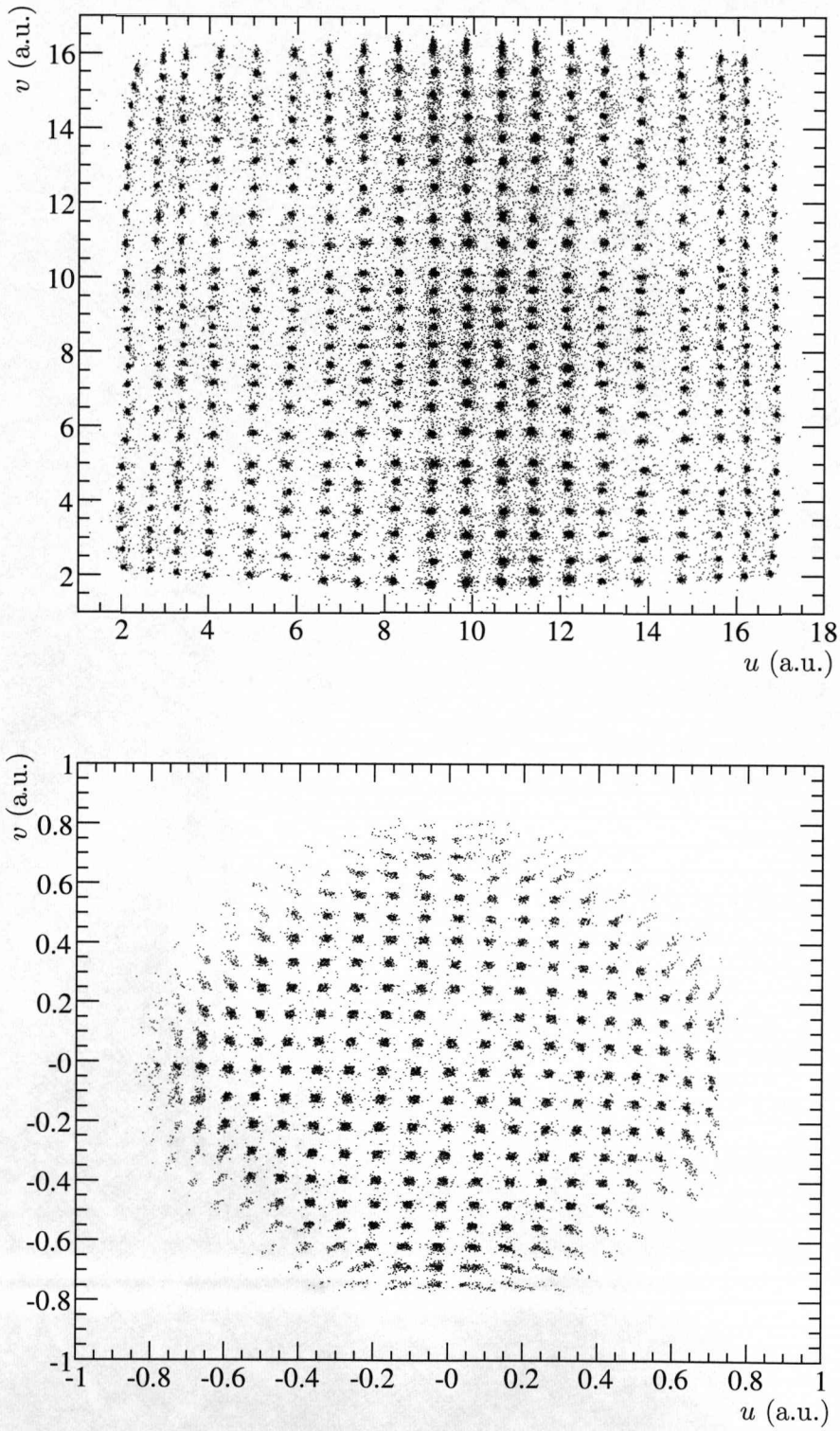

Figure 4.7: The GFI (top) and PSP (bottom) uv plots are shown before position calibration but after gainmatching. In the case of the GFI, clusters are formed where the fibres are coupled to the mask on the photocathode of the PSPM, while for the PSP, clusters are formed as a "shadow" of the beam through the active pixel mask.

Each individual point constitutes a node structure. This structure contains the point's (u, v) coordinates in a 2D vector, parameters describing the density of points (nodes) in the point's neighbourhood and the ID of the cluster that it will get assigned to (if it belongs to any). All nodes are connected to each other with links. A link is a structure that holds pointers to the two nodes that is connecting and a 2D vector which extends from (u_1, v_1) to (u_2, v_2). When all nodes have been searched and compared to their neighbours, they are assigned a signal-over-noise parameter, which is used to decide whether it belongs to a cluster or not. This assignment of point-nodes to clusters constitutes the first step of the algorithm (Fig. 4.8(top)).

Cluster (cluster-node) is another structure which holds pointers to the point-nodes that it contains and has a (u, v) coordinate as the average position of these point-nodes. It also stores pointers to the neighbouring clusters and two indexes (k, l) which are explained below. Clusters are connected to each other with cluster-links.

In both GFI and PSP cases these clusters are expected to sit on an orthogonal grid (k, l) in the xy space as a result of the geometrical construction of the PSPM mask and the active pixel mask for the GFI and the PSP detectors, respectively. However, in the uv space this image is distorted due to non-linearities. It is therefore needed to associate each cluster in the uv space with its expected position on the orthogonal grid in the xy space. In other words, it is needed to index these clusters in two dimensions (k, l), which is the second step of the algorithm. To achieve this, each cluster searches its neighbourhood and finds its north, east, south and west neighbours and makes a link with each of them (Fig. 4.8(bottom)). The search is done within a sector defined by a radius r and an angle $d\theta$. If at the end of this search there are clusters with no neighbours, this sector increases until all clusters have been assigned to their neighbours. In the end all clusters have a well-defined orientation compared to the rest, such that starting from one it is possible to walk through all of them increasing the index k (or l) when walking north (or east) and decreasing this index when walking south (or west). To get the cluster position in x and y from k and l the following equations are used

$$x = n \cdot k, \quad y = n \cdot l, \tag{4.13}$$

where n is the geometrical distance between the clusters, known from the construction of the pixel mask (PSP case) or the PSPM mask (GFI case). At this stage all (u, v) coordinates of the clusters have been determined and their corresponding (k, l) indexes (or (x, y) coordinates) have been found.

A third step is to find a transformation that can send continuously any point of the uv space to the xy one (Fig. 4.9). This transformation is discussed in the detector-specific calibration section for PSP and GFI separately, since different approaches have been used.

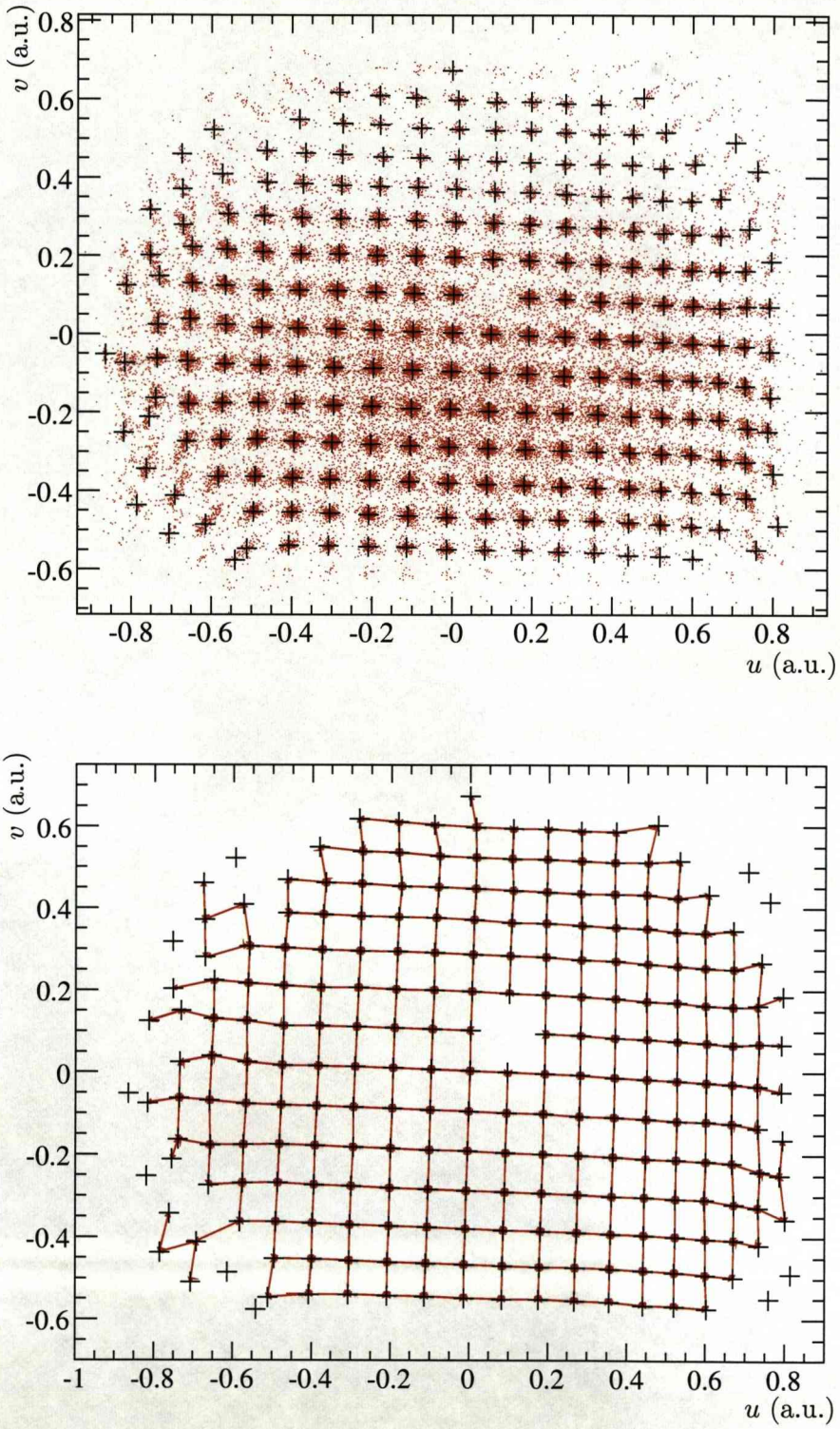

Figure 4.8: In the first step of the algorithm, the mean position of the clusters is found (top). In the second step, each cluster is associated with its neighbouring clusters (bottom). An example case is shown here for the PSP1 detector.

4.2.3 Calibration of the individual detectors

In Sections 4.2.1 and 4.2.2 the general principles behind the calibration and hit reconstruction procedures were presented. In this section the application of these procedures is discussed for each detector individually.

S2 and S8 scintillator detectors

Energy and time signals from the two PM tubes of each S2 or S8 detector are treated as described in the general case of a single scintillator paddle. As mentioned before, individual paddles cannot be "self-calibrated". For the S2 detector in particular the calibration was achieved using the finger detector, which is placed relatively close to S2 (see Fig. 3.2) and can give unambiguous position information. For the S8 detector, which stands alone at F8, the effective speed of light found for the S2 detector is used, since they consist of the same material and have very similar geometries.

FGR finger scintillator detector

Although the FGR detector consists of 15 vertical paddles, it is not considered a direct case of the general calibration of plastic scintillator paddles described earlier, due to the specific way that the paddles are read out (Section 3.4.1); however, the principles for the hit reconstruction are similar. To calibrate this detector and synchronise the 16 PM tubes, it is assumed that the beam is always passing from the same horizontal plane (i.e. same y position), which is a reasonable assumption for the dispersive focal plane where this detector is placed. This means that the time difference between the top and the bottom PM is always the same due to Eq. 4.4, and similarly due to Eq. 4.8 the difference of the natural logarithm of energies is also constant. Since each PM (apart from the very first and the very last) is also reading out one of their neighbouring paddles (see Fig. 3.4), all PMs can be synchronised with each other.

POS scintillator detector

Although the shape of the POS scintillator is far from being a paddle (it is a square), some of the ideas applied for the crossed paddles can be applied for its hit reconstruction. The time differences of the two horizontal (or vertical) PMs give the position of the hit, while the mean time is independent of its position. The time resolution of this detector can be also monitored in the same way as for the crossed paddles.

PSP Si detector

As mentioned in Sections 3.4.2 and 3.4.3, PSPs are used in this experiment for measuring both the charge of the incident ion, through the energy loss in the detector, and the position where the incident ion passes. The position is reconstructed from the four

anode signals (Q_1, Q_2, Q_3, Q_4), see Fig. 3.6. The formulae which are used for the position reconstruction are

$$u = \frac{Q_2 + Q_3 - Q_4 - Q_1}{Q_1 + Q_2 + Q_3 + Q_4}, \tag{4.14}$$

$$v = \frac{Q_1 + Q_2 - Q_3 - Q_4}{Q_1 + Q_2 + Q_3 + Q_4}. \tag{4.15}$$

Before using the anodes for position reconstruction one needs to subtract the ADC (Analog-to-Digital Converter) offset and then gainmatch them. The energy signal of each anode is position dependent and therefore has a very broad distribution. Thus, the gainmatching is performed with the pixel calibration run by gating on the central pixel of the mask. Signals from all four contacts are multiplied by a gain factor such that all of them give the same energy, as expected since the central pixel has the same distance from all corners of the square.

The reconstructed position using Eqs. 4.14 and 4.15 often suffers from severe non-linear distortions. In other words the reconstructed position is a non-linear transformation of the real position. To overcome this problem one needs to perform position calibration of the detector, i.e. to find those functions that will transform the measured (u, v) positions into the real (x, y) ones. Each real coordinate of a hit is a function of both measured coordinates (u, v).

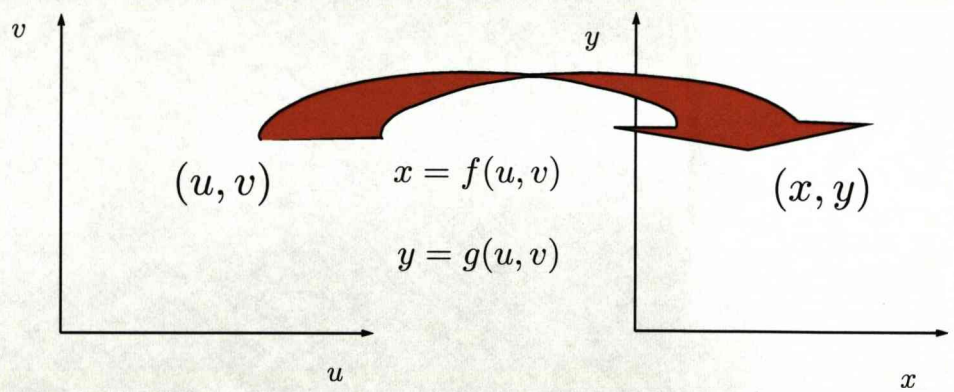

Figure 4.9: A transformation that associates the measured uv space to the real xy one.

The position calibration is achieved by using an active pixel reference mask (PIX) deposited in front of each PSP detector. By requiring events that trigger the active pixel mask, one can "see" its pixels in the PSP reconstructed image, see Fig. 4.7(bottom). At this point the technique described in Section 4.2.2 is used to find the (u, v) coordinates of the pixels and associate them with each other. It is now needed to find the transformation that sends any point of the uv space to the xy space (Fig. 4.9). In the case of the PSPs two methods are used to transform the measured (u, v) coordinates into the real (x, y) ones:

- a 2D polynomial fit between the expected values and the measured ones ($x = f(u,v)$, $y = g(u,v)$) and
- the quad-mesh method, described later in this section.

Since each pixel position has been associated to a (k, l) pair and thus to a (x, y) real position, it is possible to draw two 2D graphs with sets of (u, v, x) or (u, v, y) points. The fit of a 2D function to these data-points provides a continuous transformation that can be used to calculate from any measured (u, v) point its corresponding real (x, y) one. Two 3^{rd}, 4^{th} or 5^{th} order 2D polynomials, depending on the distortion, are used to fit the data. By performing a χ^2 minimisation on all pixel positions, the parameters of these functions are determined, as illustrated in Fig. 4.10.

The 3^{rd} order 2D polynomial fit gives in general a satisfactory (x, y) reconstruction, given that the detectors are behaving reasonably well. In the present experiment, however, larger distortions gradually develop which require in the analysis an increase in the order of the polynomial, e.g. to 5^{th} order 2D polynomial. Such a high order polynomial behaves "unpredictably" in regions where not many points exist and furthermore the large number of parameters (e.g. 21 parameters for a 5^{th} order 2D polynomial) makes it difficult to monitor (or "guess") any changes during the experiment.

All three PSP detectors in the beginning of the present experiment have a fairly good (not very distorted) behaviour. Unfortunately, in the next calibration run, performed towards the end of the experiment, this situation changes dramatically especially for the PSP2 detector. Furthermore, the small number of pixel-calibration runs do not allow for a safe monitoring of this deformation throughout the experiment. Although an increase in the order of the polynomial will eventually fit the data, it induces big ambiguities for files away from the calibration runs. Even if one guesses how this degeneration is changing with time, it is not trivial to vary parameters of high order polynomials such that they follow this degeneration from run to run.

For the aforementioned reason and due to the similarity that the PSP and GFI uv plots have, a different approach has been used (quad-mesh method). The (u, v) coordinates of the reconstructed pixels constitute the vertices of a grid of quadrilateral elements. These vertices can be one to one associated with the vertices of an orthogonal square grid in the xy space, which are the actual positions obtained from the geometrical arrangement of the pixels in the pixel mask. Any point within each of these quadrilateral elements is first assigned to the corresponding (x, y) square and then linearly interpolated depending on its distances from the corners of the particular quadrilateral element. The obvious advantage of this approach over the correction using the polynomial functions is that it can approximate more complicated deformations of the uv space due to its higher degrees of freedom. Furthermore, in this approach any time-dependent deformation of the uv plot, from one calibration run to the next, can

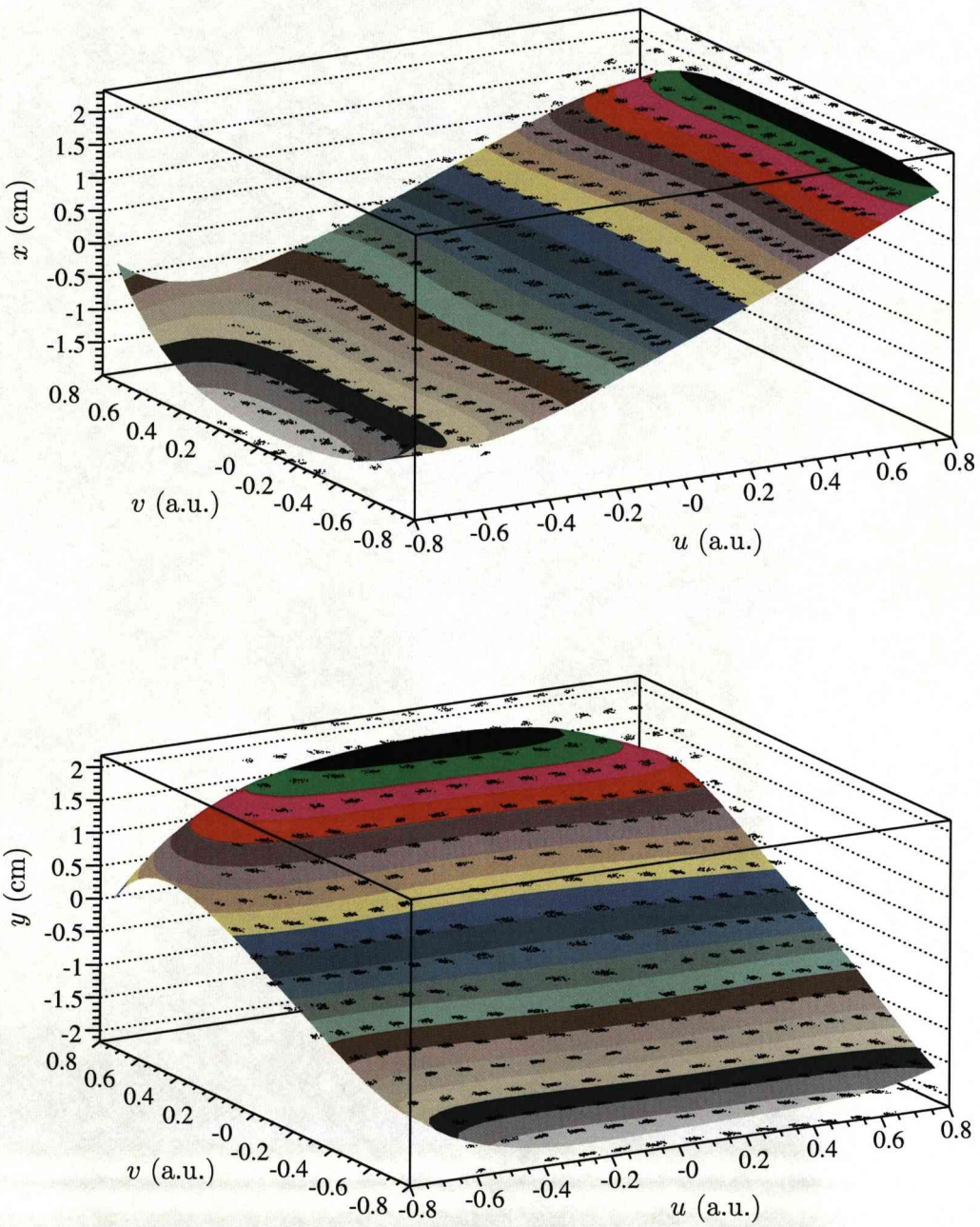

Figure 4.10: Fitting the expected values $x(u, v)$ (top) and $y(u, v)$ (bottom) using a 5^{th} order 2D polynomial for the PSP2 detector.

be better understood and monitored as a drift of the vertices of individual quadrilateral elements (see time-dependent calibration in Section 4.4).

In Fig. 4.11 reconstructed pixels in the PSP2 detector are shown before and after position calibration using the quad-mesh method for the most distorted case found in the present experiment. It is evident that position calibration is achieved for the full illuminated area with an accuracy and precision much better than the width of a pixel (0.5×0.5 mm^2). Accuracy here is used to describe how close the reconstructed pixels are to the geometrical position known from the construction of the pixel mask, while precision describes the resolution with which these pixel positions are known, or in other words the width of the reconstructed pixel.

In order to illustrate the resolution obtained for the PSP detectors, a different cut in the energy signal of the active pixel mask can be applied, so that only ions which have scattered in the edges of the pixel, and thus left less energy in the mask, are taken into account (see Fig. 4.12(top)). If this is done, then it is possible to see the edges of the pixel in the reconstructed image from the PSP detector, as shown in Fig. 4.12(bottom). Furthermore, by plotting the energy deposited in the active pixel mask versus the position obtained from the PSP detector it is evident that ions which have passed through the centre of a pixel deposit larger energies, while towards the edge of the pixel the energy measured by the pixel mask drops rapidly (Fig. 4.13(top)). The bottom plot of Fig. 4.13 is a "zoom" of the plot at the top. The red vertical lines indicate the expected position of the edges of a pixel. One can claim that since these edges are easily distinguished in the PSP reconstructed position, the σ resolution is of the order of 100 μm.

GFI detector

As mentioned in Section 3.5.2, GFI fibres are coupled to the photocathode of a PSPM tube with the use of a mask, which has holes arranged in a well-known geometry. A hit in the detector produces light which is guided through the fibres and causes a well-defined light spot on the photocathode. An electrical signal is then developed in some of the 18×16 anode wires, depending on the 2D position of the light spot on the photocathode. By combining information from these signals, it is possible to precisely reconstruct the position of the light spot on the photocathode and thus identify the fibre that is hit.

However, the amplitude of the signals depends on their amplification, which is in general different for each one, and also depends on their position on the photocathode of the PSPM. Thus, it is essential to properly gainmatch all the anode wires before proceeding with the position reconstruction of the hit. It is in general expected that the charge distribution of a typical hit will produce electrical signals in about seven neighbouring wires in each (u, v) direction and that their amplitudes will exhibit a

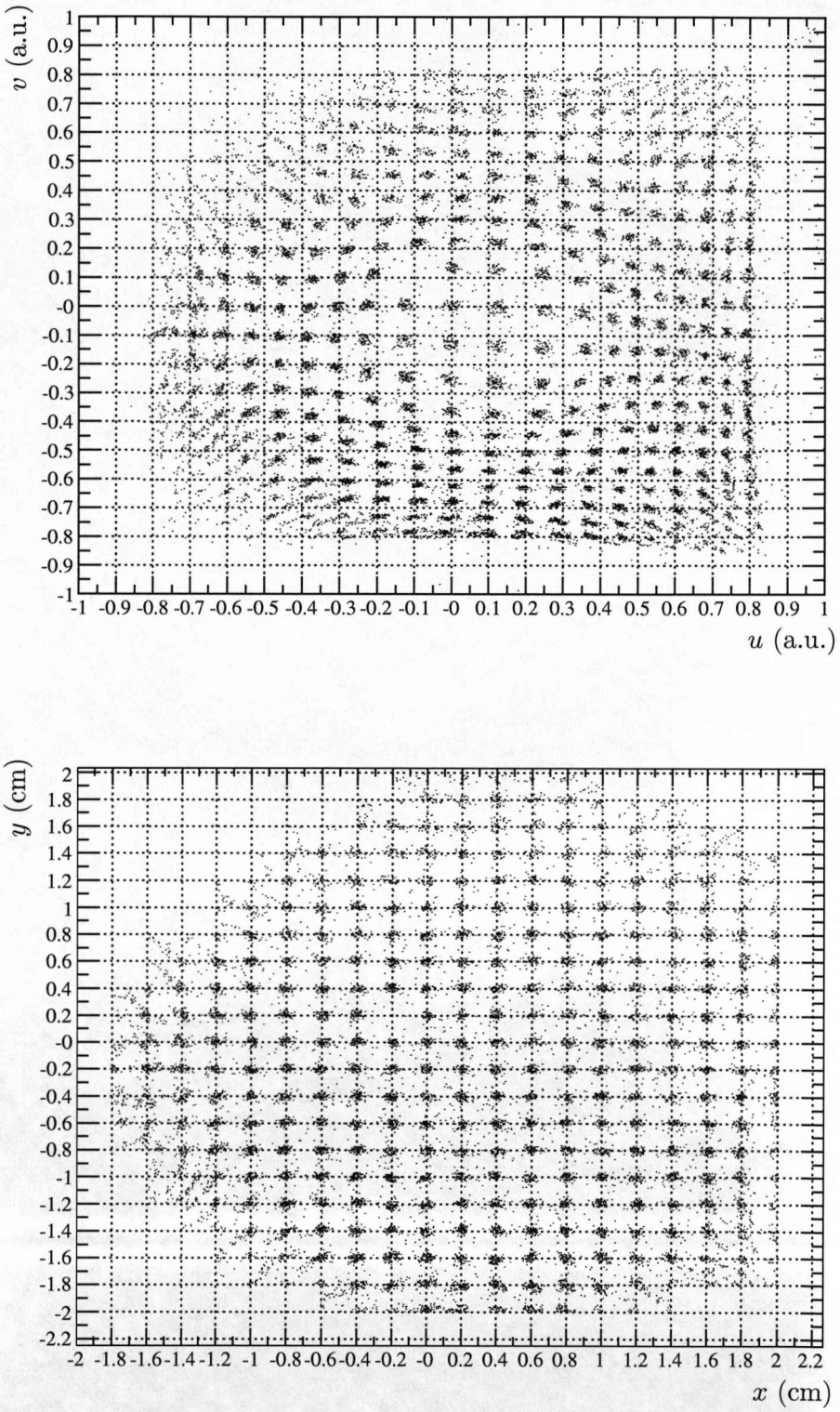

Figure 4.11: Position reconstruction from raw data (top) and after position calibration (bottom) using the quad-mesh method for the most distorted case found in this experiment (i.e. for the PSP2 detector).

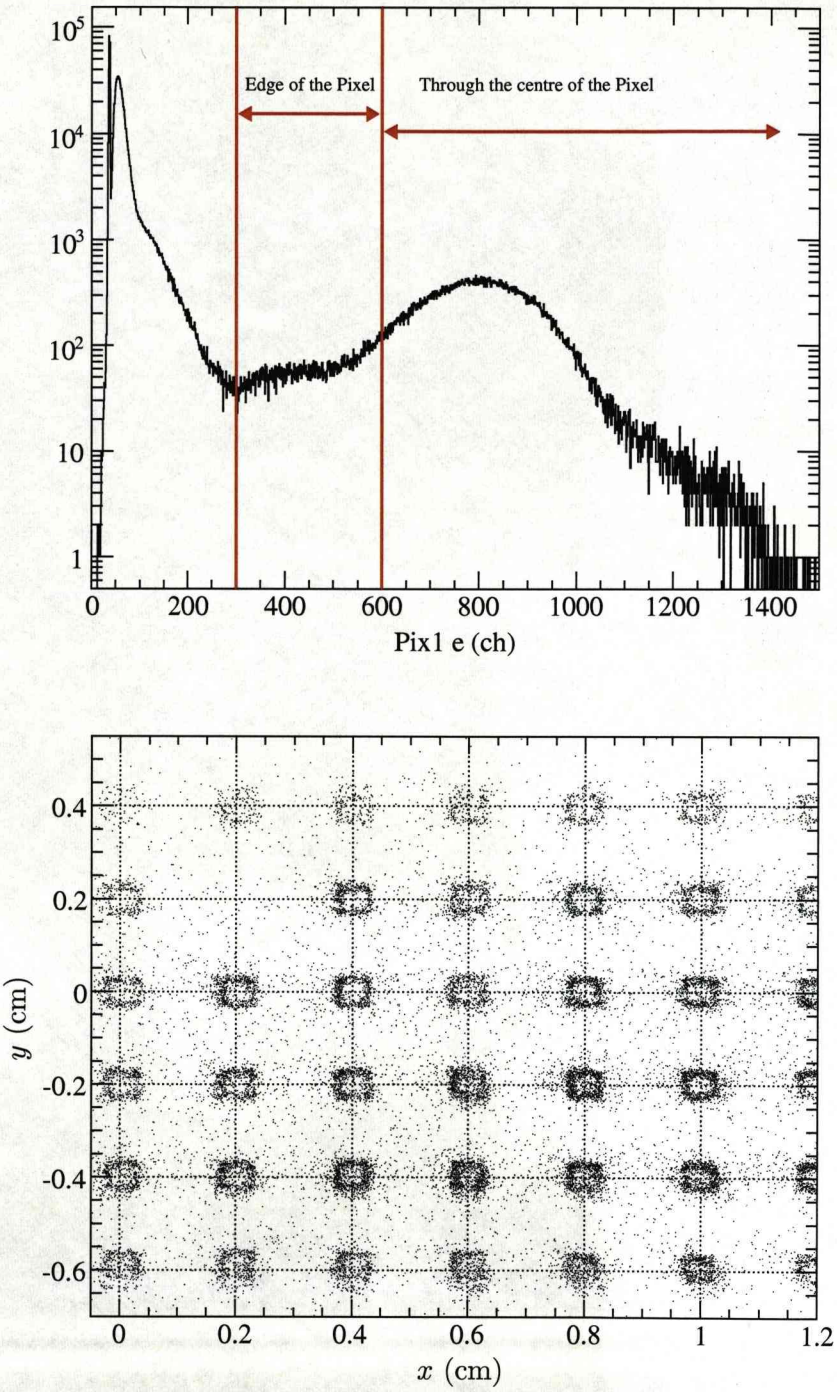

Figure 4.12: The raw energy signal (top) of the active pixel mask during a pixel-calibration run. Events with energy larger than 600 - 700 ch (channels) are selected in order to obtain a clean image of the reconstructed pixels in the PSP detector (see Fig. 4.11). However, with a different energy cut one can select events for which the ions have scattered at the edge of the pixel and thus left less energy. The reconstructed position (bottom) in the PSP detector for such events shows indeed the edges of the pixels, shown here for the PSP1 detector.

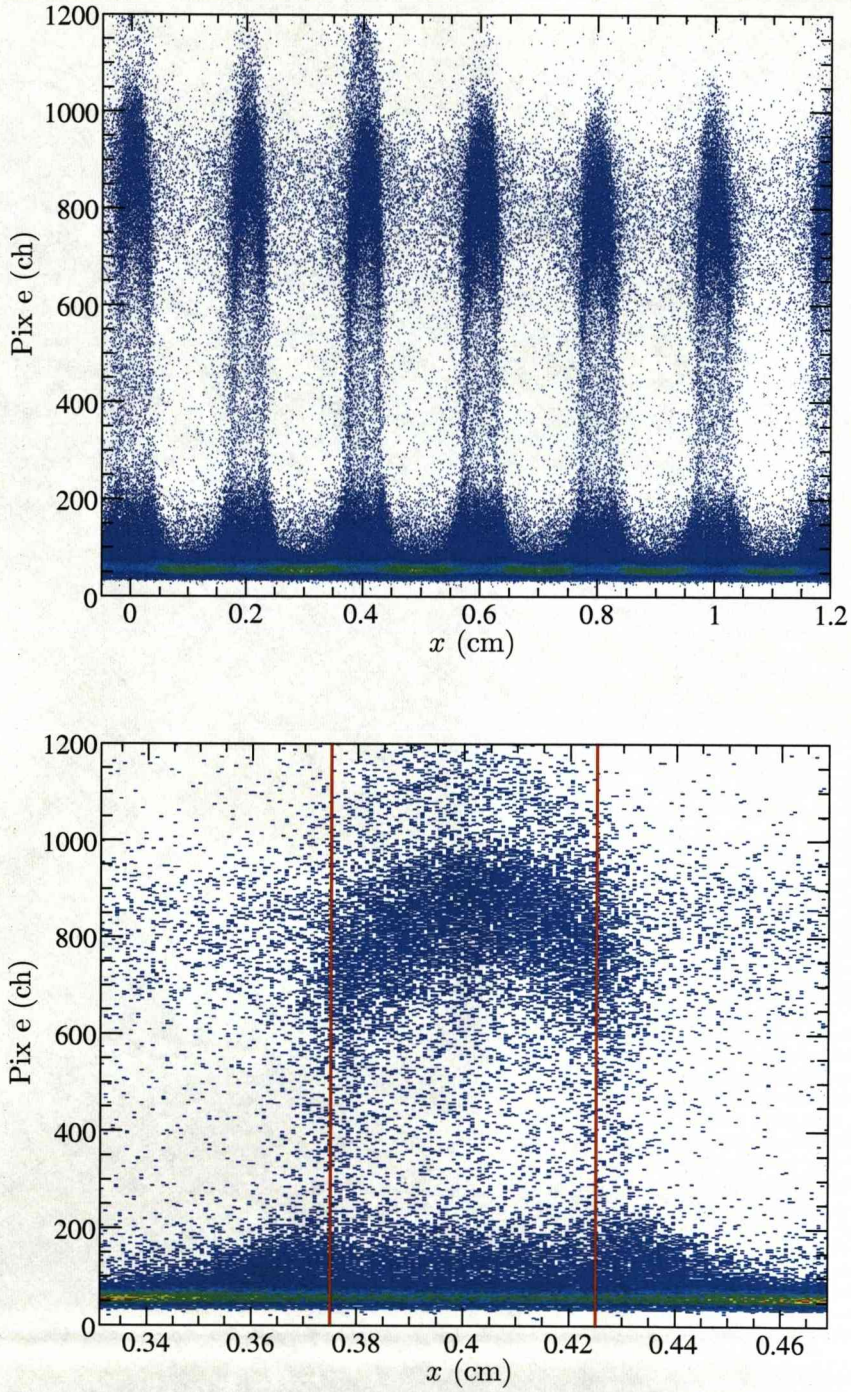

Figure 4.13: The energy measured by the active pixel mask versus the x position in the PSP detector. Ions that pass through the centre of a pixel generate a large energy signal in the pixel mask, while those that scatter at the edges of the pixel deposit less energy. Due to the fine position resolution of the PSP detector, which is much better than the size of a pixel, it is possible to clearly distinguish this effect at the edges of the pixel (illustrated in this figure for the PSP1 detector).

Gaussian-like shape. This expected Gaussian-like shape of the distribution can be used to gainmatch the wires, requiring all signals from neighbouring wires to fit in this distribution. The gains for each wire are then found by solving simultaneously the equations for all wires [68]. It is important to perform the gainmatching using a special run called the sweep run. During a sweep run the field of the ALADIN magnet is varying in such a way that the beam is forced to cover the whole range of the detector homogeneously.

Once the gainmatching is performed, the mean position of the charge distribution for each hit gives the u and v coordinates of the light spot. For a typical sweep run all the light spots, which correspond to fibres, are reconstructed properly. Fig. 4.14 shows reconstructed fibres in the uv space before (top) and after (bottom) gainmatching. It is clear that the gainmatching has corrected the large distortions at the edge of the photocathode and dots have in general a better-defined shape. This reflects the final position resolution of the detector.

At this stage a method similar to the one described in Section 4.2.2 is used to find the (u, v) position of each dot (cluster), associate them, index them and assign them the corresponding fibre. After the position (u, v) of each fibre on the mask has been found and indexed (k, l), as in the case of the PSP, a transformation is needed to send any point of the uv space to the corresponding x position. In the case of the GFI, however, the reconstruction of the x position of the hit is not a continuous transformation of the uv space, since each point has to be related to a discrete fibre. If for a hit in the detector the point (u, v) on the mask is within the width of a cluster, the assignment is trivial, but for points lying between the clusters there are more than one candidate fibres. To reconstruct the x position, either a decision has to be made choosing the fibre closest to the hit or even better it can be calculated as a weighted average of the candidate fibres [68] as follows

$$x = \frac{\sum w_{kl} x_{kl}}{\sum w_{kl}}, \tag{4.16}$$

where w_{kl} is the probability of the hit to belong to the kl fibre. This probability depends on the distance of the hit from the kl cluster and on the widths σ_{ukl}, σ_{vkl} of this cluster.

TFW detector

The calibration and hit reconstruction of the TFW detector is a typical case of the general crossed-paddle procedure described earlier.

LAND detector

For the LAND detector the same crossed-paddle procedure is used for calibration. Although LAND, in general, is not directly hit by the beam, it has the advantage of the detection of cosmic radiation with high efficiency due to its big volume and relatively

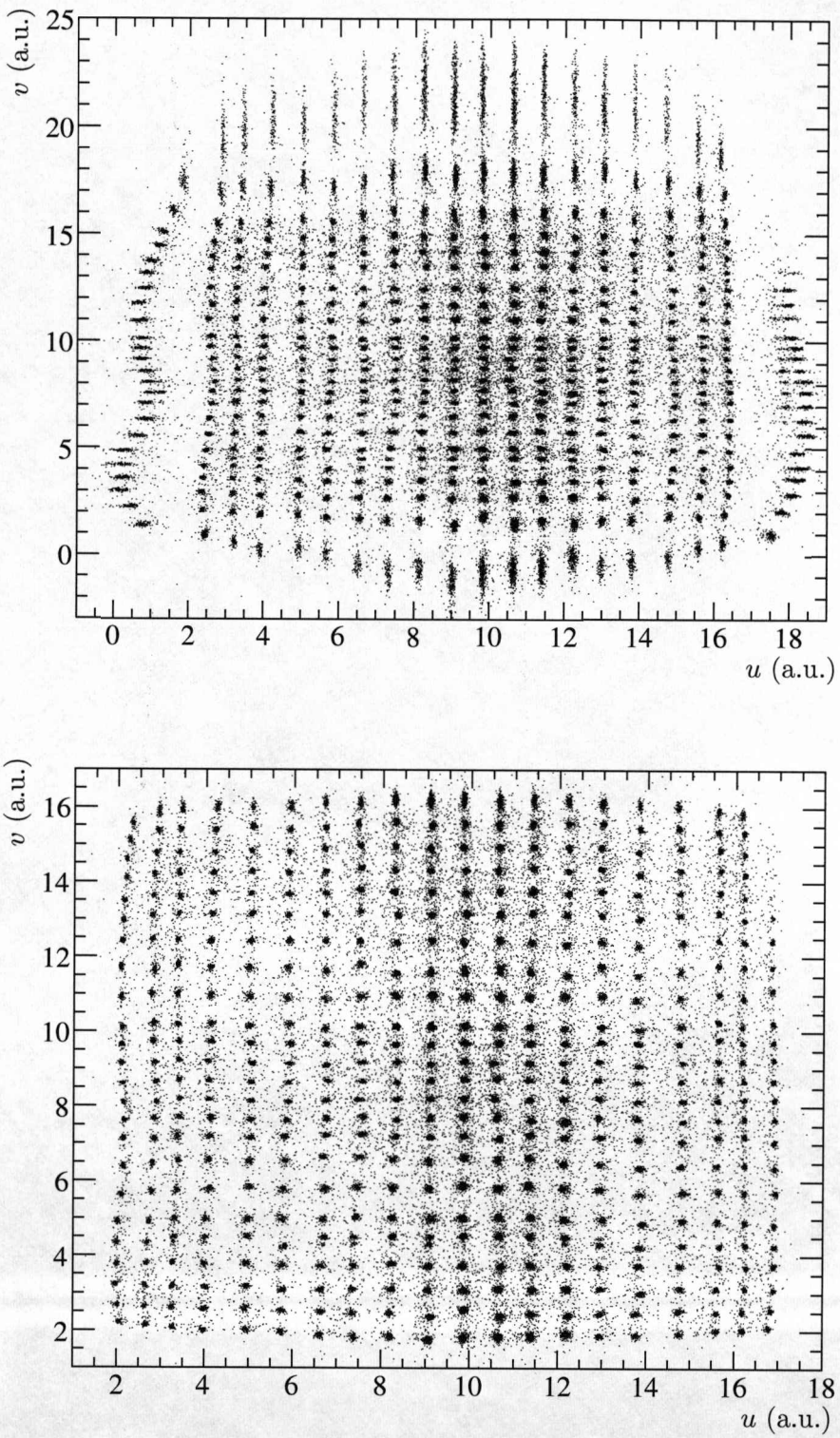

Figure 4.14: The *uv* plot of the GFI detector before (top) and after (bottom) gain-matching.

high density. Cosmic radiation is expected to travel through LAND in a straight line and deposit almost the same energy in each paddle. This enables a calibration with cosmic radiation, which uniformly penetrates the whole detector throughout the experiment, allowing for the determination and constant monitoring of the calibration parameters. Within the *land02* framework this calibration is performed using the *cosmic* calibration program.

4.3 Synchronisation and alignment of the detectors

Two additional important calibration steps are required before one can extract useful physical quantities from the data, to synchronise and align the detectors: "synchronise" in the sense of finding time offsets between the detectors, while at the same time obtaining the length of the path for a reference particle flying from one detector to the next. This length is not necessarily their geometrical distance, especially when magnets are in between. This procedure is also known as velocity calibration and is described in the following section. Alignment is needed since the position that one detector measures is known with respect to some point in this detector, e.g. its centre, but is not precisely known in the laboratory system. Only after these steps are completed does a combination of the information from the different detectors give meaningful results.

4.3.1 Velocity calibration

The velocity (β) of the ions is calculated through time-of-flight (ToF) measurements and known paths (S) as follows

$$\beta = \frac{S}{(\mathrm{ToF}) \cdot c}, \tag{4.17}$$

where c is the speed of light. To get, however, time-of-flight measurements from the time measured by the detectors, the time signals need to be synchronised with each other first. Combined time signals from the individual detectors get a physical meaning only when appropriate offsets due to electronics and cables have been applied. The paths and offsets (T_{offset}) are determined using the following method. The measured time difference (δt) is

$$\delta t = \mathrm{ToF} + T_{\mathrm{offset}}. \tag{4.18}$$

Combining Eqs. 4.17 and 4.18 the following equations are derived

$$\beta = \frac{S}{(\delta t - T_{\mathrm{offset}})c},$$

$$\beta \delta t - \beta T_{\mathrm{offset}} = \frac{S}{c},$$

$$\beta\delta t = \frac{S}{c} + \beta T_{\text{offset}}. \tag{4.19}$$

From Eq. 4.19 it is clear that by plotting $\beta\delta t$ versus β for different known beam velocities and performing a linear fit, the flight path is obtained from the offset of the linear fit (times the speed of light) and the time offset (due to cabling, etc.) is obtained from the slope of the linear fit, as illustrated in Fig. 4.15.

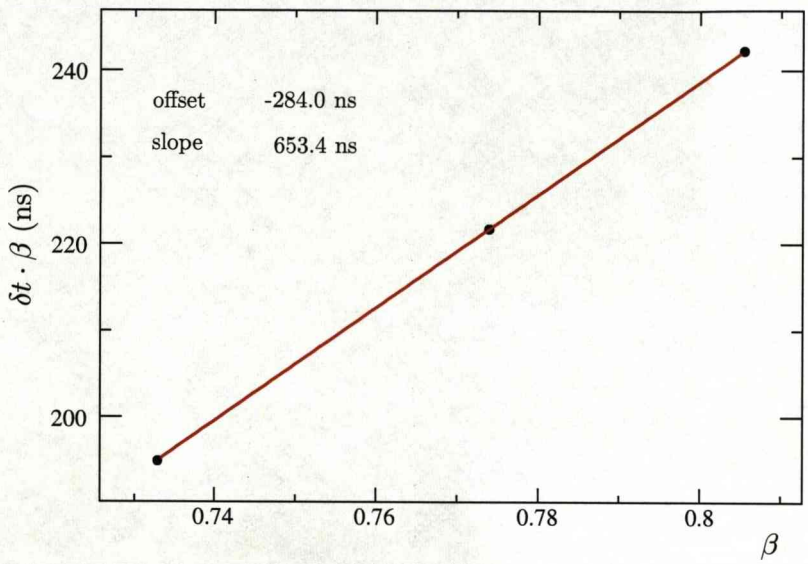

Figure 4.15: Linear fit of $\beta\delta t$ versus β for the three different calibration runs with well-known beam velocities. The offset of the fit is related to the flight path between the detectors and the slope to the time offsets due to cabling and electronics. Errors are much smaller than the size of the points in the plot.

The velocity calibration is usually performed using runs with primary beam at different beam energies (i.e. velocities). In this experiment a ^{58}Ni beam with three different energies around 450, 550 and 650 MeV/nucleon (and well-known corresponding magnetic rigidities $B\rho$) has been used. The velocity β can then be precisely determined from the $B\rho$ value given by the FRS setting.

The offset of the linear fit, which gives the flight path, needs to be inserted as an experiment-specific geometrical parameter and thus it is "not allowed" to be adjusted during the experiment. In Fig. 4.15, for example, the flight path (offset·c) is found to be $\sim$ 85 m. In contrast, the synchronisation offset that is found (i.e. slope of the linear fit) should be provided as a calibration parameter in the *land02* framework. This offset is applied for the whole detector (e.g. all channels). It is assumed that the detector is already internally synchronised, but for the scintillators with only two PM tubes each this is trivial. The POS detector, however, requires synchronisation of pairs of PM tubes corresponding to horizontal and vertical pairs.

4.3.2 Position and angle on target

The tracking of the projectile on target, i.e. finding the position and the angle on target, requires at least two 2D position measurements before and close to the target, which are provided by the PSP1 and PSP2 detectors. The position and the angle on target is found simply by extrapolating the line defined by each pair of points (one in PSP1 and one in PSP2) to the target position.

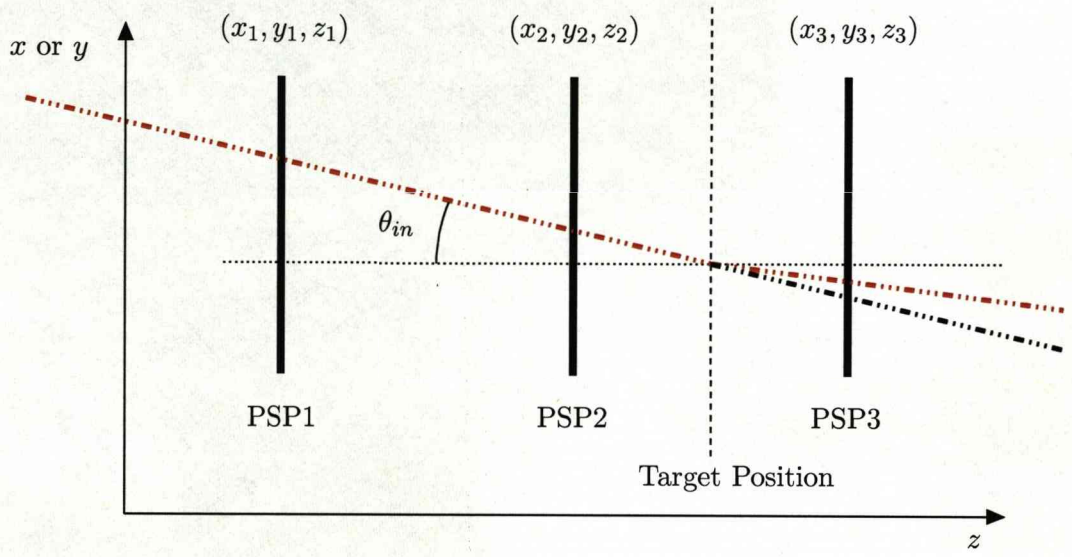

Figure 4.16: Two PSP detectors before the target and one after the target serve for determining the incoming and outgoing angles, as well as the position on target.

If an ion is moving along a straight line (Fig. 4.16) and hits the PSP1 and PSP2 detectors at points $\vec{r}_1(x_1, y_1, z_1)$ and $\vec{r}_2(x_2, y_2, z_2)$, respectively, its coordinates $\vec{r}(x, y, z)$ should satisfy the following equation

$$\vec{r} = \vec{r}_1 + (\vec{r}_2 - \vec{r}_1)t \quad \text{where t} \in I\!R, \tag{4.20}$$

or the symmetric equation of line

$$\frac{x - x_1}{x_2 - x_1} = \frac{y - y_1}{y_2 - y_1} = \frac{z - z_1}{z_2 - z_1}, \tag{4.21}$$

which shows that if any of the x, y, z is known, the other two can be calculated. By considering that the target position (z_0) is known, it is trivial to calculate the extrapolated (x_0, y_0) coordinates

$$x_0 = \frac{x_2(z_0 - z_1) - x_1(z_0 - z_2)}{z_2 - z_1}, \quad y_0 = \frac{y_2(z_0 - z_1) - y_1(z_0 - z_2)}{z_2 - z_1}. \tag{4.22}$$

Equivalently, as in the case of the target position, the (x, y) position measurements from the PSP1 and PSP2 detectors can be extrapolated at the PSP3 position (z_3). If the three PSPs are perfectly aligned the difference between the extrapolated position at PSP3 (x_3', y_3') and the position measured by PSP3 itself (x_3, y_3), for unreacted beam particles, should peak around zero, otherwise the mean position of the peak indicates the geometrical offset of the third PSP relative to the other two.

The position measurement from PSP1 and PSP2 detectors define the incoming angle, while the extrapolated position on target and the PSP3 position measurement define the outgoing angle. Their difference is proportional to the transverse momentum transferred in the reaction. For unreacted beam the difference of the outgoing and incoming angles should be a distribution with a width defined by the intrinsic position resolution of the detectors and by the multiple Coulomb scattering (straggling) in the materials. The contribution of each of these two factors, i.e. position resolution of the detectors and straggling in the materials, to the overall angular resolution is discussed below. For simplicity, instead of the scattering angle in space, the equations are written for the projected incoming (θ_{in}) and outgoing (θ_{out}) angles on the xz plane. In addition, since the angles are quite small the assumption $\tan\theta \approx \theta$ holds. If the materials were thin enough to have a negligible straggling, only the precision (σ) of the position measurements would define the overall angular resolution (so that $\theta_{in} = \theta_{in}^0$ and $\theta_{out} = \theta_{out}^0$) through error propagation in the following formulae

$$\theta_{in} = \theta_{in}^0 = \frac{x_2 - x_1}{z_2 - z_1}, \tag{4.23}$$

$$\theta_{out} = \theta_{out}^0 = \frac{x_3 - x_0}{z_3 - z_0}. \tag{4.24}$$

In reality, however, the incoming angle at the target position (θ_{in}) is affected by the straggling in the PSP2 material $\theta_{str}^{\mathrm{PSP2}}$,

$$\theta_{in} = \theta_{in}^0 + \theta_{str}^{\mathrm{PSP2}}. \tag{4.25}$$

The outgoing angle is affected by the angular straggling caused by the material of the target $\theta_{str}^{\mathrm{Target}}$, if present,

$$\theta_{out} = \theta_{out}^0 + \theta_{str}^{\mathrm{Target}}, \tag{4.26}$$

where θ_{str} is a Gaussian distribution, centred at zero with a standard deviation σ_{str}. The outgoing angle has an additional error contribution from the extrapolated x_0 position, which is affected by the $\theta_{str}^{\mathrm{PSP2}}$. This is more clear if one rewrites x_0 as

$$x_0 = x_2 + \theta_{in}\,(z_0 - z_2)\,, \tag{4.27}$$

and by substituting the above formula in Eqs. 4.24 and 4.26 then

$$\theta_{out} = \frac{x_3 - (x_2 + \theta_{in}(z_0 - z_2))}{z_3 - z_0} + \theta_{str}^{\text{Target}}. \tag{4.28}$$

The difference between the outgoing and the incoming angles is

$$\delta\theta = \frac{x_3 - (x_2 + \theta_{in}(z_0 - z_2))}{z_3 - z_0} + \theta_{str}^{\text{Target}} - \theta_{in}, \tag{4.29}$$

or

$$\delta\theta = \frac{x_3 - x_2}{z_3 - z_0} + \theta_{str}^{\text{Target}} + \left(\frac{-(z_0 - z_2)}{z_3 - z_0} - 1\right)\theta_{in}. \tag{4.30}$$

Using Eqs. 4.23, 4.25, 4.30 and $z_0 = 0$, $\delta\theta$ can be rewritten as follows

$$\delta\theta = \frac{x_3(z_2 - z_1) + x_1(z_3 - z_2) - x_2(z_3 - z_1)}{z_3(z_2 - z_1)} + \left(\frac{z_2}{z_3} - 1\right)\theta_{str}^{\text{PSP2}} + \theta_{str}^{\text{Target}}. \tag{4.31}$$

The error in this measurement, assuming $\sigma_{x_1} = \sigma_{x_2} = \sigma_{x_3} = \sigma$, is

$$\sigma_{\delta\theta}^2 = \sigma^2\left(\frac{1}{z_3^2} + \frac{(z_3 - z_2)^2}{z_3^2(z_2 - z_1)^2} + \frac{(z_3 - z_1)^2}{z_3^2(z_2 - z_1)^2}\right) + \left(\left(\frac{z_2}{z_3} - 1\right)\sigma_{\theta_{str}^{\text{PSP2}}}\right)^2 + \left(\sigma_{\theta_{str}^{\text{Target}}}\right)^2, \tag{4.32}$$

which for $z_3 \approx -z_2 \approx (z_2 - z_1)/2 \approx 0.75$ m becomes

$$\sigma_{\delta\theta}^2 = 6 \cdot \left(\frac{\sigma}{0.75}\right)^2 + \left(2 \cdot \sigma_{\theta_{str}^{\text{PSP2}}}\right)^2 + \left(\sigma_{\theta_{str}^{\text{Target}}}\right)^2. \tag{4.33}$$

Eq. 4.33 relates in a rather simple formula the actual angular resolution with the position resolution of the detectors and the straggling in the materials.

4.4 Time-dependent calibration

In the previous sections the procedures for obtaining the calibration parameters were described. However, these calibration parameters are often varying throughout an experiment for various reasons. This requires additional time-dependent monitoring and corrections of these parameters, which are presented in this section. Reasons causing the calibration parameters to drift could be damage of the detector, "jumps" in time channels and noise in the energy channels in the electronic chain, temperature effects in the cables, change of HV gains or other intended adjustments. It is clear that these types of correction depend on the specific equipment and are usually very specific for each experiment. However, the need and the general procedure of monitoring such effects is common for all experiments.

In previous sections some detectors have been characterised as "self-calibrated" (see Section 4.2.1). These detectors have the advantage of providing within the *land02* framework time-dependent calibration parameters with no additional equipment or

specially performed run. For all other detectors, however, additional care is required, as discussed in this section. In particular, the PM signals of the beam detectors S2 and S8 may drift and/or "jump" throughout the experiment and require continuous monitoring and time-dependent analysis, since they consist of only one paddle and thus they cannot get "self-calibrated". It is important to monitor the two PMs of each S2 or S8 paddle versus the event number simultaneously in order to safely determine the corrections needed. An example of such investigation is shown in Fig. 4.17, where the raw time signals from the two PMs of the S8 scintillator are plotted versus the event number together with their average and their difference. To understand this figure one should have in mind Eqs. 4.3 and 4.4 presented in Section 4.2.1, which express that

- a change in the beam velocity (i.e. change in t_0 of the hit) would result in both time signals moving at the same direction and by the same number of channels; thus, their average should change accordingly while their difference should not change,
- a change in the beam position on the detector would result in the two signals moving at opposite directions by the same number of channels, while their average should not change.

The first case can also occur if both signals are read out by the same electronic module, which can cause a "jump" of the same number of channels for both signals. It is this "jump" that one wants to identify and correct. However, a change in the beam velocity can be excluded since it is usually intended and probably documented. With the above considerations it is evident that in Fig. 4.17 the time signal (t_2) of the second PM (top right) needs correction as it appears to change without the time signal (t_1) of the first PM (top left) changing accordingly.

The PSP detectors also appear to have time-dependent behaviour in the present experiment. In Fig. 4.18 the energy signal from the PSP cathode, which is used for getting the total energy loss (ΔE), and thus the charge (Z) of the ions passing through the detector, is plotted versus the event number. It is clear that the detector collects less and less charge as the event number increases. This drift is corrected by varying the gain calibration parameter (G) of the cathode signal as a linear function of the file-number (fn), such that

$$\mathrm{Z} = G(fn) \cdot \sqrt{\Delta E} \cdot g(\beta), \tag{4.34}$$

where $g(\beta)$ describes the velocity dependence of the energy loss. This correction is performed within the *land02* code, which provides a way to vary the calibration parameters very effectively for every run, file and even for single events.

As mentioned in Section 4.2, position reconstruction in each PSP is non-linearly distorted. This is corrected during their position calibration with the active pixel

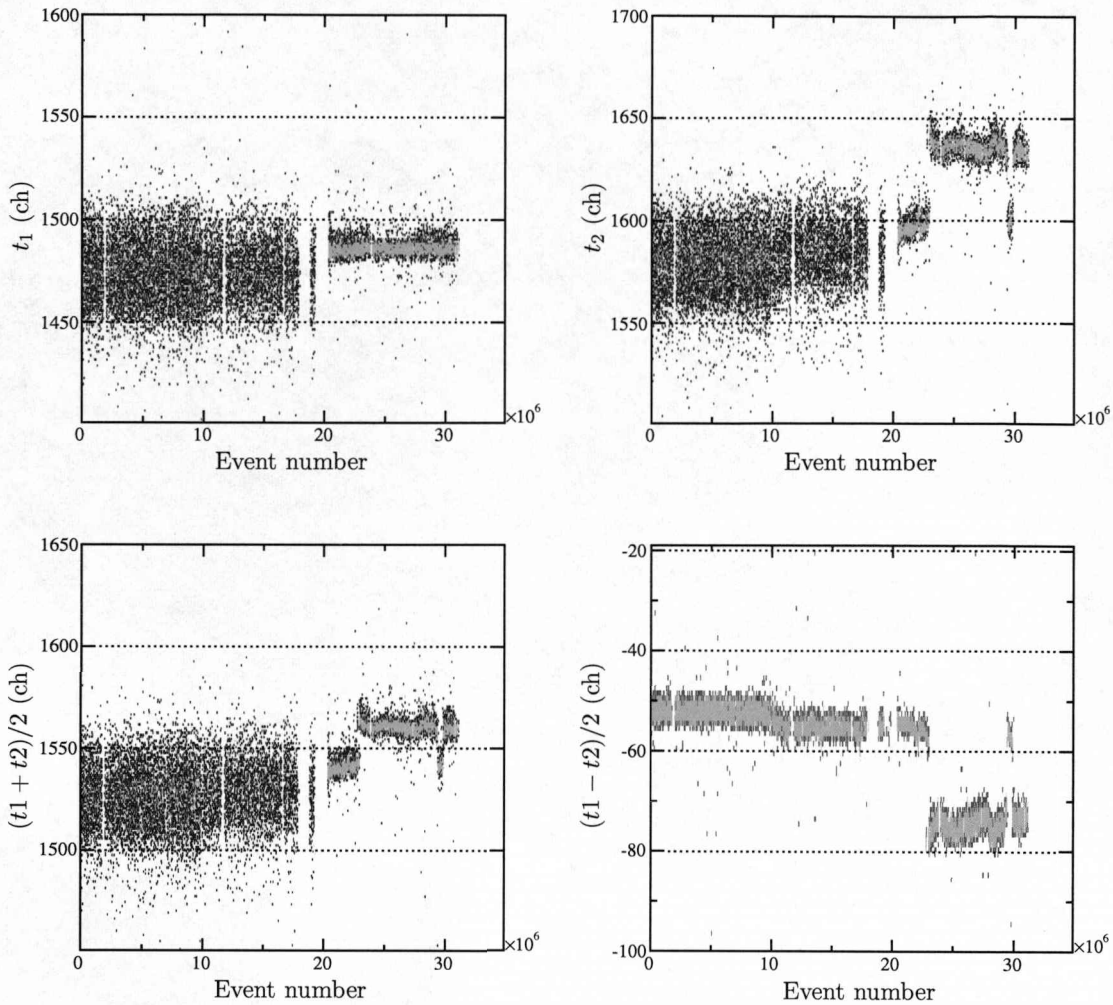

Figure 4.17: Raw time signal from S8 scintillator versus the event number for PM_1 (top left) and PM_2 (top right). Also plotted (bottom) are the average of the two signals (bottom left), which is associated to the "real" (t_0) time of a hit, and their difference (bottom right), which is associated with the x position of the hit in the detector.

mask. The reconstructed position, however, is also changing with time during the present experiment. In other words the position calibration obtained with the use of the pixel mask is valid only for runs not far away from the position-calibration runs. Thus, the anode signals of the PSP detectors also drift with time, but since they are position dependent they are quite broad and these changes are not evident by plotting the individual anode signals, as in the case of the cathode signal (Fig. 4.18). However, when combining the four anode signals for reconstructing the position, these drifts cause a significant change in this position. This is evident when plotting pixels from different calibration runs, as shown in Fig. 4.19. It is also evident that, apart from the drift in the gains, there is an additional distortion around the central area of this

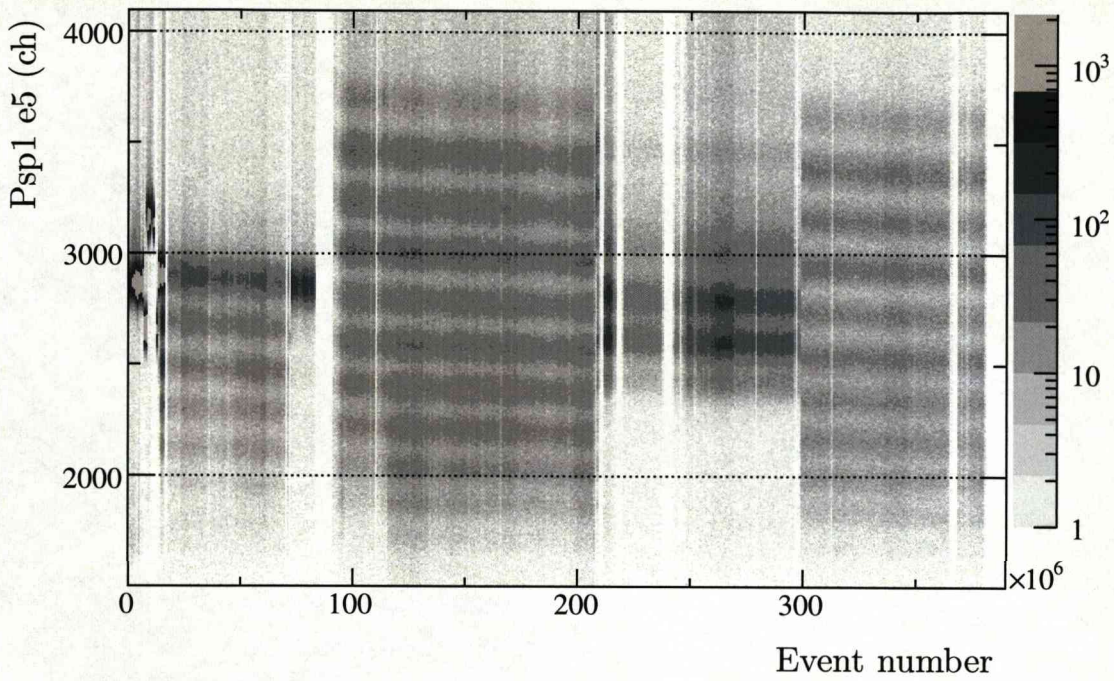

Figure 4.18: Raw energy signal from the cathode of PSP1 versus the event number. A smooth change in the energy signal towards lower channel number as a function of increasing event number is evident.

specific PSP detector. Similar drift of the gains occurred in all three PSPs; however, their distortion was smaller.

Total drift of the pixel position is of the order of 0.5 - 1.5 mm, which is much bigger than the claimed position resolution of the detector and thus it significantly affects the measurements. Monitoring and correction of this drift is achieved using the assumptions and the method described below.

Since the position of all pixels, i.e. any position in the detector, is reconstructed from the same four signals for each PSP, it is reasonable to assume that when there is a drift in the gains of these signals it affects simultaneously all pixels, i.e. the whole detector area. It is further assumed that each pixel position during this drift is moving on the line defined by the initial position, obtained from the calibration run at the beginning of the experiment, and the final position, obtained from the calibration run near the end. With these assumptions it is possible now to define several grids representing intermediate situations of the detector's response. Such grids are then used to calculate the overall angular resolution obtained from the positions of the three PSP position measurements (see Section 4.3.2) for all files. It is clear that the grid that represents better the condition of the detector at that moment (file) should minimise the angular resolution. An example of such minimisation procedure is shown in Fig. 4.20.

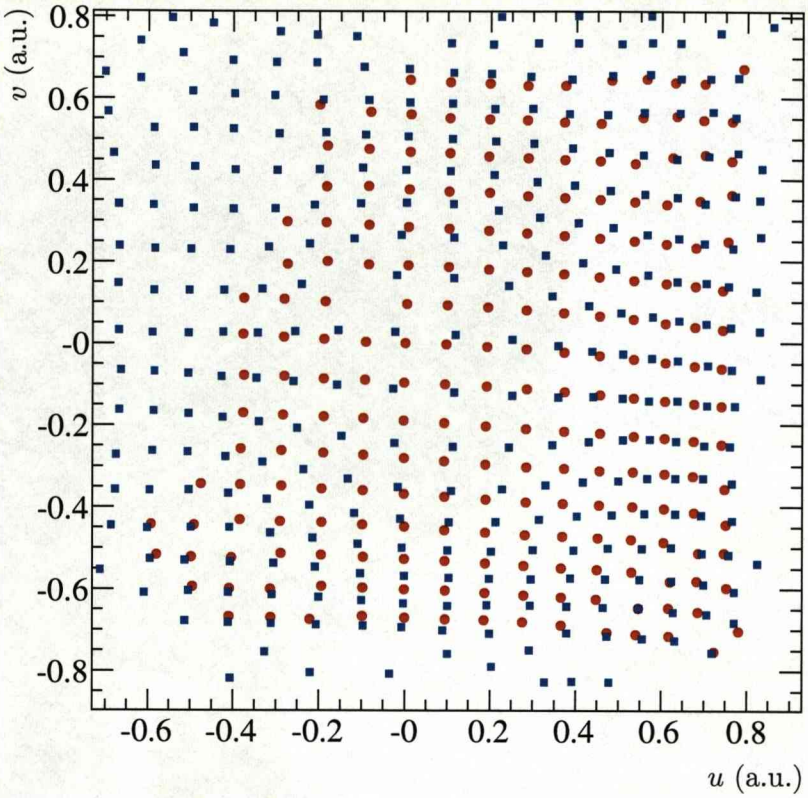

Figure 4.19: Pixel position reconstructed in PSP2 for pixel calibration runs performed at the start of the experiment (red circles) and towards the end (blue squares).

4.5 Projectile particle identification

Relativistic radioactive beams induced by in-flight fragmentation of a primary beam consist of a cocktail of ions and it is, thus, necessary to identify them in terms of mass and charge on an event-by-event basis. For this purpose the secondary beam is followed through a magnetic spectrometer where the particle identification is achieved by measuring the energy loss, the time of flight and the position of each ion. The principles used for obtaining mass and charge through these measurements are discussed in more detail in the following sections.

4.5.1 Projectile charge calibration

The specific energy loss of a charged particle moving through matter depends on the charge (Z) and the velocity (β) of this particle according to the Bethe-Bloch formula (see Eq. 3.1), as described in Section 3.4.2. For the analysis of the present experiment a function of the Bethe-Bloch formula is implemented in the *land02* code such that it takes as inputs the type and thickness of the material, the energy-loss and the velocity measurements for the moving charged particle, and delivers its charge. The

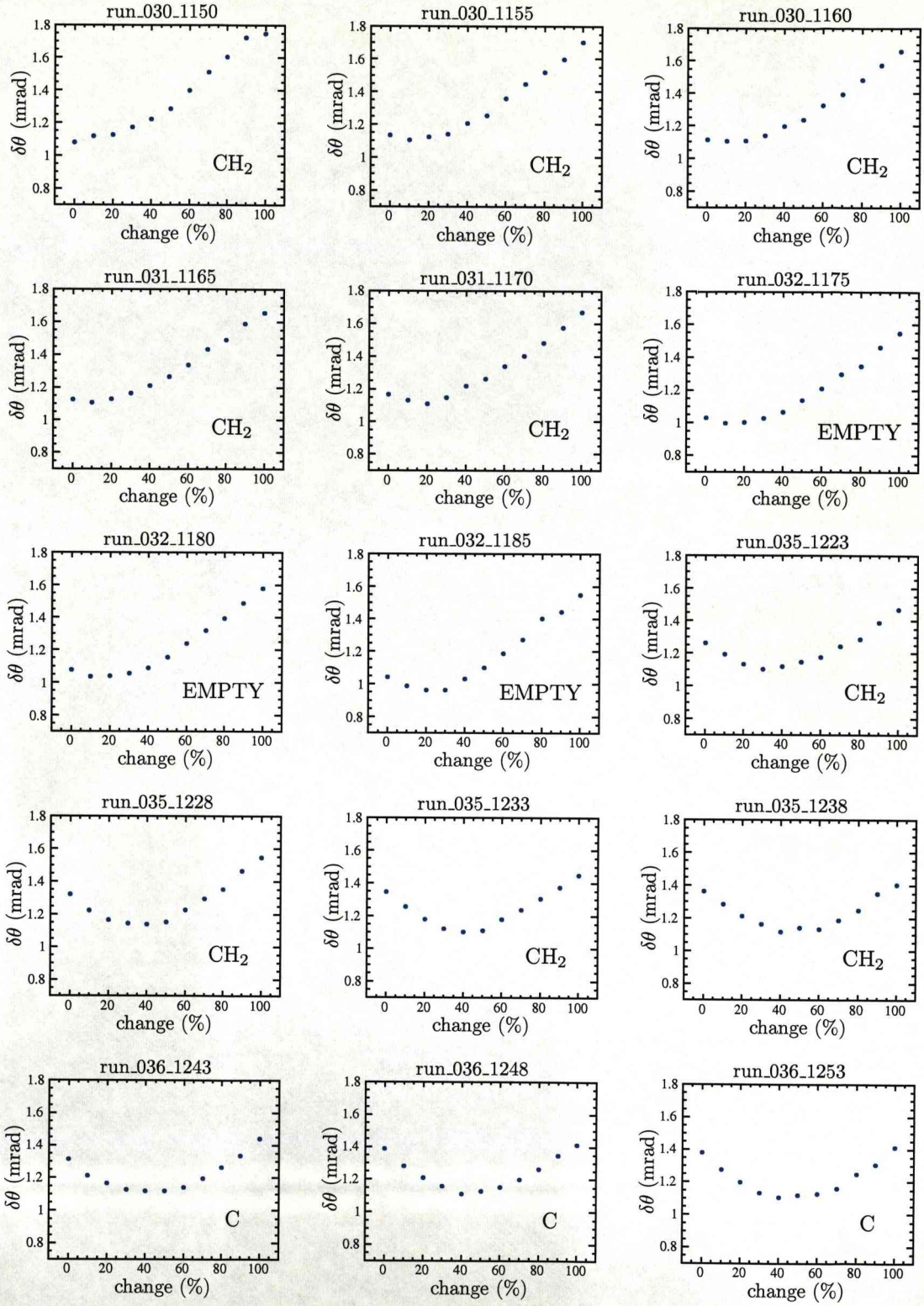

Figure 4.20: Angular resolution at the target position obtained from tracking the beam with the three PSPs using pixel grids that represent different percentage of the total change between the first (early in experiment) and the second (near the end) calibration run for PSP2. It is clear that the drift occurs gradually and can be very well corrected using the assumptions discussed in the text.

only calibration parameter that needs to be determined is a proportionality factor so that the energy-loss measurement is in MeV units.

In the analysis of earlier experiments, however, the charge-calibration procedure was performed in an equivalent but less transparent way, requiring the use of an external software package (e.g. ATIMA [69]), as described below. To perform the charge calibration in this way, an assumption is needed that the Bethe-Bloch formula (see Eq. 3.1) can be written in the following simplified form

$$\frac{dE}{dx} = \lambda f(\beta) \mathrm{Z}^2, \tag{4.35}$$

where λ is a proportionality factor. The dependence of the energy loss on the velocity ($f(\beta)$) is expected to be of the form β^{κ}, where κ is determined through a fit of data-points obtained from an external simulation package (ATIMA) (see middle plot of Fig. 4.21). To determine the proportionality factor λ and ensure that the calculated dependency ($f(\beta)$) agrees with the experimental observations, calibration runs with different beam energies are used.

To justify that the two methods are equivalent (i.e. function in the *land02* and external software ATIMA) a comparison between their results is shown in Fig. 4.21. In this figure the energy loss of ^{58}Ni ions has been calculated for energies ranging from 300 - 700 MeV/nucleon using the ATIMA code and the Bethe-Bloch formula implemented in *land02*. Calculations using *land02* are systematically lower than the ones produced by ATIMA. However, by normalising one point, e.g. 540 MeV/nucleon, the two calculations agree within few keV/nucleon, as illustrated at the bottom plot of Fig. 4.21

4.5.2 Projectile A/Z calibration

The mass-over-charge ratio (A/Z) of an ion passing through a constant magnetic field (B) with velocity (β) can be determined using the following formula

$$\mathrm{A/Z} = \frac{e}{uc} \frac{B\rho}{\beta\gamma}, \tag{4.36}$$

where e is the electron charge, u is the atomic-mass unit and c is the speed of light. Thus, it is required to measure the velocity of the ion and its magnetic rigidity ($B\rho$). The velocity is obtained through time-of-flight measurements, as described in Section 4.3.1. The nominal magnetic rigidity ($B\rho_0$) is obtained from the settings of the FRS magnets. An ion of charge Z_0 and momentum P_0 that travels in the central trajectory (reference trajectory) of the FRS setting satisfies the following equation

$$\frac{P_0}{\mathrm{Z}} = B\rho_0. \tag{4.37}$$

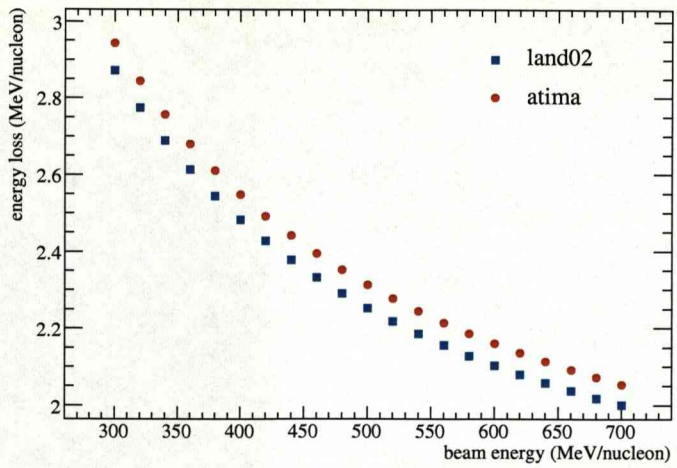

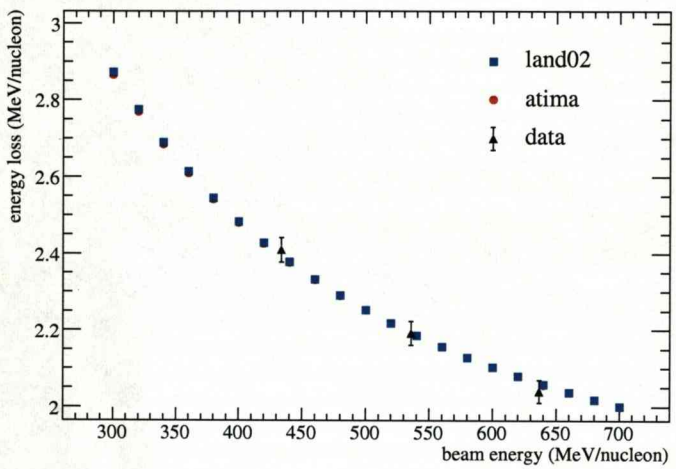

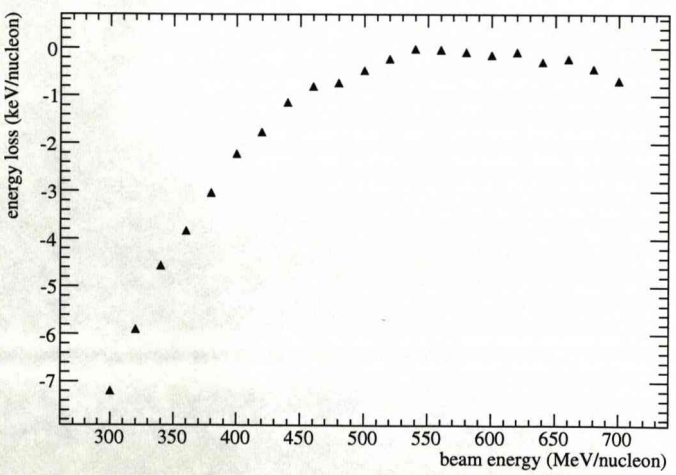

Figure 4.21: Energy loss per nucleon of a ^{58}Ni beam for different beam energies calculated with ATIMA and *land02*. Calculations with *land02* are systematically lower than the ones produced by ATIMA; however, the trend is in very good agreement since by fixing one point (middle plot) the two calculations become almost identical with a difference less than a few keV/nucleon (bottom).

Ions, however, that travel through the FRS magnets with a trajectory that deviates from the reference trajectory have a different momentum-over-charge ratio and thus, for Eq. 4.37 to be valid, a different magnetic rigidity ($B\rho$). To determine for each ion the deviation of its magnetic rigidity from the reference magnetic rigidity, position measurements at the dispersive (F2) and achromatic (F8) planes of the spectrometer are required using the FGR, S2 and S8 scintillators. The magnetic rigidity for each ion is then calculated by the equation

$$B\rho = B\rho_0 \cdot \left(1 - \frac{X_{S8} - M \cdot X_{S2}}{D_8 \cdot 100}\right), \tag{4.38}$$

where M is the magnification of the achromatic system, $M = -D_8/D_2$, and D_2 and D_8 are the dispersions at the focal planes F2 and F8, respectively. In the case where the beam is centred at S8 ($X_{S8} = 0$), Eq. 4.38 can be simplified as follows

$$B\rho = B\rho_0 \cdot \left(1 + \frac{M \cdot X_{S2}}{D_8 \cdot 100}\right), \tag{4.39}$$

or

$$B\rho = B\rho_0 \cdot \left(1 + \frac{X_{S2}}{-D_2 \cdot 100}\right). \tag{4.40}$$

Using the measured velocity and magnetic rigidity of the ion in Eq. 4.36, the mass-over-charge ratio is obtained with a precision better than 0.2% for secondary beams. In this experiment the secondary fragments have mass and charge around A $\approx$ 70 and Z $\approx$ 28, respectively. In other words, the difference in the mass-over-charge ratio for isotopes with neighbouring masses is $\sim$ 1.5%, which means that the resolving power of the spectrometer should be better than $\sigma = 0.5\%$ in order to safely distinguish them. It is evident from the aforementioned estimates that the high resolving power of the FRS spectrometer allows for an unambiguous mass identification of nuclides in this mass region, as illustrated in the particle-identification (PID) plots of Figs. 4.22 and 4.23 for the four different settings used in the present experiment.

4.6 Heavy fragment particle identification

Once identified by the FRS spectrometer, the ions reach the secondary target in Cave C, where they react and produce a series of new isotopes which also need to be identified in terms of mass and charge. As in the case of the projectile particle identification, where the mass-over-charge ratio was determined through time-of-flight and position measurements, in the case of heavy reaction fragments a combination of time-of-flight and position measurements is also required.

In the FRS the distances are large (S2 - S8 $\approx$ 85 m and S8 - POS $\approx$ 55 m), which results in isotopes with different masses having a time difference comparable to the

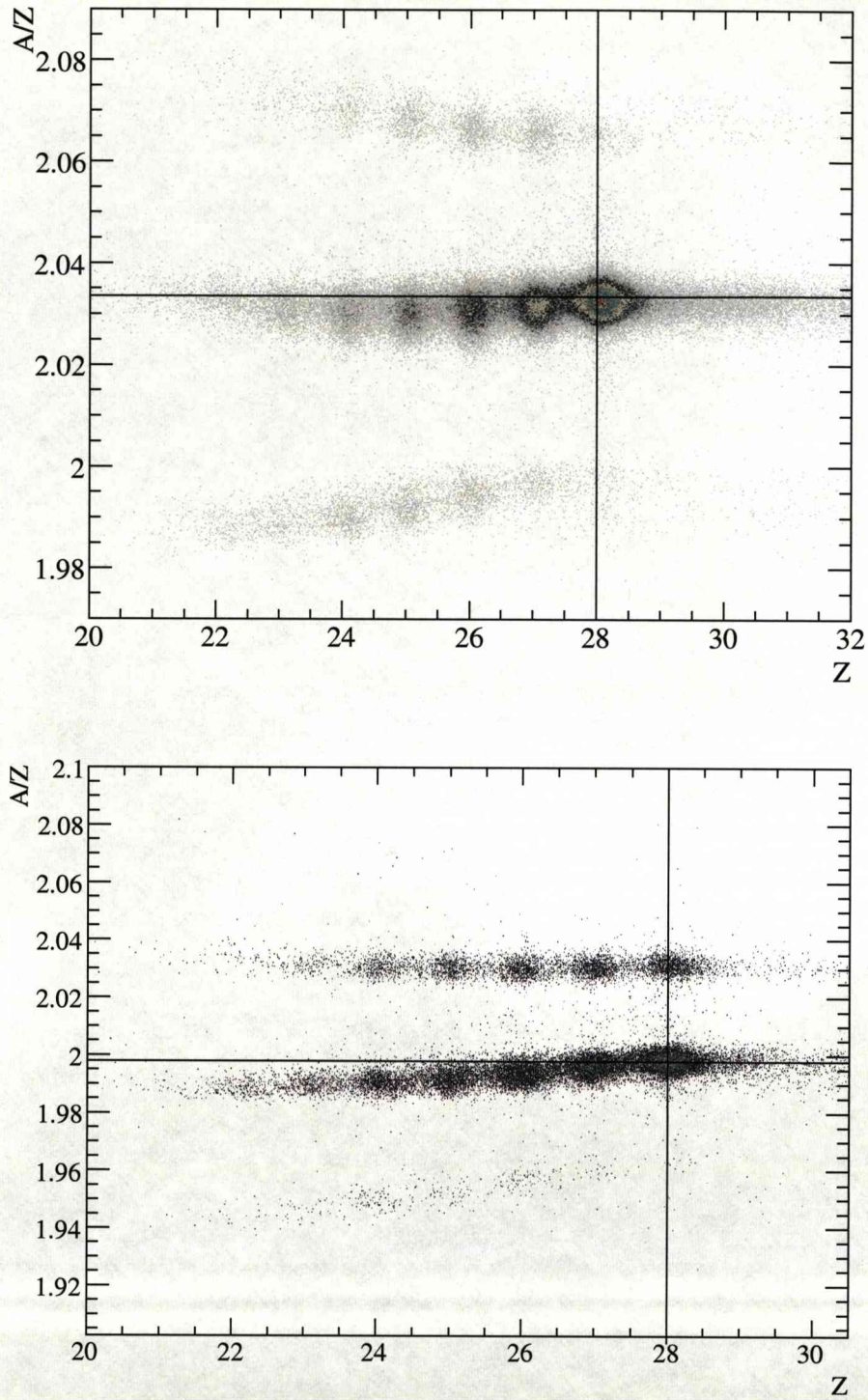

Figure 4.22: Particle-identification (PID) plots of incoming secondary beam. The FRS setup is optimised for the transmission of ^{57}Ni (top) and ^{56}Ni (bottom) isotopes. The cross in each plot shows the expected position of these isotopes on the PID plot.

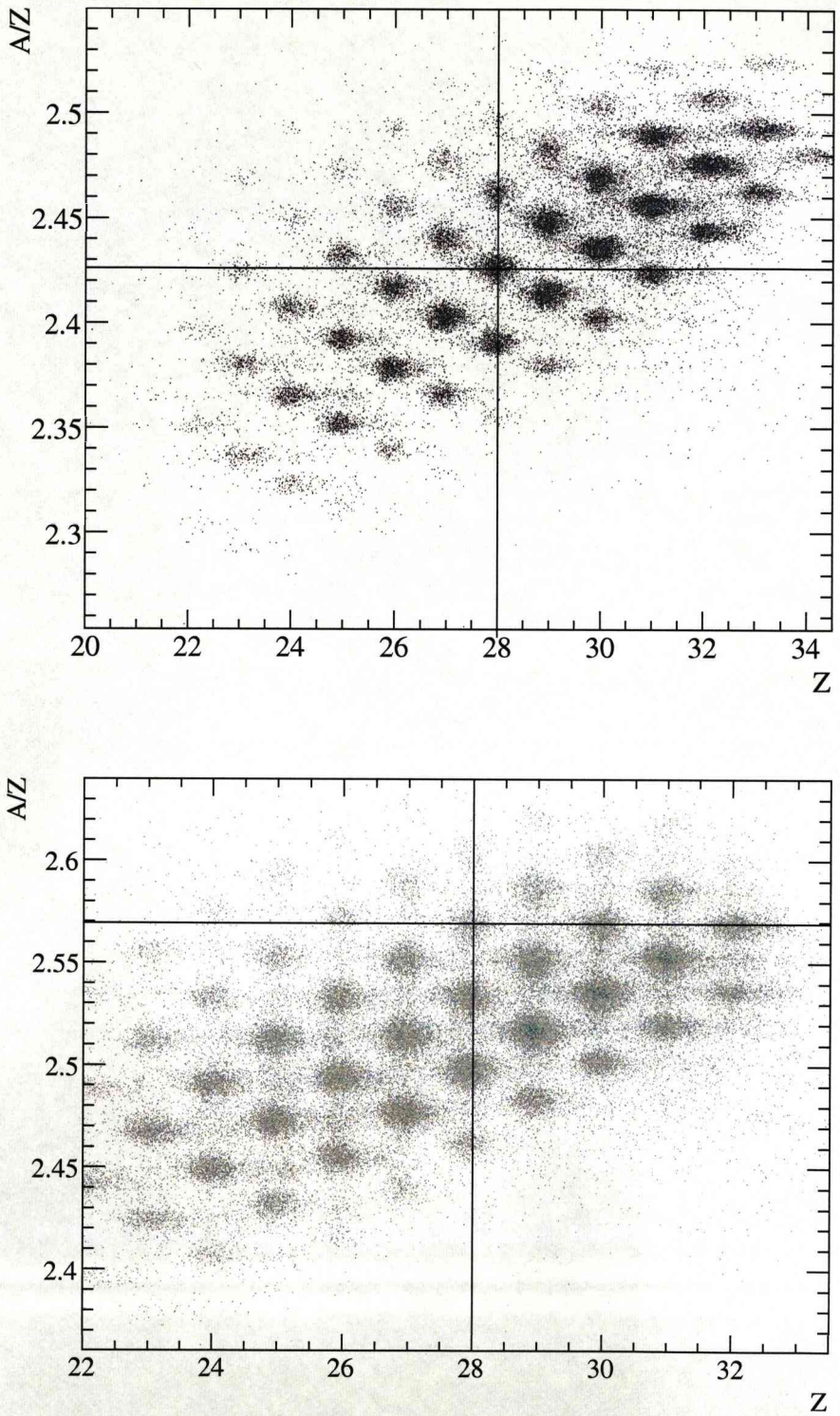

Figure 4.23: Particle-identification (PID) plots of incoming secondary beam. The FRS setup is optimised for the transmission of ^{68}Ni (top) and ^{72}Ni (bottom) isotopes. The cross in each plot shows the expected position of these isotopes on the PID plot.

time resolution of the FRS setup. In Cave C, however, the total flight path (from the target to the last detector) is only $\sim$ 17 m and time differences for different masses are much smaller than the time resolution of the LAND/ALADIN setup.

In addition, for the ALADIN dipole magnet, the position of the fragment after the magnet does not depend only on its magnetic rigidity, but also on its angle, position and velocity before the magnet. The FRS spectrometer, with a combination of four dipole and a few multipole magnets, cancels out dependencies on the incoming angle and position. The position of the fragments after the first two dipoles depends only on their magnetic rigidity (dispersive plane). After the second stage of the FRS all fragments are focused on the same position, independently of their magnetic rigidity, incoming angle or position.

These two factors, i.e. short distances and a single large acceptance dipole magnet, make the mass identification after the target a tedious task, which requires precise tracking through the ALADIN magnet with a set of measurements before and after the magnet with position resolution of σ = 200 - 300 μm. In contrast, at the FRS a single measurement of the displacement at the dispersive focal plane with a resolution not better than $\sigma \approx 1$ cm is enough to uniquely identify the masses at the region of interest (i.e. mass numbers around A $\approx$ 60 - 70).

The principles used for obtaining the mass-over-charge ratio of the heavy reaction fragments are presented in the following section. The charge of the heavy reaction fragments is determined with similar considerations as the ones described earlier in Section 4.5.1.

4.6.1 Fragment A/Z and trajectory calibrations

A matrix representation is commonly used to describe the passage of a charged particle through an ion-optical system. Each ion-optical element is represented by a matrix. The position x, the angle θ and the momentum p of a particle (A, Z) can be estimated at any place through the ion-optical system as a function of its initial variables (x_1, θ_1, p_1) and with respect to a reference trajectory of a particle (A_0, Z_0) moving with momentum p_0. For simplicity and to be able to solve the equations analytically a first order approximation is assumed. In reality, however, the description of the exact track of a charged particle through magnets requires higher order corrections. As discussed in Ref. [70], any deviations of the real trajectory from the first order approximation are referred to as aberrations and can be due to the mathematical simplifications requiring for example small angles, as well as due to imperfections in the magnetic field and misalignment of the ion-optical elements. The ion-optical system in Cave C (Fig. 4.24) is rather simple and can be approached assuming three different types of ion-optical elements discussed below [71].

Let $\mathcal{S}$ be the transport matrix for a field-free region, e.g. from the last position

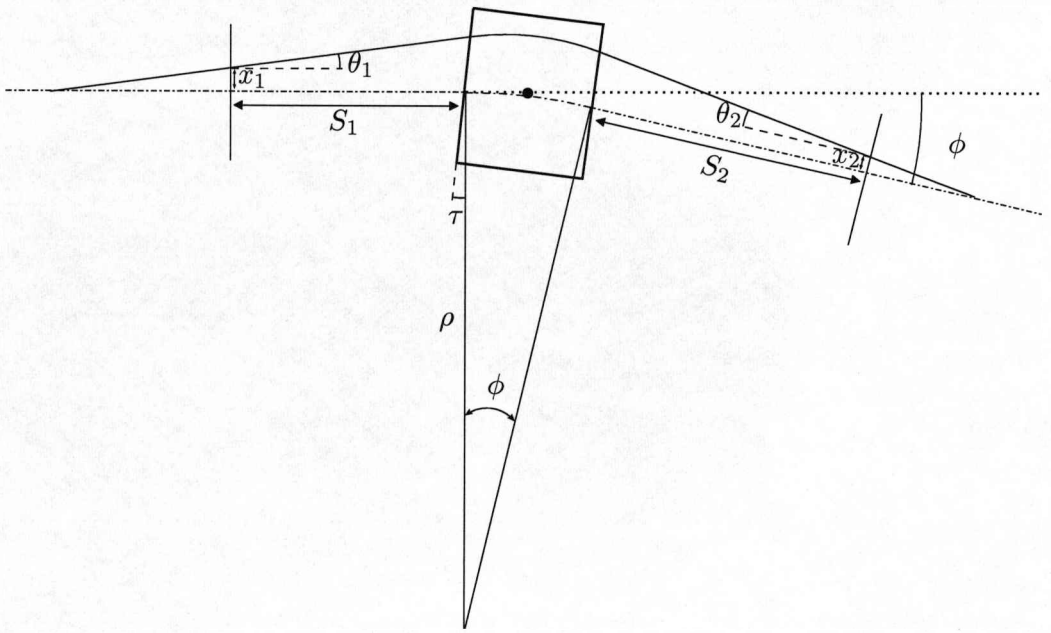

Figure 4.24: The trajectory of a charged particle through a dipole magnet (solid line) is measured relative to the reference trajectory (dot-dashed line).

measurement before the magnet to the entrance of the magnetic field (S_1) or from the exit of the magnetic field to the first position measurement after the magnet (S_2),

$$\mathcal{S}_i = \begin{pmatrix} 1 & S_i & 0 \\ 0 & 1 & 0 \\ 0 & 0 & 1 \end{pmatrix}, \; i = 1, 2. \tag{4.41}$$

The matrix F describes the "kick" that a charged particle feels when entering (F_1) or exiting (F_2) the magnetic field with a certain angle,

$$F_1 = F_2 = \begin{pmatrix} 1 & 1 & 0 \\ \tan\tau/\rho & 1 & 0 \\ 0 & 0 & 1 \end{pmatrix}. \tag{4.42}$$

This phenomenon is known as fringing field. The following matrix M describes the passage of a charged particle through a uniform magnetic field,

$$M = \begin{pmatrix} \cos\phi & \rho\sin\phi & \rho(1-\cos\phi) \\ -\sin\phi/\rho & \cos\phi & \sin\phi \\ 0 & 0 & 1 \end{pmatrix}, \tag{4.43}$$

where the last row (0 0 1) reflects the fact that the magnitude of the momentum vector does not change through a uniform static magnetic field.

Combining the above matrices such that they describe the full track of a particle through a dipole magnet, from the last x-position measurement before the magnet to the first x-position measurement after the magnet, one gets the following equation

$$\begin{pmatrix} x_2 \\ \theta_2 \\ (dp/p_0)_2 \end{pmatrix} = \mathcal{S}_2 \cdot F_2 \cdot M \cdot F_1 \cdot \mathcal{S}_1 \cdot \begin{pmatrix} x_1 \\ \theta_1 \\ (dp/p_0)_1 \end{pmatrix}. \tag{4.44}$$

By substituting $\mathcal{S}$, M, F matrices, Eq. 4.44 takes the form

$$\begin{pmatrix} x_2 \\ \theta_2 \\ (dp/p_0)_2 \end{pmatrix} = \begin{pmatrix} ax_1 + b\theta_1 + c(dp/p_0)_1 \\ ex_1 + f\theta_1 + g(dp/p_0)_1 \\ hx_1 + j\theta_1 + k(dp/p_0)_1 \end{pmatrix}, \tag{4.45}$$

where the coefficients a, b, c, e, f, g, h, j, k are found from the multiplication of the matrices. The above set of equations is valid when the reference and the measured particles are the same isotope; for different isotopes the momentum term (dp/p_0) must be replaced with the more general magnetic-rigidity (momentum-over-charge) term $(d(B\rho)/B\rho_0)$. Using Eq. 4.45 it can be shown that three position measurements (two position measurements before the magnet and one after or vice-versa) are sufficient for the determination of the difference in magnetic rigidity. The mass of the charged particle can be expressed as a function of the difference in magnetic rigidity through the following equation

$$\mathrm{A} = \mathrm{A}_0 \left(1 + \frac{d(B\rho)}{B\rho_0}\right) \frac{\mathrm{Z}}{\mathrm{Z}_0} \frac{\beta_0\gamma_0}{\beta\gamma}, \tag{4.46}$$

where Z and $\beta\gamma$ are determined through energy-loss and time-of-flight measurements, respectively. Using the method described in this section to obtain the mass of a charged particle through the ALADIN magnet, a resolution of $\sim 0.5\%$ is achieved for the outgoing heavy reaction fragments. This mass resolution is sufficiently good for distinguishing neighbouring masses, as illustrated in the PID plot of Fig. 4.25.

4.7 Discussion

In this chapter the ideas behind the calibration and the hit reconstruction procedures for the S2, S8, FGR, POS, PSP, GFI, TFW and LAND detectors have been discussed in more or less detail, together with the present status of the tracking through the FRS spectrometer and the ALADIN dipole magnet. Most of these procedures have been implemented in the *land02* framework such that they can be reused not only for the off-line analysis of previous experiments but also for the on-line monitoring and analysis of future experiments. However, the "full glory" of such a framework will become evident only when a "proper" tracking algorithm will take control of the tracking through the FRS spectrometer and particularly through the ALADIN magnet. The tracking method discussed in the previous section introduces some limitations which have become clear in the analysis of the present experiment as well.

In particular, an essential improvement of the tracking software is to include all the position measurements which are available in these type of experiments in the

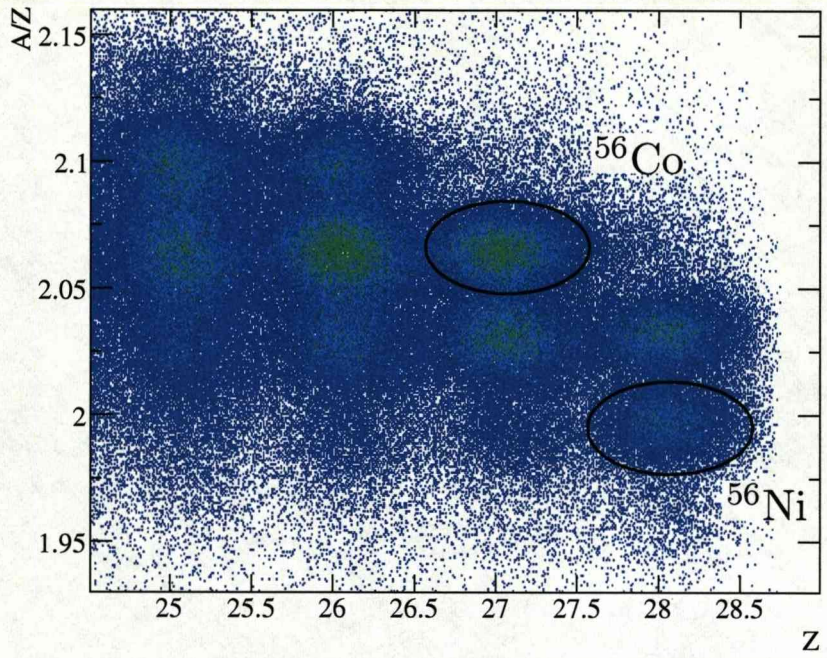

Figure 4.25: Particle-identification (PID) plot obtained from the tracking of the heavy reaction fragments through the ALADIN magnet. The PID plot is produced for incoming ^{57}Ni on a CH_2 target, requiring the presence of the plastic CV detector trigger. The different isotopes produced can be "safely" identified. The outgoing ^{56}Ni (Z = 28) and ^{56}Co (Z = 27) nuclides are highlighted.

determination of the trajectory of the charged particle through the ALADIN magnet. The position measurements, which are obtained after the beam has passed through materials, cannot be simply added to the tracking since they suffer from the straggling in these materials. Methods such as the Kalman filter [72] can come into play in order to include these position measurements in the tracking procedure. Additional position measurements improve the precision of the tracking, given that there is a good estimation of the error of these measurements. The measurement is then accepted (or not) based on a χ^2 criterion.

Another limitation of the existing tracking method affects the velocity measurement. The velocity is currently simply determined as the ratio of the mean flight path through the magnet to the time-of-flight measurement. However, the real flight path that the charged particle follows can deviate significantly from the mean reference path depending on its angle, position and momentum when entering the magnet. It is clear that the velocity of the charged particle should be calculated using the real flight path which can be determined on an event-by-event basis by tracking the particle not only through the ALADIN magnet but throughout the whole setup.

There are also some side benefits that one can obtain from the presence of a "proper"

tracker. For example, once the track of the particle has been determined, it can be used back to the lower level reconstruction to optimise detectors that provide incomplete information. In the present experiment the NTF detector has only one plane, which does not allow the "self-calibration" procedure described in Section 4.2.1 to be applied. However, if the trajectory of the particles that penetrate the NTF detector is known, then the position on the detector is also known and can be used to calibrate the paddles. A sort of iteration procedure between the estimated track and the measurement from the detectors can be used to optimise the tracking precision.

Throughout the analysis of the present experiment it has become evident that the longer-term benefits of the development of a large common analysis framework justify the efforts and sacrifices needed, especially as the setups for nuclear physics experiments grow, become more complicated and more people are getting involved.

Chapter 5

Analysis and results

After the data have passed through the calibration and reconstruction routines described in the previous chapter, they can reveal some useful physical quantities of the ions. However, due to the high beam energy (i.e. 510 MeV/nucleon for the ^{57}Ni secondary fragments), the large number of different ions in the incoming beam and the materials placed along the path of the ions, all sort of reactions and processes are induced. It is therefore essential to apply a series of selections and corrections, in order to isolate specific reaction channels and eliminate the background, before one can extract and study in detail the nuclear processes of interest. In this chapter these selections and corrections are described first (Section 5.1) and then the physics results are presented (Section 5.2) and discussed (Section 5.3).

5.1 Analysis

5.1.1 Selection of the reaction channel

The high resolving power of the FRS spectrometer allows for an unambiguous identification of the incoming beam. By applying appropriate selections on the incoming particles, it is possible to study on an event-by-event basis reactions induced only by a particular nuclide, see Fig. 5.1 where incoming ^{57}Ni is selected.

The next step is to select the outgoing channel. However, before one looks at the masses obtained from tracking through the ALADIN magnet, it is first necessary to make a selection based on the charges of the heavy fragments. In particular, a selection in the correlation between two energy-loss measurements, one at the beginning of the outgoing track (PSP3) and one at the end (TFW), is required, as shown in Fig. 5.2. This procedure provides a way to clean out secondary reactions induced by materials (detectors, vacuum windows, air, etc.) placed after the target, given that the charge of the fragments changes during these reactions. Indeed, fragments that react with the materials after the target are identified by the first detector (PSP3) as having a specific charge (Z), while in the last detector (TFW) their charge is different resulting in this characteristic tail below each "blob" in Fig. 5.2. Only events correlated on

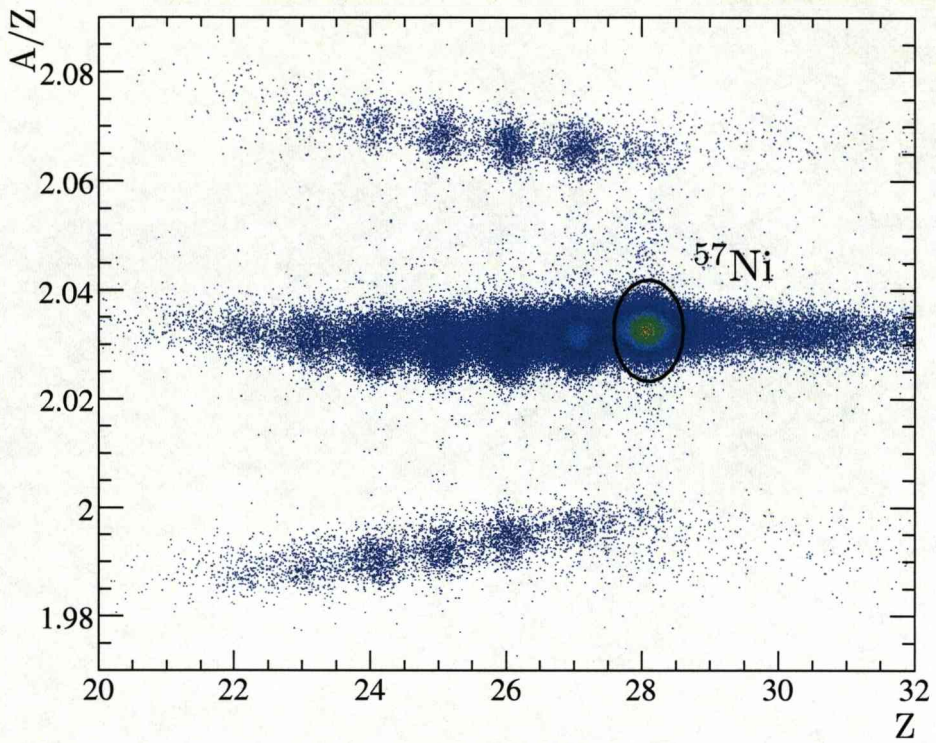

Figure 5.1: Particle identification of the incoming beam. Mass over charge (A/Z axis) is obtained through a combination of time of flight (ToF) measurements (i.e. ToF between S2−S8 and S8−POS) and horizontal displacement measurement at the dispersive plane of the FRS spectrometer. Charge (Z axis) is obtained through energy loss measurements in the PSP1 and PSP2 detectors, placed before the target. Applying appropriate graphical cuts, as the ellipse shown in this figure, one can select events of a particular projectile isotope (e.g. ^{57}Ni).

the diagonal of this figure are useful. This energy-loss correlation, however, cannot eliminate inelastic/elastic reactions in the materials or reactions where only the neutron number has changed.

After "cleaning up" the data from some of the secondary reactions in the materials, a precise tracking of the heavy reaction products through the ALADIN magnet provides a sufficiently good mass resolution despite the limitations discussed in Section 4.6. The resolved masses of the Ni isotopes are shown in Fig. 5.3, where the ^{56}Ni fragment is selected. To obtain this figure the additional condition that a proton has triggered the plastic detector (CV) is applied, otherwise everything is dominated by the unreacted ^{57}Ni beam.

Thus, it is possible at this point to apply appropriate gates on incoming beam and outgoing heavy reaction particles, selecting for example events where only one neutron or one proton has been removed during the reaction with the target. Moreover, additional selections on light outgoing fragments can be applied depending on the

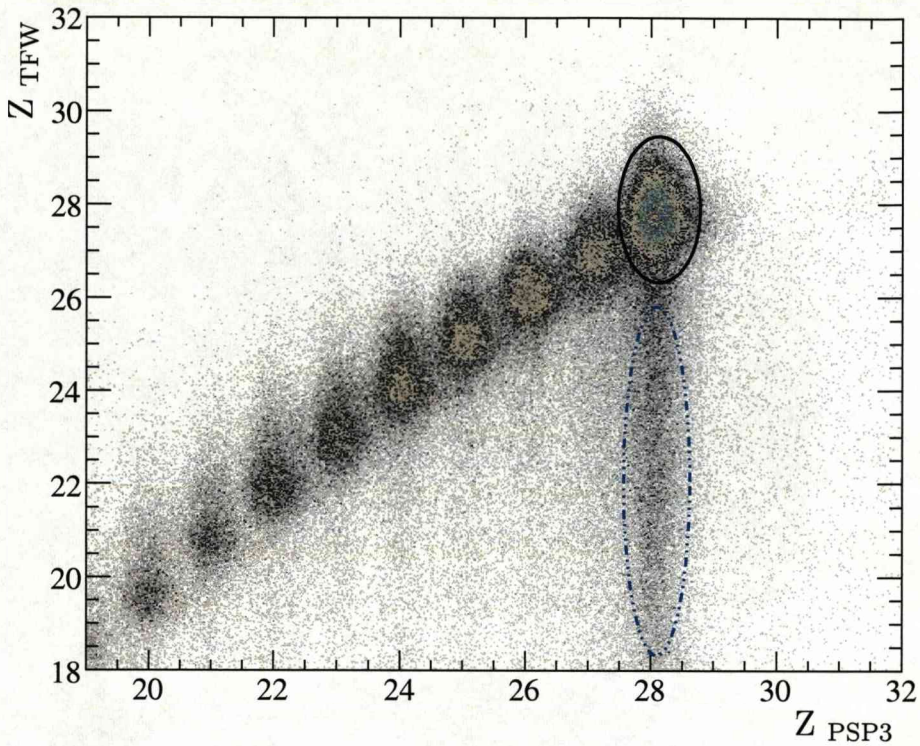

Figure 5.2: Correlation of two energy-loss measurements after the target, one at the PSP3 detector close to the target and one at the TFW detector at the end of the track ($\sim$ 17 m downstream). The graphical cuts (black ellipse, solid line) on this 2D plot select a specific charge for the outgoing fragments and cleans up events that have reacted with the (non target) materials after or at PSP3 (blue ellipse, dot-dashed line).

specific reaction, requiring for example a neutron in the neutron detector (LAND), or a proton in the plastic detector (CV) around the target, or a γ ray, a proton or a neutron in the CsI array (CS). In this way specific reaction channels can be probed, such as the diffraction breakup or the (p,2p) and the (p,pn) reactions, excluding other processes that take place in the target area.

The detection of light particles in the target-recoil detectors (CV, CS) has been extensively used for obtaining the results presented in this thesis. The arrangement of these detectors is shown in Fig. 5.4. The twelve paddles of the CV detector around the target are arranged in such a way that they cover in ϕ the full 2π azimuthal angle and the forward polar angles from $\sim 10\,^\circ$ to $90\,^\circ$. The energy signal of the paddles is shown in Fig. 5.5 for fast protons. The CsI array surrounds the CV detector and it is also granulated in twelve ϕ sectors. In addition, it is granulated in twelve θ sectors, such that each of the 144 CsI crystals has a unique (ϕ, θ) index which is written in this thesis as (Csi (ϕ), Csi (θ)). Its energy spectrum from all crystals before gainmatching is shown in Fig. 5.6. In this figure the large energies are considered to be fast protons.

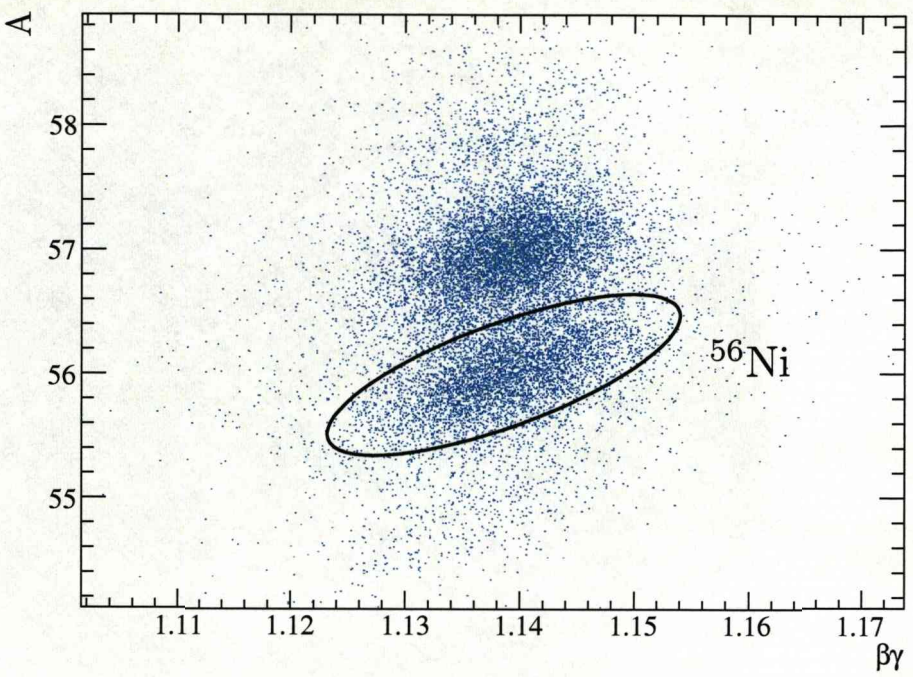

Figure 5.3: Identification plot of Ni fragments (i.e. gate on Z = 28 in Fig. 5.2) from a $\sim$ 500 MeV/nucleon ^{57}Ni incident beam on the CH_2 target, with the additional requirement that the CV detector around the target has multiplicity one.

Although both detectors provide a poor angular resolution of 30 ° in ϕ, they allow for some interesting kinematical correlations to be observed, as discussed in Sections 5.2 and 5.3.

5.1.2 Background subtraction

Despite the aforementioned selections in the incoming and outgoing heavy fragments and the requirements for protons, neutrons or γ rays in specific detectors, there is still a substantial amount of residual background contribution in the spectra that needs to be estimated and subtracted. For this purpose, runs with an empty target are performed throughout the experiment to provide a quantitative estimation of this background. The runs without the target are analysed applying exactly the same conditions as for the ones with the target and the obtained spectra (or cross sections) are normalised and subtracted from the measurements with the target. A sort of background subtraction can be performed also between runs with different targets. For example, in order to probe reactions induced only by the H atoms of the CH_2 target, the carbon contribution needs to be subtracted from the spectra as background. In this case the runs with the pure carbon target can be used to estimate the carbon contribution in reactions with the CH_2 target.

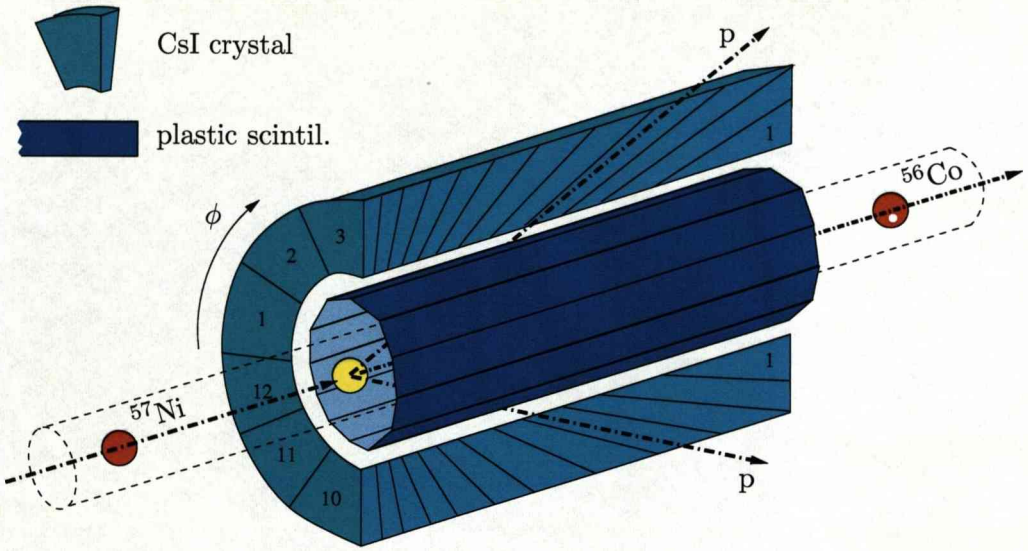

Figure 5.4: The twelve plastic paddles of the CV detector are placed between the beam pipe and the CsI array, covering the full 2π angle in ϕ and from $\sim 10°$ to $90°$ in θ. For simplicity only half of the CsI array is shown in this figure. The scattered proton triggers a plastic paddle and then enters one of the CsI crystals placed at the same ϕ angle, "behind" the paddle.

In some cases, depending on the observable, the spectra obtained with empty target need to be folded with the influence that the presence of the target material has (in this specific measurement) and then subtracted as background. A typical example of background subtraction is discussed in the following section for the momentum distribution measurements.

5.1.3 Momentum distribution analysis

When a nuclear reaction occurs, such as the removal of a nucleon from the projectile nucleus by the target, the width of the momentum distribution of the residual fragment can be linked to the orbital angular momentum of the removed nucleon through the theoretical considerations discussed in Chapter 2. The width of the momentum distribution (in one dimension) of the residual fragment, when one nucleon is "suddenly" removed from a bound state of the projectile nucleus, is of the order of 100 - 200 MeV/c, as discussed in Ref. [31]. The momentum distribution measurements are usually presented in the literature as the projection of the momentum on one of the coordinates, i.e. either on the axis parallel to the beam direction (longitudinal) or on one of the axes which are perpendicular to the beam direction (x or y projection of the transverse component, $P_{\perp}^{x}$ or $P_{\perp}^{y}$). In general, it is preferred to measure the longitudinal com-

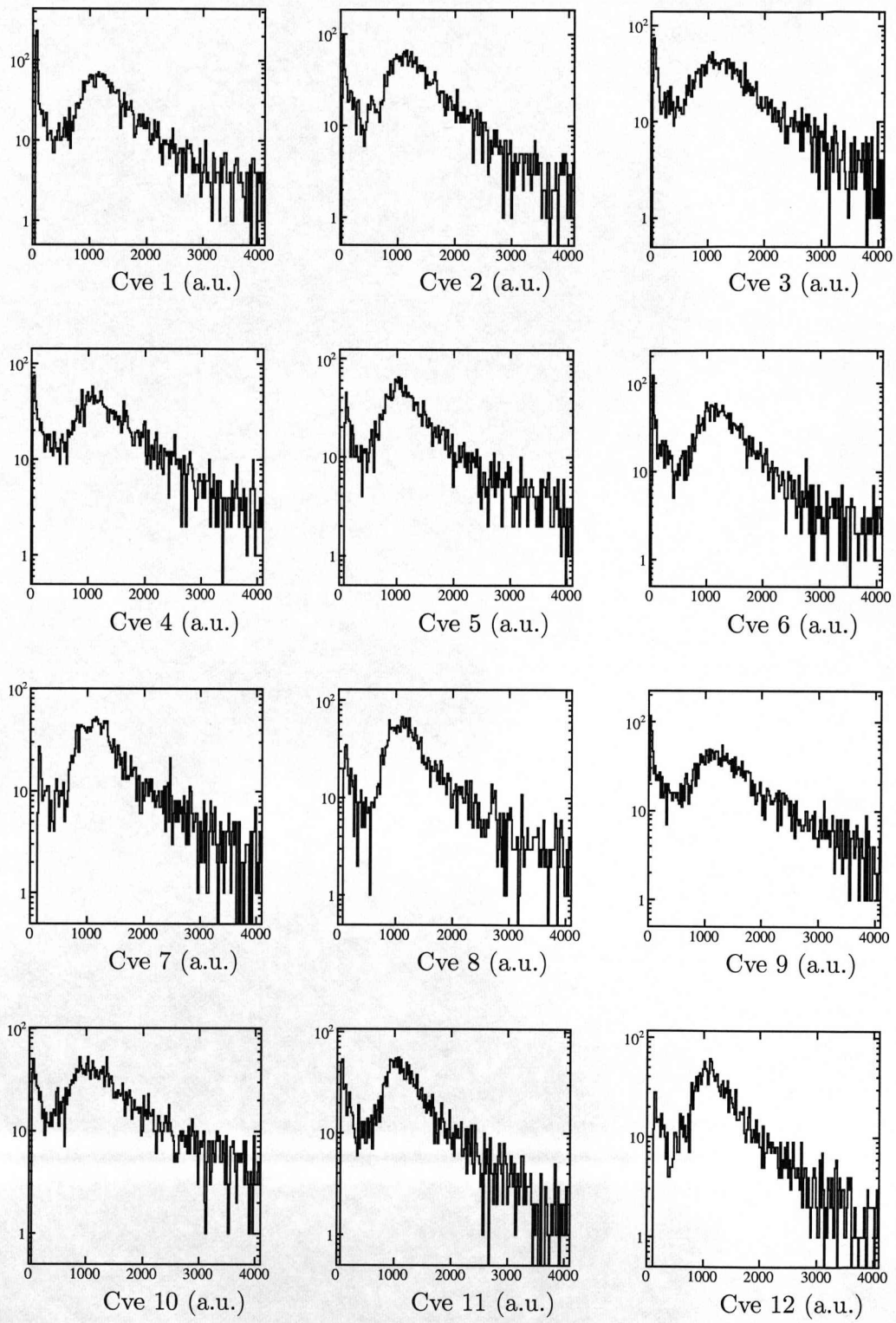

Figure 5.5: The proton energy signals from the twelve plastic paddles for the CH_2 target, after selecting ^{57}Ni incoming beam and ^{56}Co outgoing fragments.

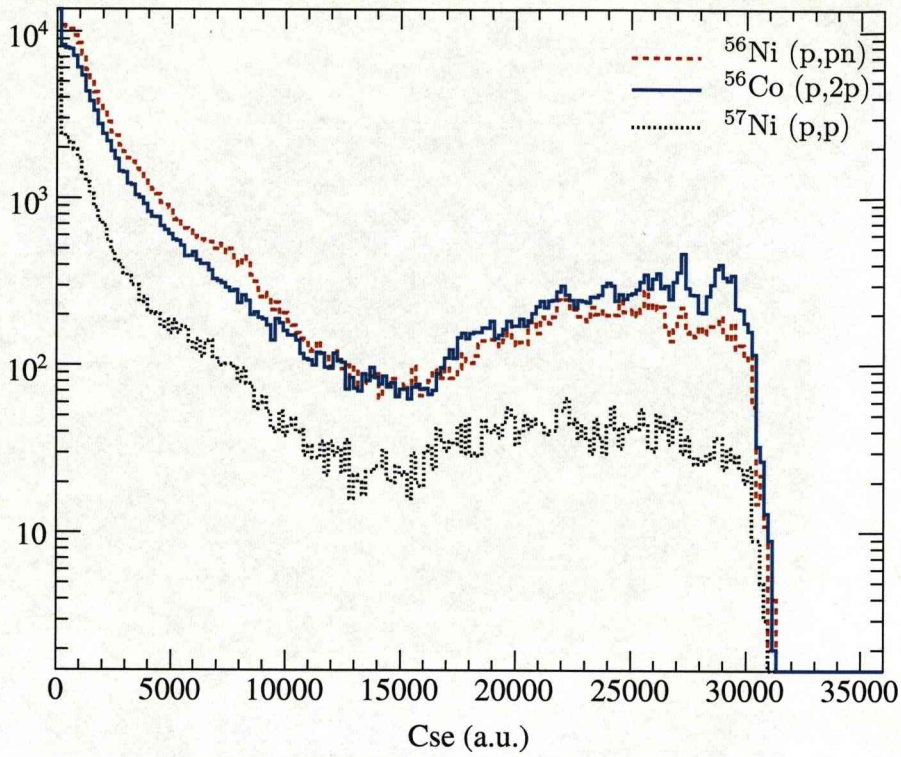

Figure 5.6: The CsI energy spectrum (in arbitrary units) obtained from all crystals before gainmatching for the CH_2 target and by selecting ^{56}Ni (blue), ^{56}Co (red dashed) and ^{57}Ni (black) outgoing fragments.

ponent of the momentum ($P_{\parallel}$) rather than the transverse one ($P_{\perp}$), which is much more affected by the Coulomb deflection. However, due to the high momentum of the beam ($\sim$ 60 GeV/c) in the present experiment, the measurement of the longitudinal momentum requires a resolving power of the order of 0.1%, which is not achievable with the present LAND/ALADIN setup. Instead, the transverse component of the momentum is measured by determining the change between the incoming and outgoing angle of the projectile-like fragment at the target position, as discussed in Section 4.3.2.

In reality, when the momentum resolution of the setup is comparable with the nucleon's momentum, the observed momentum width is the convolution of these two contributions, i.e. the orbital angular momentum of the removed nucleon and the angular resolution of the setup. For unreacted[1] beam the width of this momentum distribution is defined only by the position resolution of the detectors and the straggling in the materials. For runs with empty target (E.T.) the measured angular resolution is $\sigma_{\text{E.T.}}$, while for runs with target (e.g. CH_2) the measured angular resolution (σ_{CH_2}) is

[1]The term unreacted beam here implies that the beam particles have only interacted with the target material at the atomic level (energy loss of the beam), or have been at most elastically scattered by the target nucleus (straggling of the beam).

larger due to the presence of the target material, see Section 4.3.2. Comparing runs with and without target for events of unreacted beam (Fig. 5.7), it is possible to estimate the straggling caused by the target material,

$$\sigma_{\text{Target}} = \sqrt{\sigma^2_{\text{CH}_2} - \sigma^2_{\text{E.T.}}} = \sqrt{65^2 - 57^2}\ \text{MeV/c} = 31\ \text{MeV/c}, \tag{5.1}$$

which is in good agreement with the ATIMA calculations. Thus, the background measurement obtained from runs without target needs to be folded with the extra straggling caused by the target material before subtracting it from the momentum distribution spectra obtained with the target. A typical example of background subtraction is shown in Fig. 5.8. Note also that the width of the momentum distributions of the reacted fragments presented in Section 5.2 is characterised by the root-mean-square (RMS) of the distribution.

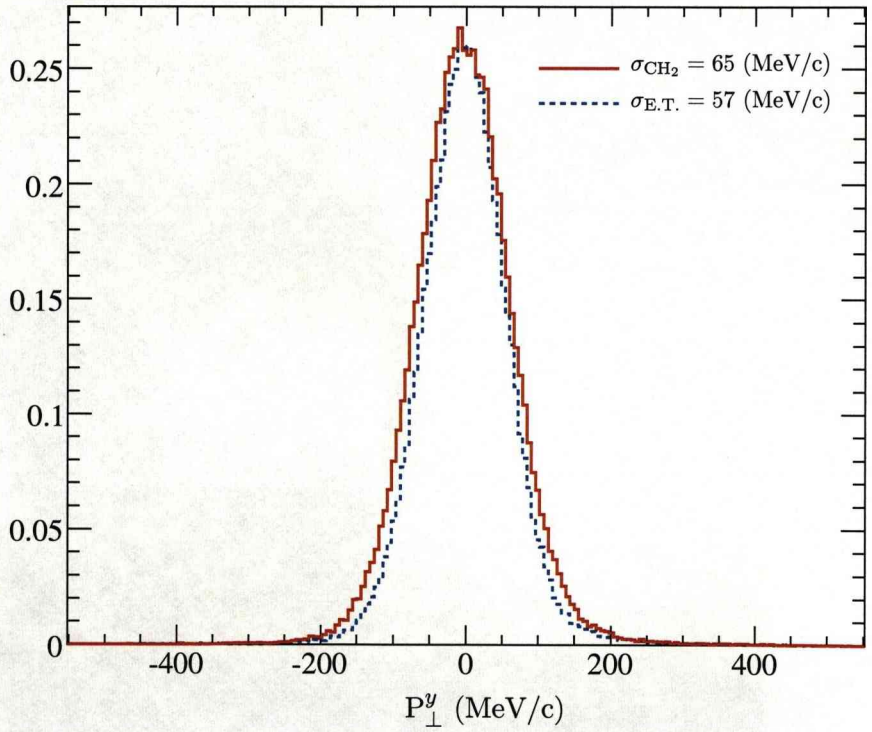

Figure 5.7: The projection of the transverse momentum distribution on the y axis is plotted for the unreacted beam and for the CH_2 (red-solid line) and empty (blue-dashed line) targets. The presence of the target causes an additional straggling of $\sqrt{65^2 - 57^2}$ MeV/c = 31 MeV/c.

5.1.4 Cross sections

The inclusive cross section (σ) is defined as the ratio of the total number (N_f) of a specific outgoing fragment (e.g. ^{56}Ni) to the total number (N_i) of a specific incoming

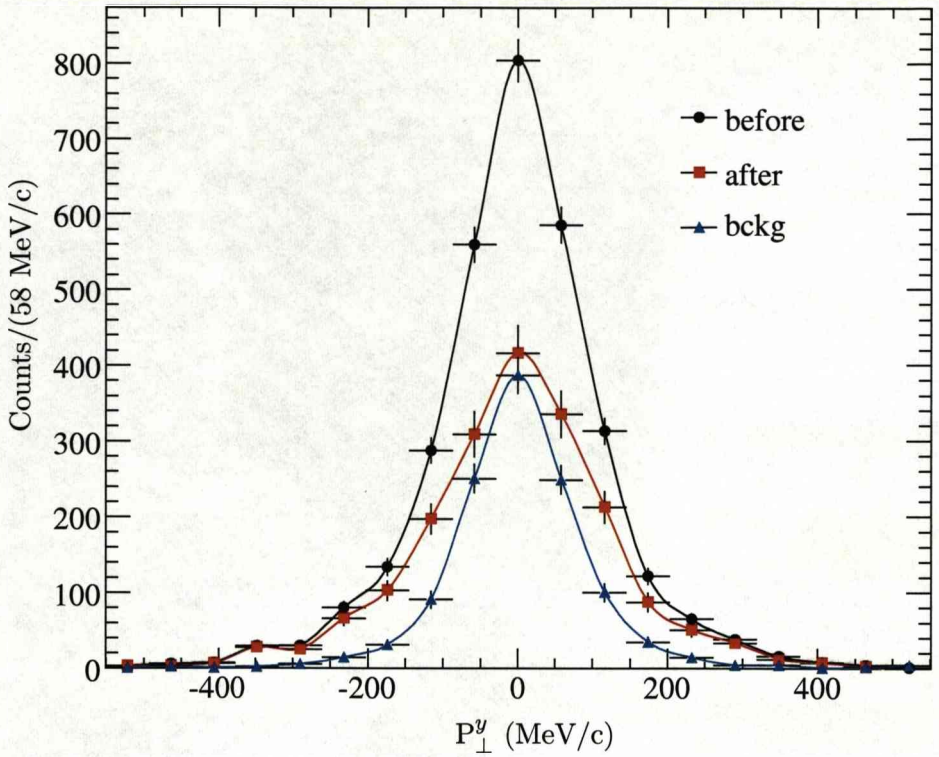

Figure 5.8: A typical example of a momentum distribution measurement before and after the subtraction of the background (bckg).

parent isotope (e.g. ^{57}Ni)

$$\sigma = \frac{N_f}{N_i}\frac{1}{N_t}, \tag{5.2}$$

where N_t is the number of target nuclei per unit area. The total number of incident ions (N_i) is determined as the number of nuclides (N_i') detected in the gate shown in Fig. 5.1 for the minimum bias trigger[2] (Tpat&1) times the down-scale factor (DSF) of this trigger. The nominal value of the down-scale factor is given from the hardware setting, e.g. for runs with ^{57}Ni it has the value of 2^8. Throughout the experiment, however, this factor can have a small deviation from the nominal value. It can be determined experimentally as the ratio of the number of events for a non down-scaled trigger to the number of events for which the non down-scaled trigger and the minimum bias are both present. For example, in the case of the non down-scaled (LAND) neutron trigger (Tpat&4), the down-scale factor of the minimum bias is determined as

$$DSF = \frac{N_{\text{Tpat\&4}}}{N_{\text{Tpat\&5}}} \approx 256. \tag{5.3}$$

[2]Minimum requirements for accepting an event, i.e. beam on target.

The number N_t is defined as the target number density times the target thickness in length units. However, the target thickness (d) is usually given in g/cm^2 units in which case the number N_t can be written in the more convenient form

$$N_t = \frac{d \cdot N_A}{m_u}, \tag{5.4}$$

where m_u is the mass number of the material in g and N_A is the Avogadro's number (6.022×10^{23} mol^{-1}). The number of the recorded fragments $N_f^{'}$ is a fraction of the total number of fragments N_f induced by the reaction, as it is affected by the detection and geometrical efficiency (ϵ) of the detectors involved, such that

$$N_f = \frac{N_f^{'}}{\epsilon}. \tag{5.5}$$

In the case of the minimum bias trigger, the efficiency factor (ϵ) is determined by the efficiency with which the heavy reaction fragment is detected and tracked, while if an additional trigger is required (e.g. LAND neutron trigger), the efficiency of the neutron detector is also taken into account. Using Eqs. 5.3, 5.4 and 5.5 the cross section from Eq. 5.2 can be rewritten as

$$\sigma = \frac{N_f^{'}}{N_i^{'} DSF} \frac{m_u}{\epsilon \cdot d \cdot N_A}. \tag{5.6}$$

5.2 Results

In this experiment both carbon (C, 187 mg/cm^2) and polyolefin (CH_2, 213 mg/cm^2) targets were used. In reactions with the carbon target mainly peripheral collisions are induced, removing a nucleon from the outer shells, while with the polyolefin target removal of more deeply bound nucleons is also expected due to the presence of hydrogen atoms in the target. The reaction mechanism is also expected to differ between the two targets with the former one inducing mainly one-nucleon removal reactions, while the latter one enhances quasi-free scattering reactions (p,pn) and (p,2p). A comparison between these two types of reactions is presented in Chapter 2. The significant influence that the hydrogen atoms have in the reactions is already evident in the multiplicity plot of the CV detector, illustrated in Fig. 5.9, for ^{56}Ni and ^{56}Co heavy outgoing fragments and for different targets.

Once a reaction channel is clearly selected, it is possible to measure the cross section for this process and the transverse momentum distributions of the projectile-like fragments, which provide a signature of the orbital angular momentum of the knocked-out nucleon. The results for the cross sections and the momentum distributions presented in this thesis are inclusive, in the sense that the knocked-out nucleon could originate from any state in the nucleus, leaving the residue to an excited state or the ground

state. In order to distinguish contributions from the different final states, coincident γ-ray measurement is also required. The values for the cross sections presented in this chapter are tentative, since a more precise estimation of the detectors' efficiency using simulations is required, and their error is not assigned yet.

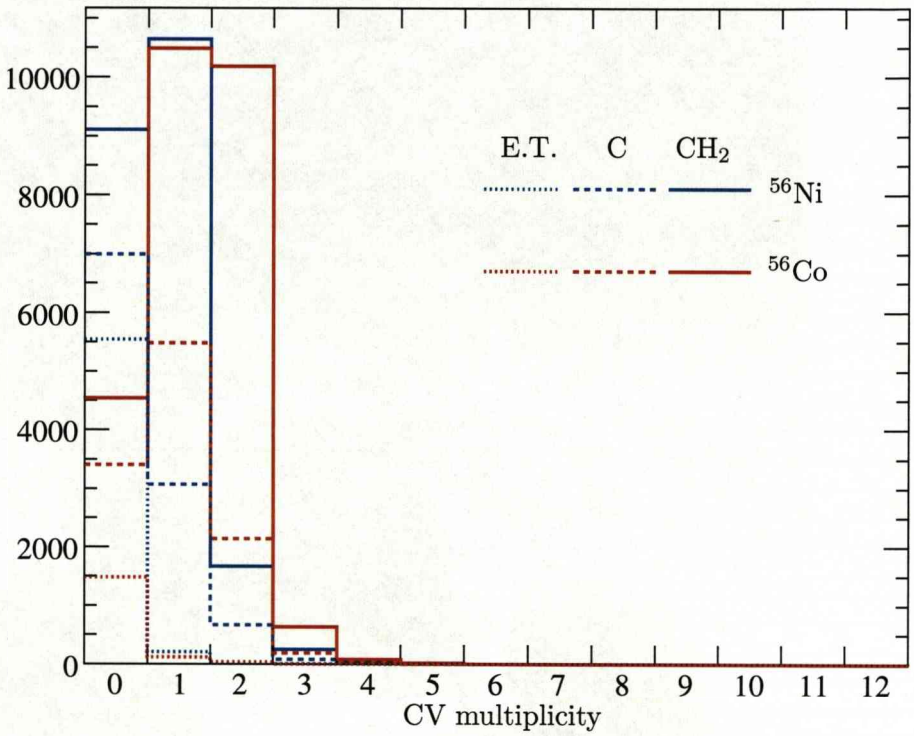

Figure 5.9: The multiplicity of the plastic detector (CV) obtained for ^{56}Co (red lines) and ^{56}Ni (blue lines) heavy outgoing fragments and for CH_2 (solid lines), C (dashed lines) and empty (dotted lines) targets. The runs from the three different targets have been normalised to the same number of incoming ^{57}Ni particles.

5.2.1 C target

The total cross section for removing one nucleon from ^{57}Ni by a C target is the sum of two main contributions, the stripping and the diffractive breakup, see Section 2.3.1. In most experiments it is impossible to determine experimentally the contribution of each one separately, especially if the removed nucleon is a neutron. However, in the present experiment neutrons which are evaporated in-flight (i.e. diffractive case) are kinematically forward focused and can be detected with the LAND detector, located $\sim$ 15 m downstream from the target, with very high efficiency. In addition, neutrons removed via the stripping process are emitted in large angles[3] and are registered in

[3]To which extent the scattered nucleons originating from the stripping process react with or get absorbed by the target is unclear.

the CsI array which surrounds the target area. It is evident that the LAND/ALADIN setup provides a unique opportunity to study experimentally the contribution of these two processes to the total cross section of the reaction.

One-neutron removal from ^{57}Ni

The inclusive cross section for the C(^{57}Ni,^{56}Ni)X reaction, when one neutron is detected by the LAND detector (i.e. diffractive breakup case), is measured to be 4.0 mb. For the determination of this cross section a detection efficiency of 80% has been assumed for detecting one neutron in the LAND detector. The main sources of error in the cross section measurement are the detection efficiencies and the estimation of the background from the runs without target. The y projection of the transverse momentum distribution of the residual ^{56}Ni core after the diffraction breakup of one neutron from ^{57}Ni is illustrated in Fig. 5.10. In the same figure the theoretical distributions for $l = 1$ and $l = 3$ [73, 74] are also shown for comparison.

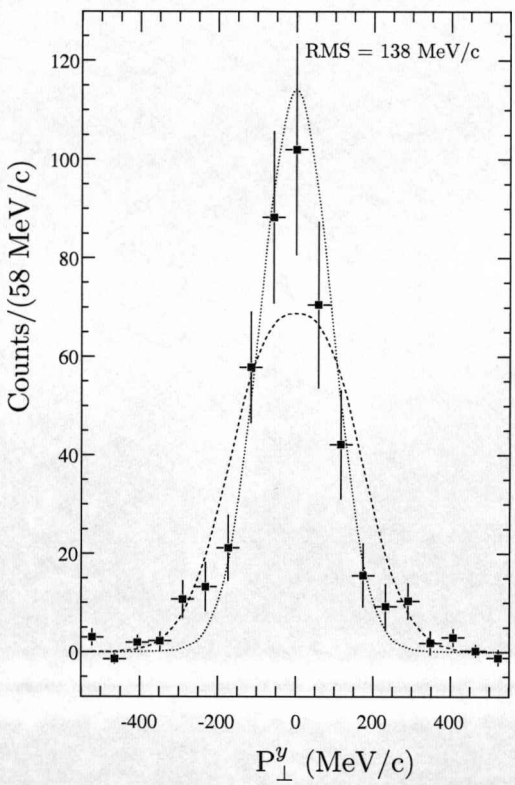

Figure 5.10: The projection of the transverse momentum distribution on the y axis is plotted for the ^{56}Ni core after the removal of one neutron from ^{57}Ni by the C target. The additional requirement that a neutron has been detected by the LAND detector is applied, selecting in this way only the neutron diffractive breakup channel. Calculations [73, 74] for $l = 1$ (dotted line) and $l = 3$ (dashed line) are also shown for comparison.

One-proton removal from ^{57}Ni

The inclusive cross section for removing one proton from ^{57}Ni by the C target with the requirement that a proton has triggered the CV detector is measured to be 22.5 mb. For the determination of this cross section a detection efficiency of 80% has been assumed for detecting a scattered proton in the CV detector. The y projection of the transverse momentum distribution of the residual ^{56}Co core after the removal of one proton from ^{57}Ni is illustrated in Fig. 5.11, where the theoretical distributions for $l = 1$ and $l = 3$ [73, 74] are also shown for comparison.

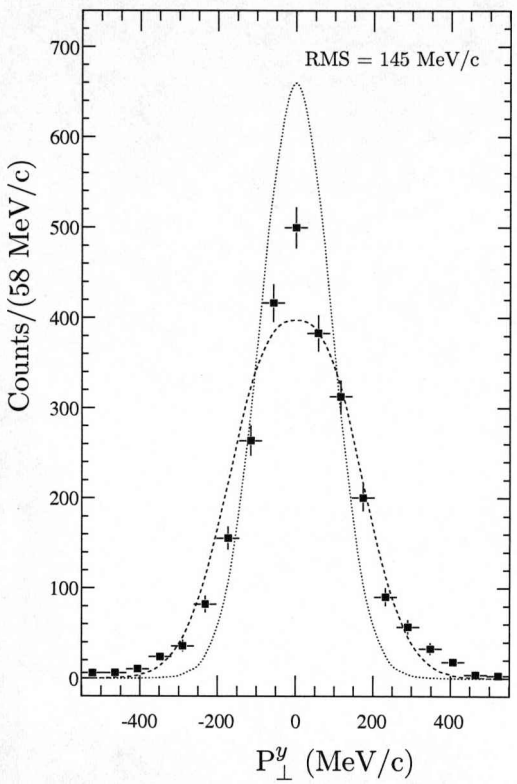

Figure 5.11: The projection of the transverse momentum distribution on the y axis is plotted for the ^{56}Co core after the removal of one proton from ^{57}Ni by the C target. The additional requirement that a proton has been detected by the CV detector is applied. Calculations [73, 74] for $l = 1$ (dotted line) and $l = 3$ (dashed line) are also shown for comparison.

5.2.2 CH_2 target

In the case of the CH_2 target both the carbon and the hydrogen atoms contribute to the final measurement, but as mentioned in Section 5.1.2 the carbon contribution can be subtracted as background from the spectra, allowing the study of reactions induced

only by the hydrogen atoms[4]. In this section all correlation plots are presented for both C and H_2 targets in order to highlight their differences.

At the beam energies used in the present experiment (i.e. $\sim$ 500 MeV/nucleon), it is expected that the proton of the hydrogen atom can knock a nucleon out of the projectile nucleus without any further violent interaction to occur between the nucleus and the incident or the two outgoing particles, due to the low nucleon-nucleon cross section in this energy region (see Section 2.3.2). In other words, a quasi-free scattering reaction ((p,pn) and (p,2p)) is likely to occur, but in inverse kinematics. Some evidence of such reactions in inverse kinematics are presented in the following sections.

One-neutron knockout from ^{57}Ni

In particular, when requiring the ^{56}Ni outgoing fragments, it is possible that the hydrogen atoms in the CH_2 target have induced a (p,pn) quasi-free reaction with the projectile, in which both the proton from the target and the neutron from the projectile should scatter at large angles, sharing the energy of the incident neutron of the projectile which is $\sim$ 500 MeV. The proton passes through the CV detector producing a trigger signal and then penetrates or stops in the CsI array producing a high energy signal in one or a few neighbouring crystals. The neutron, although being invisible for the CV detector, it is expected to scatter in the dense CsI material and generate relatively large energy signals. Requiring one proton in one of the plastic paddles of the CV detector, the multiplicity of the CsI crystals is shown in Fig. 5.12 with blue solid line.

The high number of multiplicity-one events in the CsI multiplicity plot, with the requirement that a proton has triggered the CV detector, correspond mainly to protons that penetrate a thin plastic paddle of the CV detector and then enter one of the CsI crystals located at the same ϕ angle. By plotting the ϕ angle obtained from the CV and CsI detectors (Fig. 5.13), this effect appears as a strong correlation on the diagonal.

Performing the same correlation plot for the events where the CsI multiplicity is two (in Fig. 5.12 with a solid blue line), it is expected to see protons which have scattered in two neighbouring CsI crystals[5] after triggering one paddle of the CV detector. Indeed such events appear strongly correlated on and around the diagonal of Fig. 5.14. However, on the same figure it is evident that a strong correlation appears also for crystals with a ϕ angle opposite to that given from the plastic paddles. Thus, the events with multiplicity two in the CsI array and the requirement for one proton in the CV detector, besides being scattered protons in neighbouring CsI crystals, can also have a different origin. This correlation at opposite ϕ angles is a signature of the neutron

[4]The plots obtained with the CH_2 target in which the carbon contribution has been subtracted are labelled as "H_2 Target", although a pure H_2 target has not been used in the present experiment.

[5]It should be noted here that if an add-back procedure is included in the analysis of the CsI array, such cases of particles scattering in neighbouring crystals will be merged and treated as one hit.

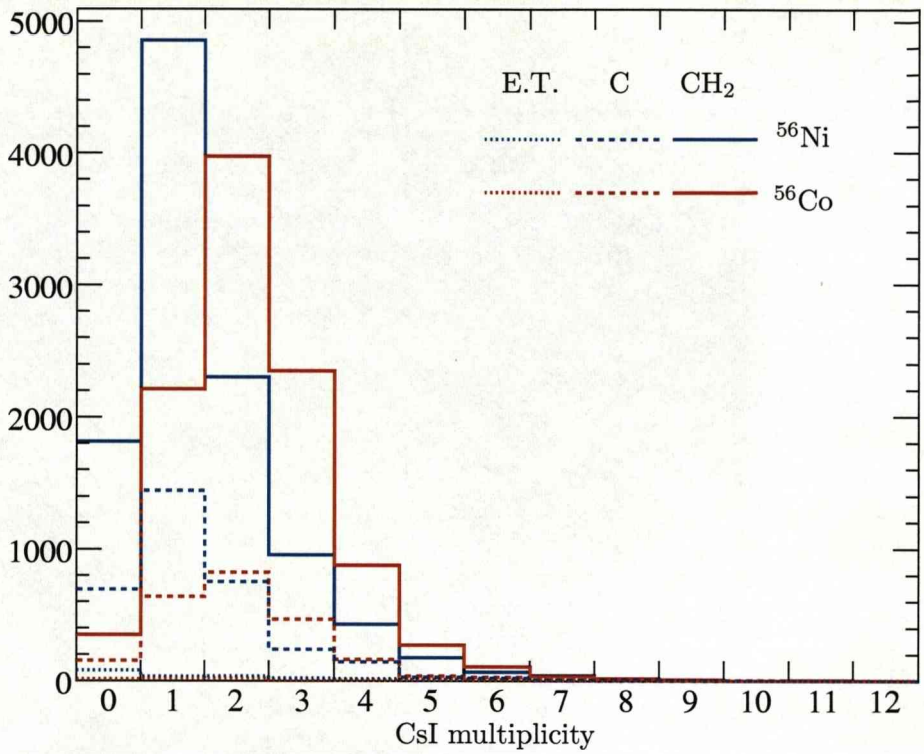

Figure 5.12: The multiplicity of the CsI crystals by selecting the ^{56}Ni (blue lines) and the ^{56}Co (red lines) heavy outgoing fragments when requiring the multiplicity of the CV detector to be one and two, respectively. The runs from the three different targets have been normalised to the same number of incoming ^{57}Ni particles.

and proton from the (p,pn) reaction. In other words, the proton triggers a plastic paddle and enters one of the CsI crystals placed at the same ϕ angle (points on and around the diagonal in Fig. 5.14), while the neutron does not get detected by the thin plastic paddles of the CV detector but it triggers a CsI crystal placed at the opposite ϕ angle compared to the ϕ angle where the proton is detected. The origin of events with multiplicity two in the CsI is also evident in Fig. 5.15, in which scattered particles have ΔCsi (ϕ) = 1 and/or ΔCsi (θ) = 1 and particles at opposite ϕ angles have ΔCsi (ϕ) = 5 or 6. The transverse momentum distribution versus the ϕ angle between the scattered proton and neutron is shown in Fig. 5.16. In Fig. 5.17 the y projection of the transverse momentum distribution is shown for proton and neutron scattered at any ϕ angle (left) and at $\phi = 180°$ (ΔCsi (ϕ) = 6) (right).

One-proton knockout from ^{57}Ni

By selecting the ^{56}Co outgoing fragments it is expected that the hydrogen atoms in the CH_2 target can induce a (p,2p) quasi-free reaction with the projectile. Both protons,

from the target and from the projectile, should scatter at large angles sharing the energy of the incident proton $\sim$ 500 MeV. Furthermore, the two protons should be detected by both the CV and the CsI detectors around the target. Thus, in the multiplicity plot of the CV detector a high number of multiplicity two events is expected, as shown in Fig. 5.9.

By correlating the CV detector number of the first and the second hit, see Fig. 5.18, it is evident that in most cases the two protons are detected by scintillators placed at opposite ϕ angles, i.e. $\phi \approx 180\,^\circ$. Thus, the two outgoing protons are preferentially moving on the same plane or almost on the same plane; the ϕ angular resolution in the present experiment limits the measurement to $180\,^\circ \pm 15\,^\circ$. It is interesting to plot the transverse momentum distribution of the ^{56}Co core after the knockout of one proton from ^{57}Ni as a function of the ϕ angle between the two outgoing protons, as shown in Fig. 5.19. In this figure it is evident that for outgoing protons scattered at opposite ϕ angles (ΔCvi = 6) the large components of the momentum distribution of the fragment are suppressed. The y projection of the transverse momentum distribution is shown in Fig. 5.20 for any ϕ angle (left) between the two scattered protons and for a ϕ angle around $180\,^\circ$ (right).

Furthermore, by selecting the events where the two outgoing protons are detected by plastic paddles placed at opposite ϕ angles, it is possible to measure their polar angle θ from the orientation of the CsI crystals, as shown in Fig. 5.21. The θ angle between the two protons peaks at $77\,^\circ$. The angular resolution for measuring the θ angle is defined by the opening angle of the crystals which is $\sim 6\,^\circ$.

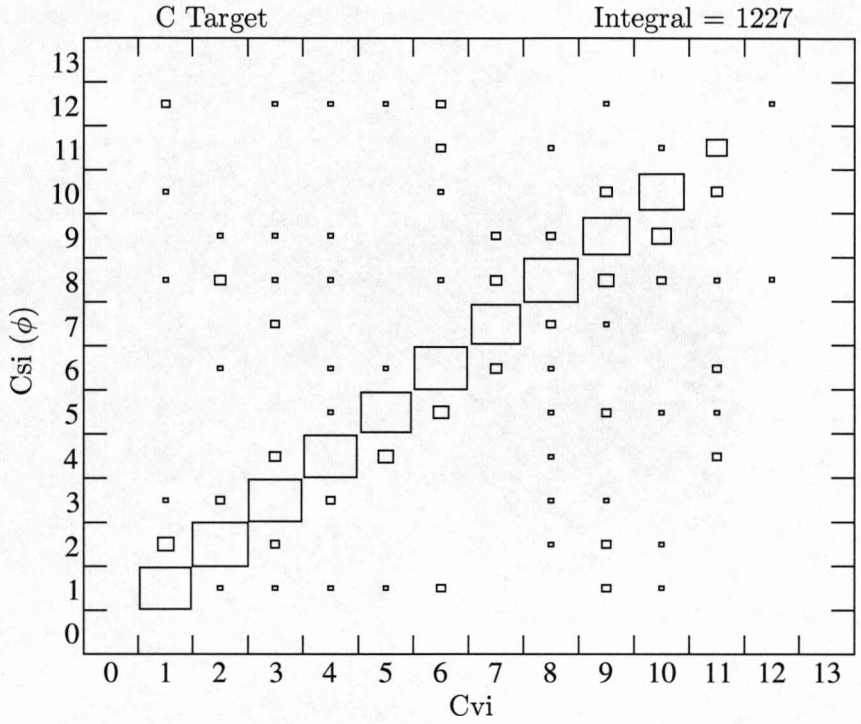

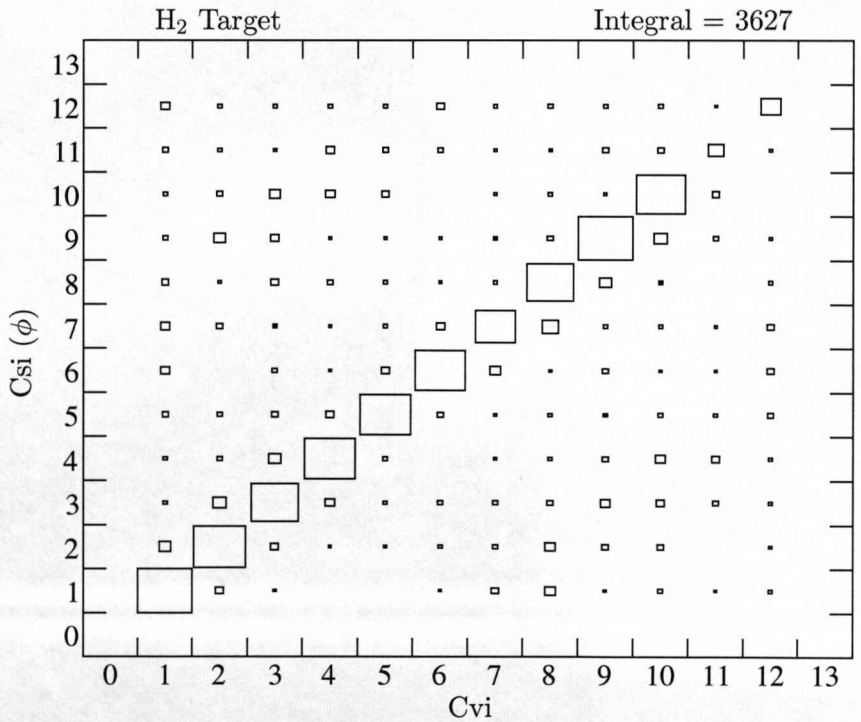

Figure 5.13: The paddle number of the plastic CV detector (Cvi), which is related to the ϕ angle, is plotted versus the ϕ crystal number of the CsI array (Csi (ϕ)) for events where both the CV and the CsI detectors have multiplicity one. A strong correlation on the diagonal is evident, which corresponds to protons that hit a plastic paddle and then enter one of the CsI crystals located at the same ϕ angle "behind" the plastic paddle.

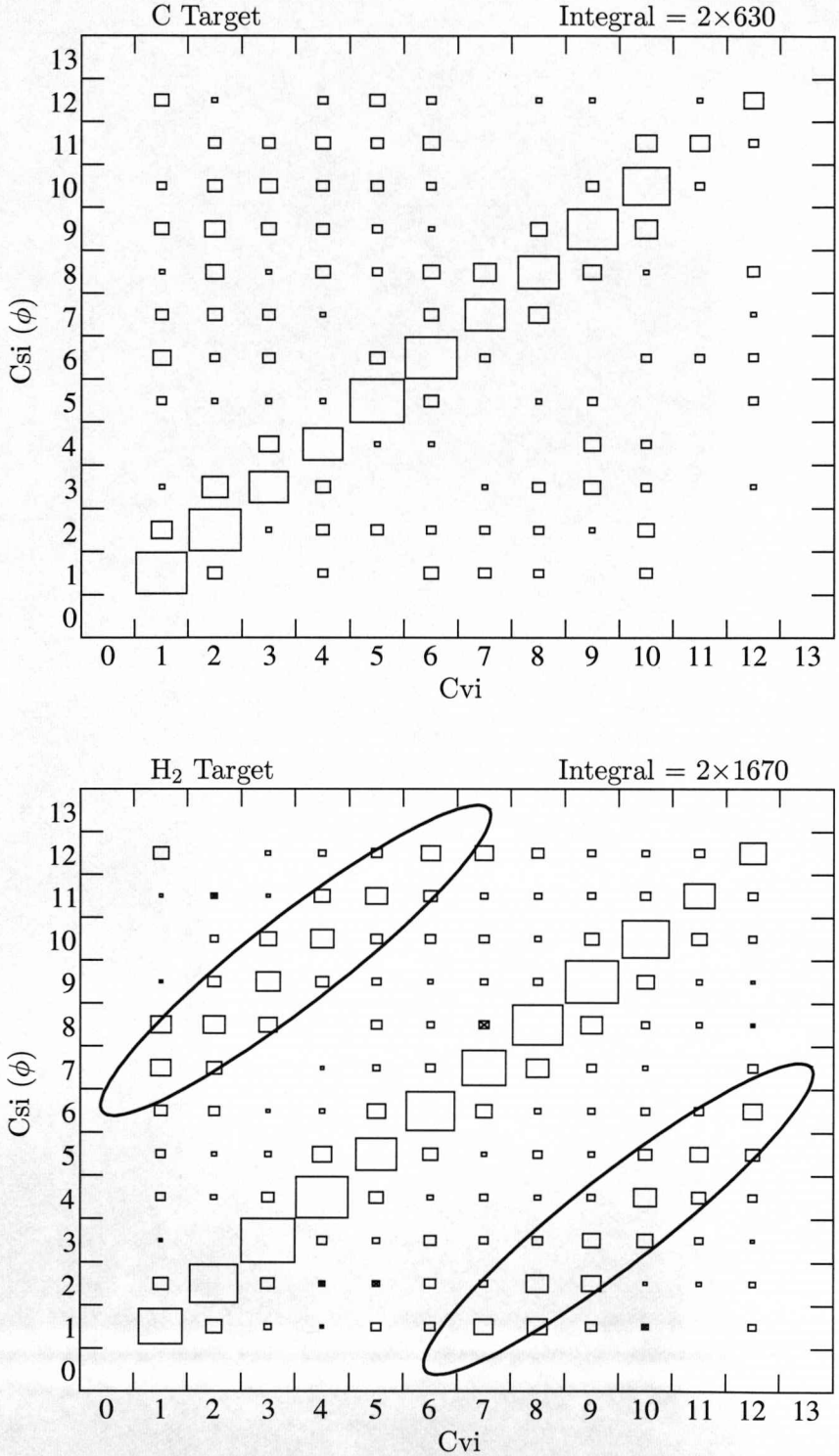

Figure 5.14: Correlation plot as in Fig. 5.13, but for events where the multiplicity of the CV and CsI detectors is one and two, respectively. The strong correlation on the diagonal corresponds to protons that hit a plastic paddle and then scatter in neighbouring CsI crystals located at the same ϕ angle "behind" this paddle. The highlighted correlation, for ϕ angles from the CsI array opposite to those obtained from the CV detector, corresponds to neutrons from the (p,pn) reaction.

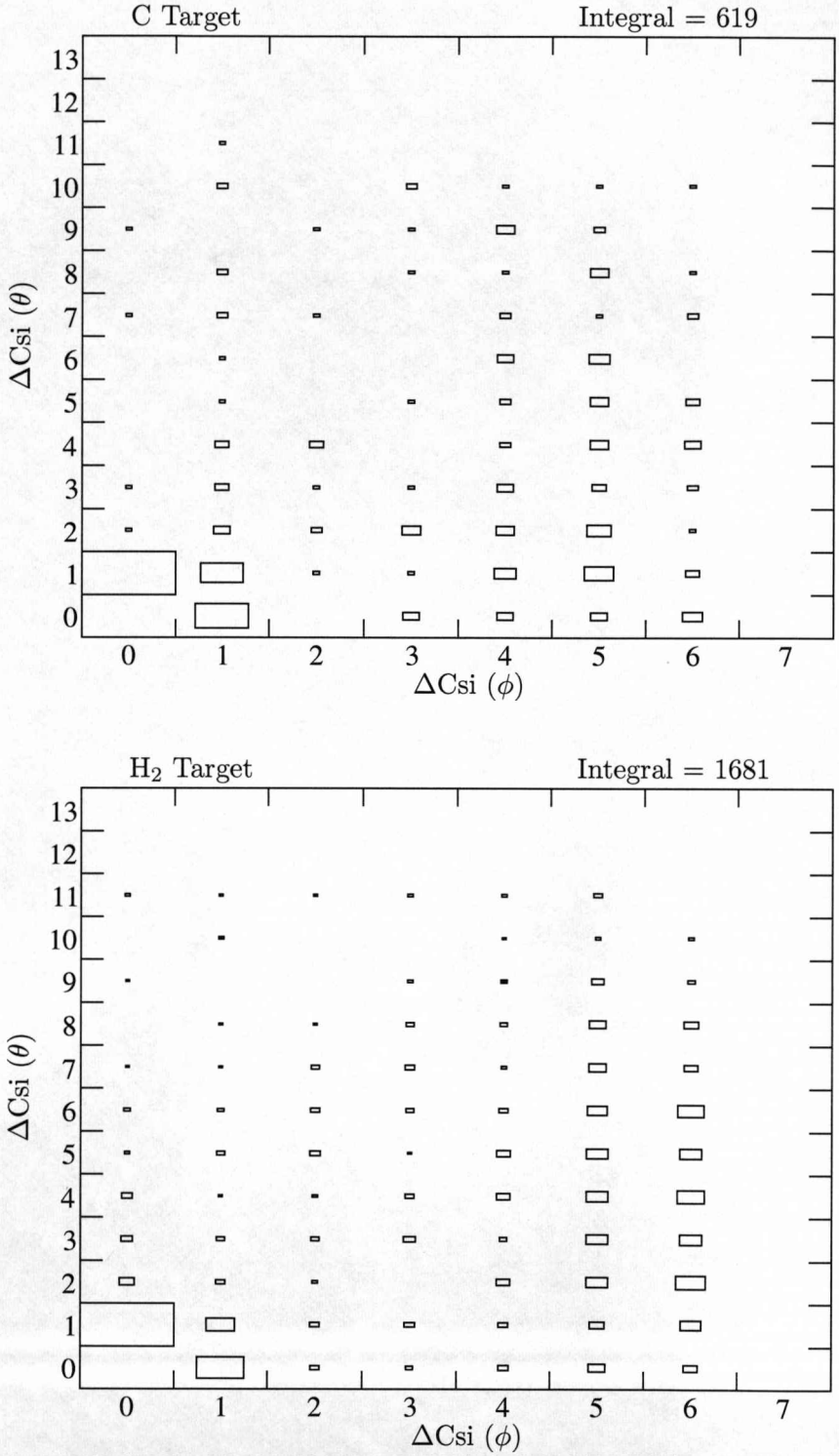

Figure 5.15: The difference between the θ crystal number of the first and the second hit versus the difference of the ϕ crystal number for these hits, for multiplicity two in the CsI array and one in the plastic detector (CV) and ^{56}Ni outgoing fragments. The events with ΔCsi (ϕ) = 1 and/or ΔCsi (θ) = 1 correspond to particles which have scattered in neighbouring crystals, while events with ΔCsi (ϕ) = 5 or 6 correspond to particles detected by crystals at opposite ϕ angles.

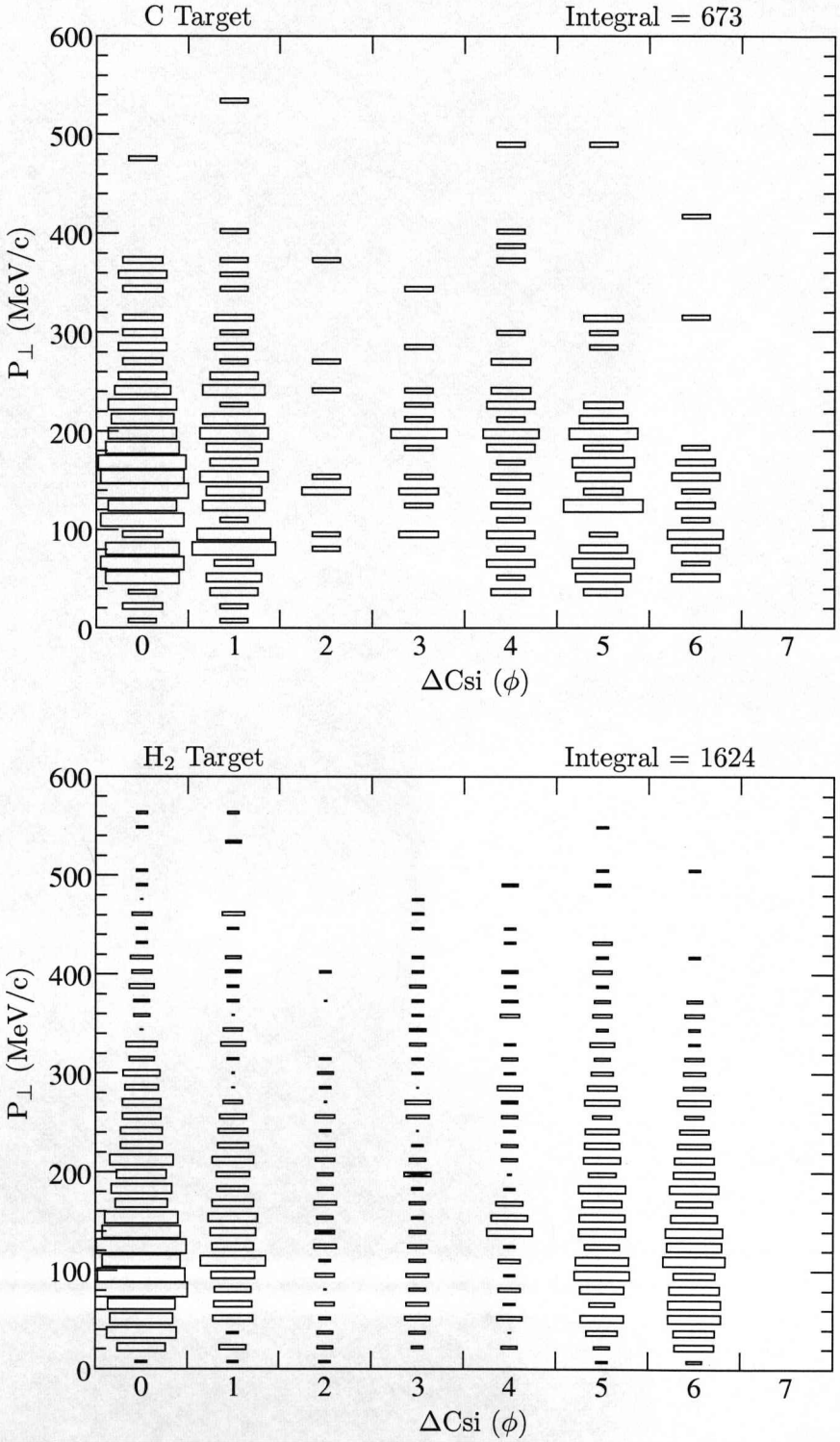

Figure 5.16: The transverse momentum distribution of the ^{56}Ni core after the knockout of one neutron from ^{57}Ni is plotted versus the ϕ angle between the proton and the neutron for the C (top) and H_2 (bottom) targets.

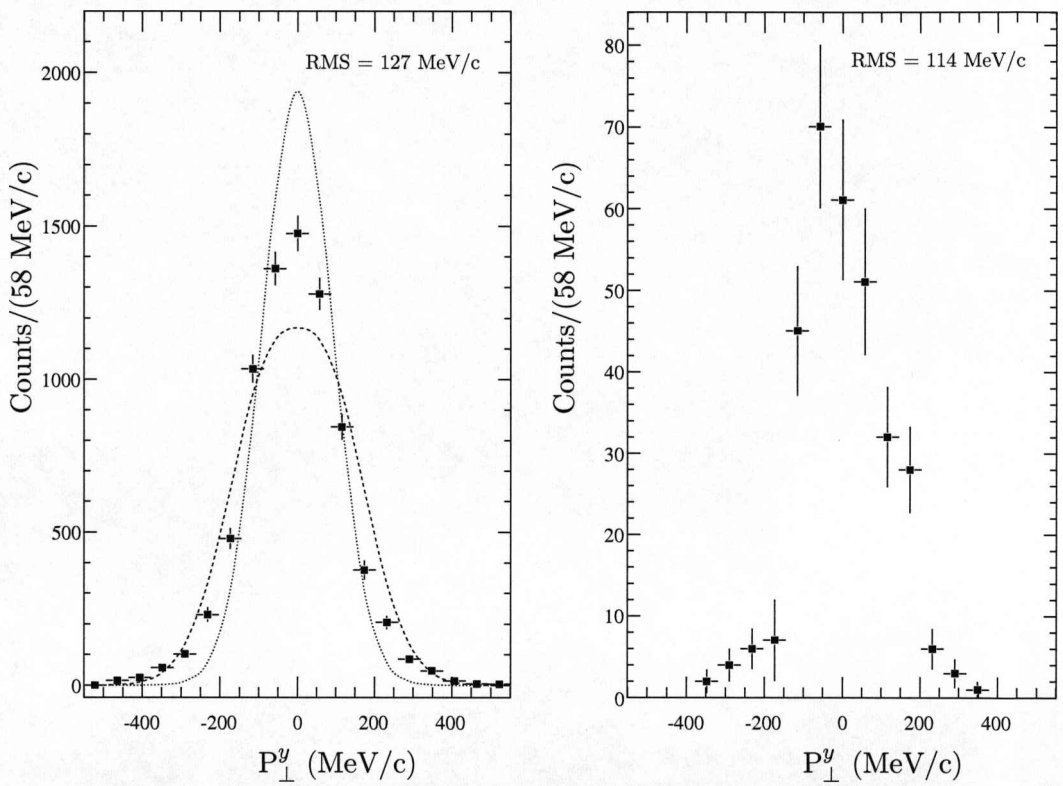

Figure 5.17: The projection of the transverse momentum distribution on the y axis is plotted for the ^{56}Ni core after the knockout of one neutron from ^{57}Ni by the H_2 target for any ϕ angle between the proton and the neutron (left) and for a ϕ angle around 180° (right). Calculations for $l = 1$ (dotted line) and $l = 3$ (dashed line) are also shown for comparison. Note that these calculations are obtained for C target.

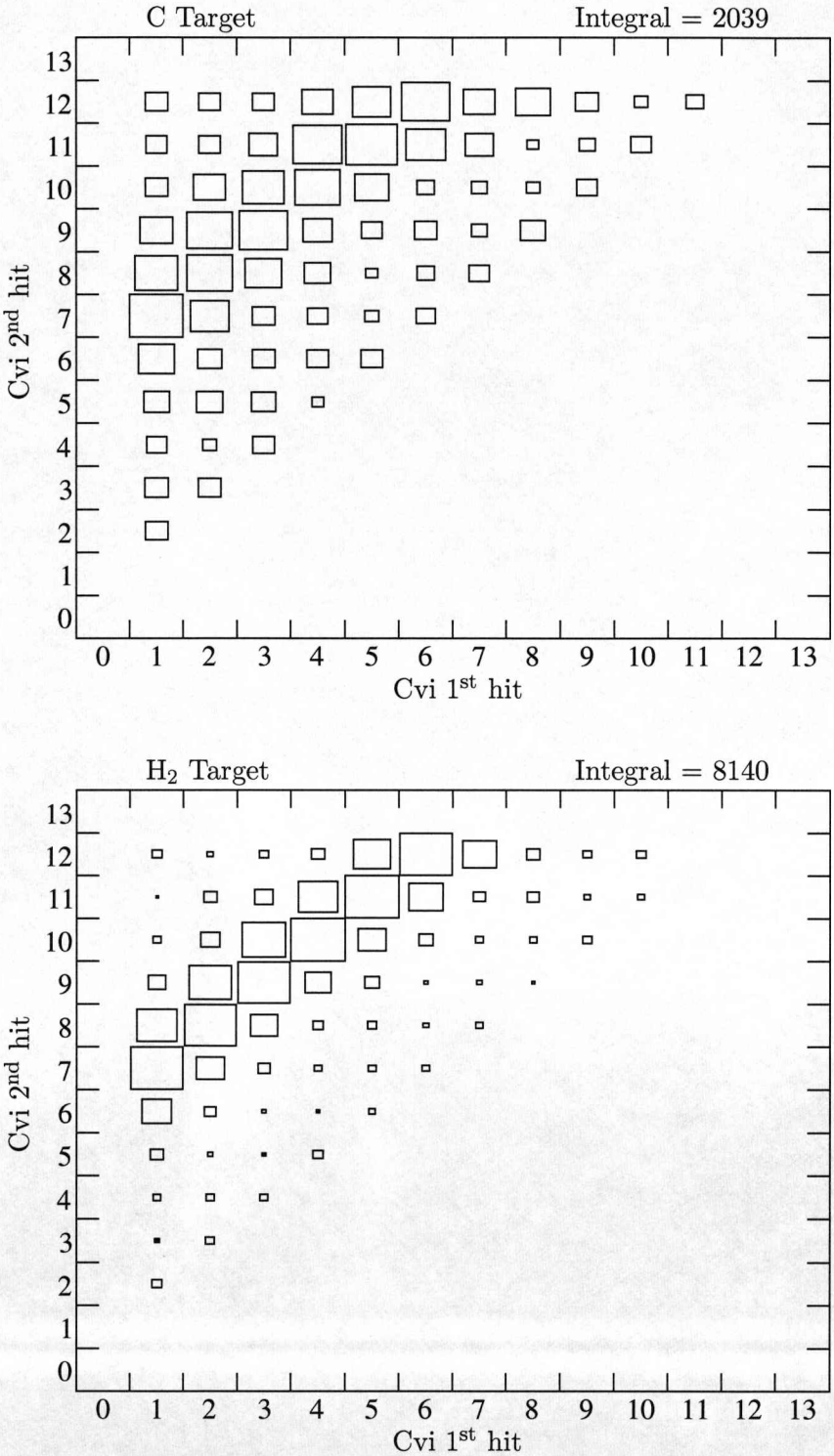

Figure 5.18: The paddle number of the plastic CV detector (Cvi) for the first (1^{st}) and the second (2^{nd}) hit corresponding to the two protons originating from the p(^{57}Ni,^{56}Co)2p knockout (quasi-free) reaction is plotted for the C (top) and H_2 (bottom) targets. It is evident that the two protons are preferentially scattered at opposite ϕ angles ΔCvi $\approx$ 6 (180 °).

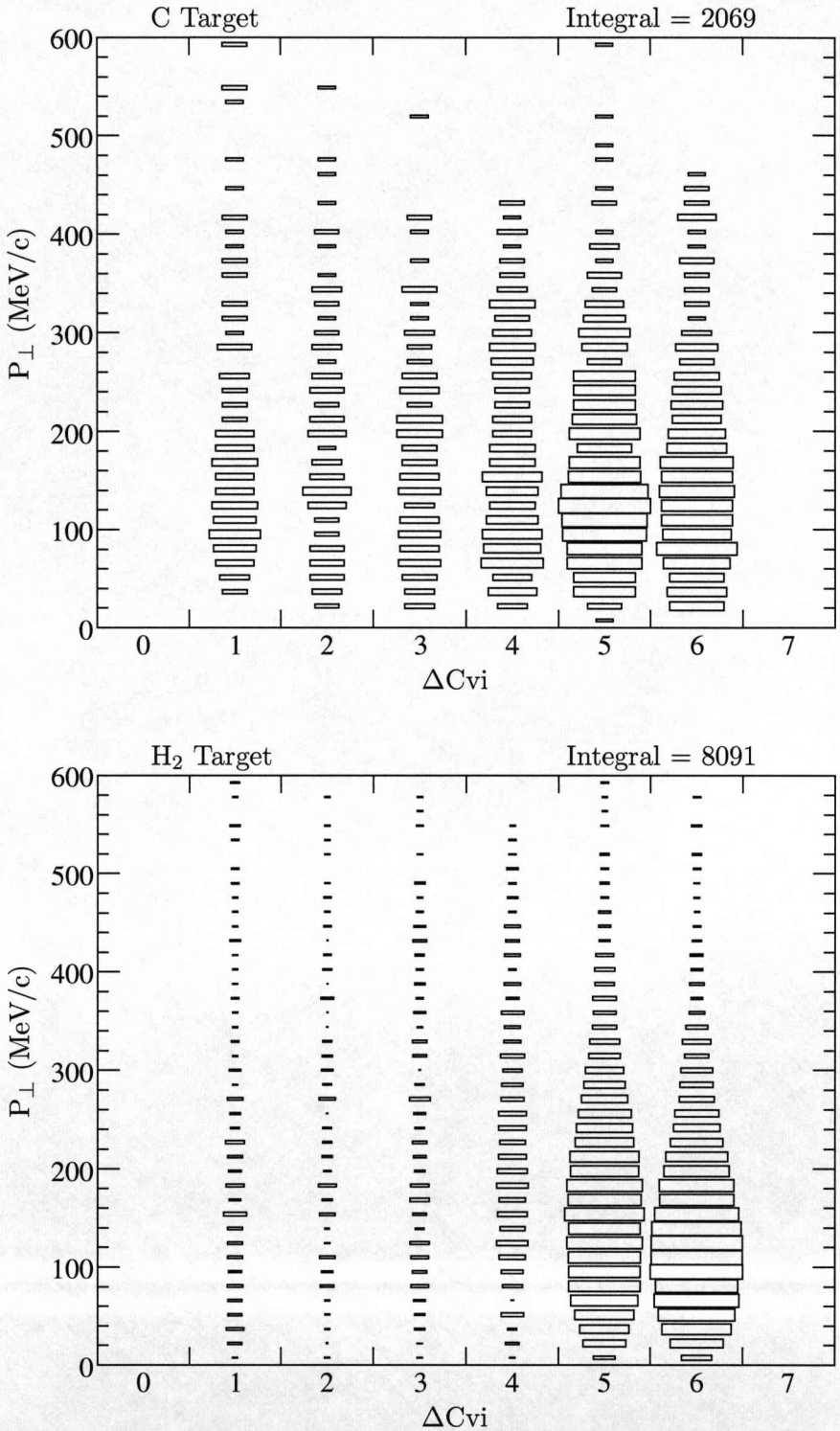

Figure 5.19: The transverse momentum distribution of the ^{56}Co core after the knockout of one proton from ^{57}Ni is plotted versus the ϕ angle between the two protons for the C (top) and H_2 (bottom) targets.

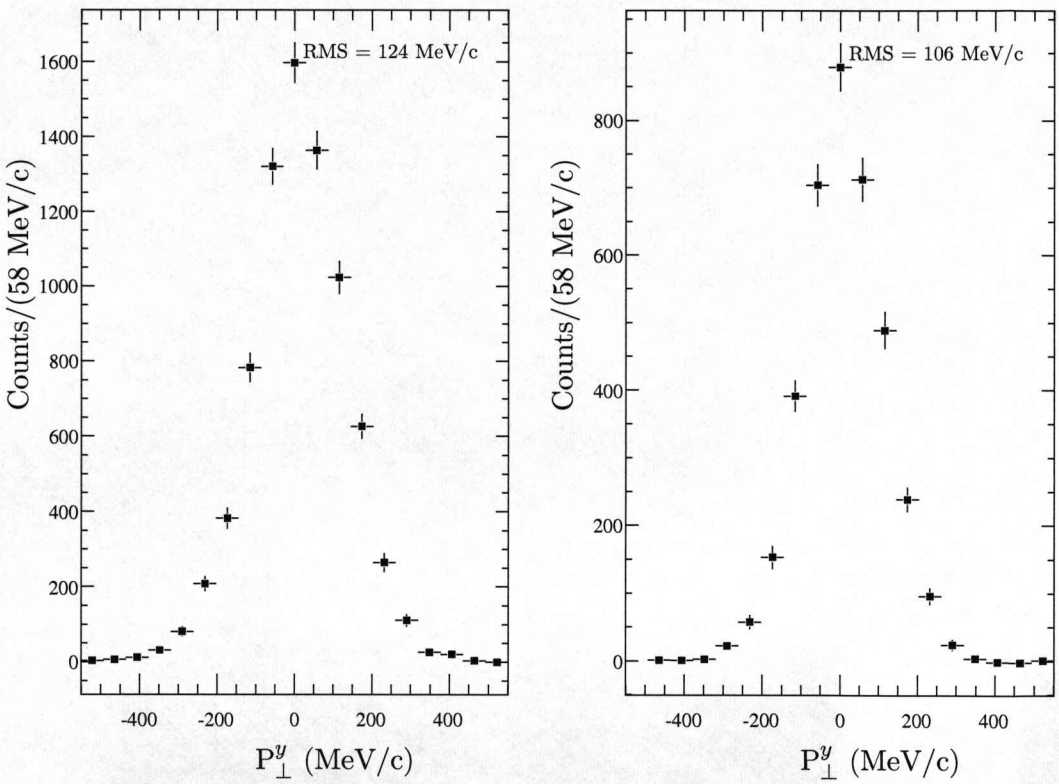

Figure 5.20: The projection of the transverse momentum distribution on the y axis is plotted for the ^{56}Co core after the knockout of one proton from ^{57}Ni by the H_2 target, requiring two protons in the plastic detector (CV) with any ϕ angle between them (left) and with a ϕ angle around 180 ° (right).

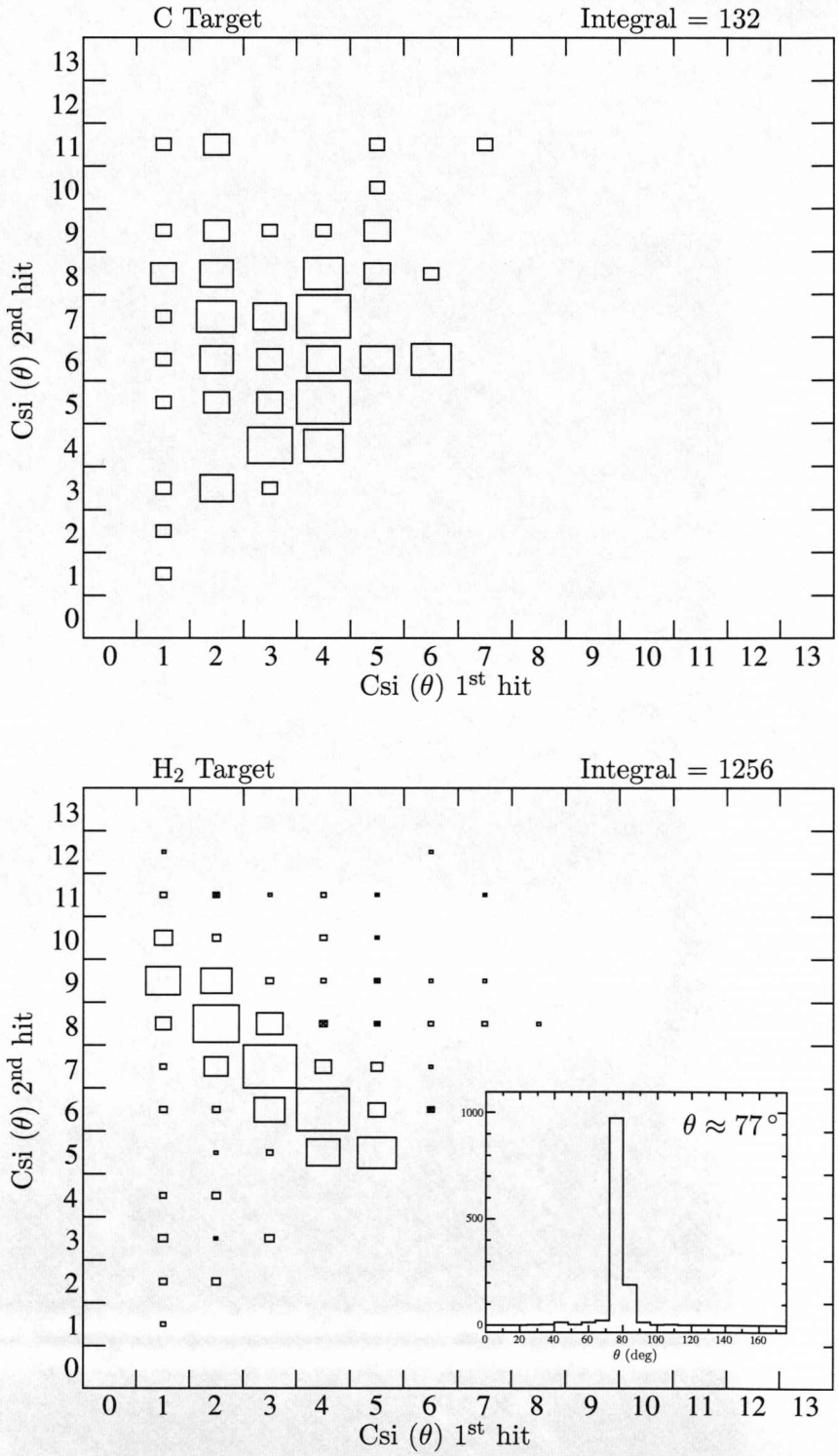

Figure 5.21: The θ crystal number of each of the two outgoing protons when scattered at opposite ϕ angles for the C (top) and H_2 (bottom) targets. The strong correlation is evidence of the quasi-free nature of the scattering. The angle between the momentum vectors of the two protons peaks at 77°. For the free nucleon-nucleon scattering at kinetic energies of $\sim$ 500 MeV the angle between the two nucleons is $\sim$ 83°.

5.3 Discussion

One-nucleon removal reactions from ^{57}Ni

The shell model predicts that in ^{57}Ni the valence neutron is in the $2p_{3/2}$ orbital, thus by removing this neutron via (peripheral) one-neutron removal reactions it is expected to populate the residue ^{56}Ni in the ground state with a momentum distribution associated with an $l = 1$ state. Furthermore, more deeply bound neutrons are predicted to be in the $1f_{7/2}$ shell. When removing one of these neutrons it is expected to populate the ^{56}Ni fragment in one of its low excited states and its momentum distribution to follow an $l = 3$ distribution. These predictions have been confirmed in a recent experimental study [18] using one-neutron removal reactions. In the same study, reduced spectroscopic factors for the p- and f-shell neutrons compared to shell model calculations were observed. From the preliminary results on the one-neutron removal reaction from ^{57}Ni presented in this chapter, it is possible to measure only the inclusive momentum distribution from all final states of the ^{56}Ni fragment for the diffraction breakup channel, as shown in Fig. 5.10. The inclusive momentum distribution has indeed contributions from both $l = 1$ and $l = 3$ components.

Regarding the one-proton removal reaction C(^{57}Ni,^{56}Co)X, the shell model predicts that the valence protons in ^{57}Ni are in the closed f shell and thus removing one via (peripheral) one-proton removal reactions should result in a momentum distribution of the ^{56}Co residue fragments associated with an $l = 3$ state. From the preliminary results on the one-proton removal reaction from ^{57}Ni presented in this chapter, the inclusive momentum distribution of the ^{56}Co fragments is measured to be broader than that for removing a neutron, as shown in Fig. 5.11. However, a pure $l = 3$ distribution is not observed.

Quasi-free scattering kinematics

As discussed in Ref. [75] by L. V. Chulkov *et al.*, in a quasi-free scattering reaction in inverse kinematics the recoiling and the knocked-out particles should be strongly correlated. The statements in Ref. [75] hold true for knocking out a cluster from a light nucleus by a proton target. However, the same arguments can be used for the (p,2p) and the (p,pn) quasi-free scattering reactions discussed here. In the present text the nucleon which is knocked out from the projectile takes the place of the cluster in the equations of Ref. [75], while the scattered proton from the target is common in both cases. For the (p,2p) reaction a differentiation between the proton from the target and the proton from the projectile is not possible. Thus, for simplicity in the notation, the equations are written for the (p,pn) reaction.

An equivalent formalism as the one used in Ref. [75] is defined here. The nucleus is travelling with momentum $\vec{P}$ and $\vec{Q}$ before and after the reaction, respectively. $\vec{p}_{\mathrm{p}}$

is the initial momentum of the proton in the target, while $\vec{q}_{\rm p}$ and $\vec{q}_{\rm n}$ are the momenta of the scattered proton and neutron, respectively. The reaction plane is defined by the $\vec{P}$ and $\vec{q}_{\rm p}$ vectors, as shown in Fig. 5.22, while the z axis of the Cartesian coordinate system is defined along the $\vec{P}$ vector. The angle between a vector perpendicular to the reaction plane (i.e. parallel to $\vec{P} \times \vec{q}_{\rm p}$) and $\vec{q}_{\rm n}$ is ψ. The azimuthal angles are measured from the x axis. The kinematics of the quasi-free scattering in the laboratory system ($|\vec{p}_{\rm p}| = 0$) are summarised in the following equation [75]

$$\cos\psi = \frac{((\vec{P} \times \vec{q}_{\rm p}) \cdot \vec{q}_{\rm n})}{|\vec{P} \times \vec{q}_{\rm p}||\vec{q}_{\rm n}|} = \sin\theta_{\rm n} \sin(\phi_{\rm n} - \phi_{\rm p}) = \frac{Q_{\rm tr}}{|\vec{q}_{\rm n}|}, \tag{5.7}$$

where $Q_{\rm tr}$ is the projection of the momentum $\vec{Q}$ on the $\vec{P} \times \vec{q}_{\rm p}$ vector, i.e. perpendicular to the reaction plane, and is related to the internal momentum of the knocked-out nucleon (while in the nucleus). The first equality is simply derived by carrying out the dot- and cross-product calculations for the $\vec{q}_{\rm n}$, $\vec{q}_{\rm p}$ and $\vec{P}$ vectors. The second equality holds from geometrical arguments. To derive the last equality, momentum conservation in the reaction is used ($\vec{q}_{\rm n} + \vec{q}_{\rm p} = \vec{P} - \vec{Q}$).

Unfortunately, the magnitude of $\vec{q}_{\rm n}$ (or $\vec{q}_{\rm p}$) is not measured in the present experiment, since it requires a measurement of the total energy of the nucleon using a calorimeter. However, even a qualitative description using the range of expected values for $\vec{q}_{\rm n}$ can give some kinematical restrictions. As mentioned earlier in this chapter, the scattered nucleons share the energy of the incident particle, i.e. they share $\sim$ 500 MeV. Thus, it is likely that each scattered nucleon has an energy in the region of 100 - 400 MeV. This kinetic-energy range corresponds to nucleons moving with momentum 450 - 950 MeV/c, while the projection of the momentum change ($Q_{\rm tr}$) of the projectile-like fragment, which corresponds to the momentum of the knocked-out nucleon in the nucleus, has a value of $\sim$ 100 MeV/c. Using these values for $|\vec{q}_{\rm n}|$ and $Q_{\rm tr}$ in Eq. 5.7, the value of the $\cos\psi$ lies around 0.1 - 0.2 or else $\psi \simeq 75\,^\circ$ - $85\,^\circ$. In other words the knocked-out neutron is more likely to scatter "close" to the reaction plane, where $\psi = 90\,^\circ$ by definition.

Moreover, the last equality of Eq. 5.7 shows the dependency of the momentum $Q_{\rm tr}$ on the difference in the azimuthal angles of the two scattered nucleons ($\phi_{\rm n} - \phi_{\rm p}$). This correlation is evident from the data as illustrated in Figs. 5.16 and 5.19, which shows indeed that when moving towards co-planar scattering ΔCsi (ϕ) = 6 or ΔCvi = 6 (i.e. $\phi_{\rm n} - \phi_{\rm p} \simeq 180\,^\circ$ or $\phi_{\rm p_1} - \phi_{\rm p_2} \simeq 180\,^\circ$), the large components of the transverse momentum distribution of the residue are suppressed.

Another interesting observation concerning the kinematics of the quasi-free scattering reaction is that for nucleons scattered at almost opposite ϕ angles ($\phi_{\rm n} - \phi_{\rm p} \simeq 180\,^\circ$, $\phi_{\rm p_1} - \phi_{\rm p_2} \simeq 180\,^\circ$), the angle between their momentum vectors peaks at $77\,^\circ \pm 3\,^\circ$, as shown in the inset of Fig. 5.21(bottom). This is evidence of the quasi-free nature

of the scattering, since for free nucleon-nucleon scattering at relativistic energies of $\sim$ 500 MeV the scattered nucleons are moving on the same plane with an angle of $\sim 83\,^\circ$ between their momentum vectors.

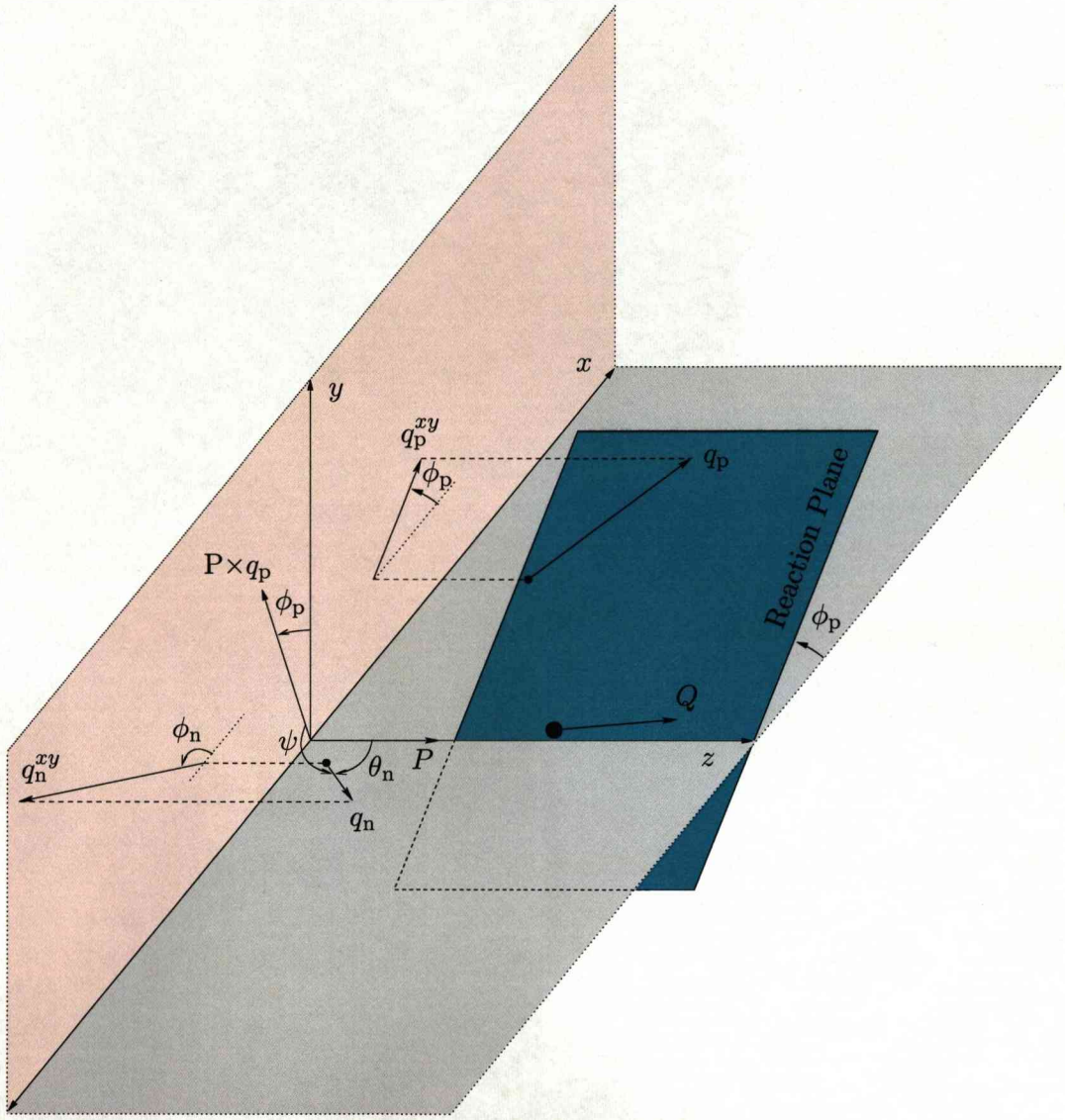

Figure 5.22: Quasi-free scattering kinematics for the (p,pN) reaction. $\vec{P}$ and $\vec{Q}$ are the momentum of the nucleus before and after the reaction, respectively, while $\vec{q}_p$ and $\vec{q}_n$ are the momentum vectors of the scattered proton (from the target) and the knocked-out nucleon, respectively. The reaction plane is defined from $\vec{P}$ and $\vec{Q}$.

Chapter 6

Conclusions and future work

This thesis has presented the first preliminary results of an experiment performed at the LAND/ALADIN setup at GSI which aims, among other things (see Chapter 1), at studying the single-particle structure of ^{57}Ni via one-nucleon removal reactions using a C target. The feasibility of the quasi-free scattering process in inverse kinematics has also been demonstrated by studying the reaction of the ^{57}Ni ions with the protons of a CH_2 target.

Regarding the one-nucleon removal reactions, the inclusive cross section and the transverse momentum distribution of the residual core for the C(^{57}Ni,^{56}Ni)X and the C(^{57}Ni,^{56}Co)X reactions have been measured for the diffractive and the stripping channel, respectively. A more narrow momentum distribution has been observed for removing a neutron compared to the proton-removal reaction from ^{57}Ni, as expected due to the presence of the $l = 1$ component of the valence neutron in the distribution. As the coincident γ-ray measurement has yet to be included in the analysis, the contributions from all possible final states are present in the measurement. In order to obtain exclusive measurements from this experiment, the calibrations and simulations regarding the detection efficiency of the CsI array should be finalised. The efficiency of the LAND detector, which is used to extract the cross section for the C(^{57}Ni,^{56}Ni)X reaction in this thesis, has only been roughly estimated. A more detailed simulation of the CsI and LAND detector response is currently under way within the collaboration.

Concerning the quasi-free scattering reactions in inverse kinematics, where very little experimental evidence exist, a clear observation of the (p,2p) and the experimentally more challenging (p,pn) knockout reaction has been achieved. It has also been possible to interpret the basic kinematics of these reactions and understand the strong correlation between the momentum distribution of the heavy residue and the angle of the two outgoing nucleons. The results presented in this thesis strongly support that these reactions can be developed into a powerful spectroscopic tool to be used in radioactive beam experiments.

The momentum distributions presented in this thesis are shown together with some

preliminary theoretical calculations. However, the results for both the one-nucleon removal and the quasi-free scattering reactions need a more thorough theoretical support. In particular, although the one-nucleon removal reactions have been an established spectroscopic tool, they are usually performed with lower beam energies. Moreover, the hadronic quasi-free reactions in inverse kinematics have only been attempted very recently and the theoretical framework to support this type of reactions is under development.

One of the main experimental programs within the R^3B project is the development of the quasi-free scattering reactions in inverse kinematics using relativistic radioactive ion beams into a powerful spectroscopic tool. In this thesis it has been shown that such quasi-free scattering reactions are feasible in the near future and that the observables from such reactions are rather clean, even with the use of a polyolefin (CH_2) target instead of a pure liquid-hydrogen target. The required improvements in the experimental setup, in order to explore the full capabilities of the quasi-free scattering reactions in inverse kinematics, are the implementation of a target-recoil detector, consisting of Si strips, and a high-efficiency calorimeter. The Si strips can deliver excellent angular-correlation measurements for the outgoing protons, while the calorimeter measures the total energy of the nucleons and the prompt γ rays in the reactions. The development of the calorimeter is under way, while the Si strip detectors are currently mounted and used in recent experiments.

This thesis also presented part of the calibration and reconstruction procedures developed and implemented in the common analysis *land02* framework. A particular emphasis has been placed upon the algorithm developed for finding neighbours on a deformed grid, which allows the tedious position calibration of the position sensitive Si pin diodes to be performed on-line. Some of the advantages of working within such a framework have been highlighted and the need for an advanced tracking algorithm has been discussed. It has also been noted that the development of such framework is essential as the setup becomes more and more complicated and the number of people involved in the analysis of the experiments grows.

Bibliography

[1] http://www.stfc.ac.uk/About/Introduction.aspx.

[2] http://www.gsi.de/fair.

[3] http://www.gsi.de/fair/experiments/NUSTAR/index_e.html.

[4] Aumann, T. *Prog. Part. Nucl. Phys.* **59**, 3 (2007).

[5] http://www.gsi.de.

[6] Paar, N. *et al. Phys. Rev. C* **67**, 034312 (2003).

[7] Leistenschneider, A. *et al. Phys. Rev. Lett.* **86**, 5442 (2001).

[8] Adrich, P. *et al. Phys. Rev. Lett.* **95**, 132501 (2005).

[9] Navin, A. *et al. Phys. Rev. Lett.* **85**, 266 (2000).

[10] Terry, J. R. *et al. Phys. Rev. C* **77**, 014316 (2008).

[11] Sorlin, O. *et al. Phys. Rev. C* **47**, 2941 (1993).

[12] Sorlin, O. *et al. Phys. Rev. Lett.* **88**, 092501 (2002).

[13] Oros-Peusquens, A. M. and Mantica, P. F. *Nucl. Phys. A* **669**, 81 (2001).

[14] Langanke, K. *et al. Phys. Rev. C* **67**, 044314 (2003).

[15] Gould, C. R. *et al. Phys. Rev.* **188**, 1792 (1969).

[16] Kraus, G. *et al. Phys. Rev. Lett.* **73**, 1773 (1994).

[17] Rehm, K. E. *et al. Phys. Rev. Lett.* **80**, 676 (1998).

[18] Yurkewicz, K. L. *et al. Phys. Rev. C* **74**, 024304 (2006).

[19] http://www.nndc.bnl.gov/ensdf.

[20] Bohr, N. and Wheeler, J. A. *Phys. Rev.* **56**, 426 (1939).

[21] Mayer, M. G. *Phys. Rev.* **75**, 1969 (1949).

[22] Haxel, O., Jensen, J. H. D., and Suess, H. E. *Phys. Rev.* **75**, 1766 (1949).

[23] Casten, R. F. *Nuclear Structure from a Simple Perspective.* Oxford University Press, (1990).

[24] Mueller, A. C. *et al. Nuclear Structure under Extreme Conditions of Isospin, Mass, Spin and Temperature.* NuPECC report, (1997).

[25] Tanihata, I. *et al. Phys. Rev. Lett.* **55**, 2676 (1985).

[26] Yoshida, S. and Sagawa, H. *Phys. Rev. C* **69**, 024318 (2004).

[27] Klimkiewicz, A. *et al. Phys. Rev. C* **76**, 051603(R) (2007).

[28] Thibault, C. *et al. Phys. Rev. C* **12**, 644 (1975).

[29] Dobaczewski, J. *et al. Phys. Rev. C* **53**, 2809 (1996).

[30] Brown, B. *et al. Phys. Rev. C* **65**, 061601(R) (2002).

[31] Hansen, P. G. and Tostevin, J. A. *Ann. Rev. Nucl. Part. Sci.* **53**, 219 (2003).

[32] Olson, D. L. *et al. Phys. Rev. C* **28**, 1602 (1983).

[33] Kidd, J. M. *et al. Phys. Rev. C* **37**, 2613 (1988).

[34] Gade, A. *et al. Phys. Rev. Lett.* **93**, 042501 (2004).

[35] Tostevin, J. A. Private communication, Surrey.

[36] Catford, W. N. *et al. Eur. Phys. J. A* **25**, 245 (2005).

[37] Catford, W. N. *et al. J. Phys. G: Nucl. Par. Phys.* **31**, S1655 (2005).

[38] Maddalena, V. *et al. Phys. Rev. C* **63**, 024613 (2001).

[39] Aumann, T. *et al. Phys. Rev. Lett.* **84**, 35 (2000).

[40] Al-Khalili, J. and Nunes, F. *J. Phys. G: Nucl. Par. Phys.* **29**, R89 (2003).

[41] Johnson, R. C. *et al. Phys. Rev. C* **1**, 976 (1970).

[42] Glauber, R. J. *Lectures in Theoretical Physics*, volume 1. New York: Interscience, (1959).

[43] Feshbach, H. *Theoretical Nuclear Physics.* John Wiley and Sons, (1992).

[44] Satchler, G. R. *Introductory Nuclear Reactions.* The Macmillan Press LTD, London and Basingstoke, (1980).

[45] Al-Khalili, J. and Roeckl, E., editors. *The Euroschool Lectures on Physics with Exotic Beams*, volume 1. Springer, (2004).

[46] Tostevin, J. A. *J. Phys. G: Nucl. Par. Phys.* **25**, 735 (1999).

[47] Tostevin, J. A. *Nucl. Phys. A* **320c**, 682 (2001).

[48] Sauvan, E. *et al. Phys. Rev. C* **69**, 044603 (2004).

[49] Jacob, G. *et al. Rev. Mod. Phys.* **38**, 121 (1966).

[50] Jacob, G. *et al. Phys. Lett. B* **45**, 181 (1973).

[51] Jacob, G. *et al. Rev. Mod. Phys.* **45**, 6 (1973).

[52] Chew, G. F. and Wick, G. C. *Phys. Rev.* **85**, 636 (1952).

[53] Samanta, C. *et al. Phys. Rev. C* **34**, 1610 (1986).

[54] Kitching, P. *et al. Nucl. Phys. A* **340**, 423 (1980).

[55] Lemmon, R. C. *et al.* GSI Experimental Proposal, R^3B and EXL collaboration, November (2004).

[56] Aumann, T. Technical report, GSI Darmstadt, January (2005).

[57] Geissel, H. *et al. Nucl. Instrum. Methods Phys. Res. B* **70**, 286 (1992).

[58] Johansson, H. T. Licentiate of Engineering, Chalmers University of Technology, Göteborg, Sweden, (2006).

[59] Knoll, G. F. *Radiation Detection and Measurement.* John Wiley & Sons, Inc., 3rd edition, (2000).

[60] Cub, J. *et al. Nucl. Instrum. Methods Phys. Res. A* **402**, 67 (1998).

[61] http://www-land.gsi.de/a_new_land/__public/documentation/detectors/gfi/gfi.html.

[62] http://www-land.gsi.de/a_new_land/__public/documentation/detectors/tof_wall/pictures/tof_pictures.html.

[63] http://www-land.gsi.de/a_new_land/__public/documentation/detectors/csi/tlange_mirror/CsI/csi.html.

[64] Blaich, T. *et al. Nucl. Instrum. Methods Phys. Res. A* **314**, 136 (1992).

[65] http://www-land.gsi.de/a_new_land/__public/documentation/detectors/land/land.html.

[66] Johansson, H. T. PhD thesis, Chalmers University of Technology, to be published.

[67] Adrich, P. *Observation of Pygmy and Giant Dipole Resonances in ^{132}Sn and neighboring mass isotopes.* PhD thesis, Krakow, (2005).

[68] Mahata, K. *et al. Nucl. Instrum. Methods Phys. Res.*, in preparation.

[69] http://www-linux.gsi.de/~weick/atima/.

[70] Penner, S. *Rev. Sci. Instrum.* **32**, 150 (1961).

[71] Livingood, J. J. *The Optics of Dipole Magnets.* Academic Press, 3rd edition, (1969).

[72] Kalman, R. E. *J. Basic Eng.* **82**, 35 (1960).

[73] Bertulani, C. A. and Hansen, P. G. *Phys. Rev. C* **70**(3), 034609 Sep (2004).

[74] Aumann, T. Private communication, GSI.

[75] Chulkov, L. V. *et al. Nucl. Phys. A* **759**, 43 (2005).